

LAPPEENRANTA-LAHTI UNIVERSITY OF TECHNOLOGY LUT  
School of Engineering Science  
Master's Degree Programme in Chemical and Process Engineering

*Kosisochi Fiona Ibebunjo*

**SHAPE MEMORY RESPIRATOR MASK FOR COVID-19**

Examiners: Associate Professor Eveliina Repo  
Ph.D. Samantha Kiljunen

## **ABSTRACT**

Lappeenranta-Lahti University of Technology LUT  
School of Engineering Science  
Master's Degree Programme in Chemical and Process Engineering

Kosisochi Fiona Ibebunjo

### **Shape Memory Respirator Mask for Covid-19**

Master's thesis

2021

97 pages, 48 figures and 22 tables

Examiners: Associate Professor Eveliina Repo

Ph.D. Samantha Kiljunen

Keywords: Facemask, respirator, Covid, shape memory, SMP, polymer, extrusion, PLA, PCL

The outbreak of Covid-19 has increased the demand for facemask and focused several research on producing masks that offer maximum protection. However, the level of protection a mask can offer depends on the mask type and mask fit which in turn depends on facial size and shape. Since face shapes and sizes are different, one mask size will not fit all faces.

In this research, Shape-memory polymers (SMP) based on polymers blends were studied as alternative polymers for making respirator masks that can change shape and size and be moulded or remoulded to fit any face. Different polymer blends with and without compatibilizers or additives were prepared into filaments by polymer extrusion. Successfully extruded blends were characterised and their shape memory behaviour alongside their mechanical properties, melting and crystallization behaviour, morphology, and self-healing behaviour were investigated.

Tensile tests showed the mechanical properties of the SMPs can be tuned by varying the composition of the polymers, compatibilizer and additive in blends. The melting transitions obtained from DSC were used to determine the reversible and fixing phase. SEM images showed all the blends exhibited phase separated morphology which improved on addition of compatibilizer and additive. Thermo-responsive shape memory test conducted on selected blends showed that the crystallization of the reversible phase and the physical interaction at the interface between the two phases in blend were responsible for the shape memory behaviour.

Following the results from characterization and shape memory tests, PLA/PCL blend with 30 wt.% PCL was selected as the best shape memory blend and printing material for the mask. Finally, the 3D printed respirator mask was thermally activated at 65°C and fitted to different faces. The mask showed good shape memory behaviour and could be moulded and remoulded to fit different face shapes and sizes. In addition, the self-healing behaviour of the respirator mask was also investigated, and the mask was observed to heal from scratches placed on it.

The respirator mask designed in this study is for protection against Covid-19 transmission and solves several current facemask issues, such as fit and maximum protection, reusability, and waste minimization.

## **ACKNOWLEDGEMENT**

I would like to express my gratitude to my thesis advisors, Prof. Eveliina Repo and Samantha Kiljunen for giving me the opportunity to participate in this very intriguing research. I am thankful for their support, guidance and invaluable feedback and suggestions.

I would like to thank Marrko Hyvärinen, Toni Väkiparta and Liisa Puro for helping me with tensile test, SEM, and DSC analyses. I also want to thank Mikko Huhtanen, Reijo Heikkinen and Saied Chozaki for their exceptional help and cooperation during my research.

Finally, I would like to express my profound gratitude to my parents, siblings, and friends whose love, unfailing support and guidance has always been with me in all my pursuit. Thank you for believing in me.

Lappeenranta 18.06.2021

Kosisochi Ibebunjo

## TABLE OF CONTENTS

ABSTRACT .....	1
ACKNOWLEDGEMENT .....	2
LIST OF SYMBOLS .....	6
ABBREVIATIONS .....	8
1. INTRODUCTION .....	8
2. FACEMASK .....	13
2.1 Types of facemasks .....	14
2.1.1 Nonmedical facemask .....	14
2.1.2 Medical facemask .....	14
2.1.3 Respirators .....	15
2.2 History .....	16
2.3 Materials and methods for making facemask .....	17
2.4 Facemask test .....	20
2.4.1 Filter penetration test .....	20
2.4.2 Total inward leakage (TIL) .....	22
2.4.3 Breathing resistance Test .....	23
2.4.4 Clogging .....	24
2.4.5 Carbon dioxide build-up test .....	25
2.4.6 Microbial cleanliness (Bioburden) .....	25
3. SHAPE-MEMORY POLYMERS .....	26
3.1 Shape memory effect .....	27
3.2 History .....	28
3.3 Classification of shape memory polymers .....	29
3.3.1 Classification of SMPs based on their polymer structure and composition .....	29
3.3.2 Classification of SMPs based on external stimuli .....	32

3.3.3	Classification of SMPs based on shape-memory function.....	33
3.4	Techniques for preparing shape memory polymers.....	35
3.4.1	Chemical crosslinking of thermoplastics .....	35
3.4.2	Polymerization of monomers or prepolymers with crosslinkers.....	36
3.4.3	Synthesis of phase-segregated block copolymers .....	36
3.4.4	Physical blending of different polymers .....	36
3.4.5	Composite.....	37
3.5	Characterization techniques for shape memory polymers .....	37
3.5.1	Scanning electron microscopy (SEM).....	37
3.5.2	Differential scanning calorimetry (DSC) .....	38
3.5.3	Static tensile test.....	40
3.5.4	Dynamic mechanical analysis (DMA) .....	40
3.6	Characterization techniques for shape memory properties .....	42
3.6.1	Thermomechanical cyclic test.....	43
3.6.2	Bending test.....	45
3.6.3	Heat shrinkage measurement .....	46
3.7	Characterization techniques for self-healing properties .....	47
3.8	Applications .....	48
3.9	Polymer selection.....	49
4.	MATERIAL AND METHODS.....	49
4.1	Materials .....	49
4.2	Extrusion of polymer blend .....	51
4.3	3D printing .....	53
4.3.1	Filament testing .....	53
4.3.2	Mask 3D printing .....	53
4.4	Characterization .....	54
4.4.1	Tensile test.....	54

4.4.2 Differential Scanning Calorimetry (DSC).....	55
4.4.3 Scanning Electron Microscopy (SEM) .....	56
4.4.4 Shape Memory test.....	56
5. RESULTS AND DISCUSSION.....	57
5.1 Extrusion.....	57
5.2 Mechanical properties.....	57
5.3 Crystallization and melting behaviour.....	66
5.4 Morphology of the blends.....	74
5.5 Filament testing.....	79
5.6 Thermo-responsive shape memory behaviour and mechanism.....	80
5.7 3D printed mask.....	84
5.8 Mask fitting.....	84
5.9 Self-healing behaviour.....	85
6. CONCLUSION .....	86
7. FUTURE RESEARCH.....	88
REFERENCES .....	90

## LIST OF SYMBOLS

$C_0$	Photometer reading for clean air
$C_1$	NaCl aerosol concentration before the test specimen
$C_2$	NaCl aerosol concentration after the test specimen
$C_1$	Aerosol concentration
$C_2$	Mean of measured aerosol concentration
$CO_2$	Carbon dioxide
$E^*$	Complex dynamic modulus
$E'$	Storage modulus
$E''$	Loss modulus
$\epsilon_m$	Mechanical deformation
$\epsilon_p$	Permanent shape
$\epsilon_u$	Temporary shape
$Fe_3O_4$	Iron Oxide
$H_c$	Crystallization enthalpy
$H_m$	Melting enthalpy
$l_0$	Photometer zero reading for clean air
$l_1$	Photometer reading before the test specimen
$l_2$	Photometer reading before the test specimen
$l_o$	Original length of test sample
$l_1$	Test sample length after shrinkage
$l_{str}$	Test sample length after stretching
$P$	Penetration
$P$	Leakage
$P_{healed}$	Tensile strength of the healed specimen
$P_{notched}$	Tensile strength of the notched specimen
$P_{virgin}$	Tensile strength of the virgin specimen
$R_f$	Shape/strain fixity
$R_r$	Shape/strain recovery
$\tan \delta$	Angle for phase change
$T_c$	Crystallization temperature

$t_{Ex}$	Total time of exhalation
$T_g$	Glass transition temperature
$T_{high}$	Above transition temperature
$t_{In}$	Total time of inhalation
TIL	Total inward leakage
$T_{low}$	Below transition temperature
$T_m$	Melting temperature
$T_{perm}$	Highest thermal transition
$T_{trans}$	Transition temperature
$\sigma_m$	Constant stress
$\Theta_{final}$	Final angle
$\Theta_{fixed}$	Fixed angle
$\Theta_i$	Series of angles
$\Theta_{max}$	Maximum angle
$\lambda$	$l_{str}/l_o$
$\%_{heal}$	Degree of healing

## ABBREVIATIONS

CDC	Centers for Disease control and Prevention
CNT	Carbon nanotube
COVID	Coronavirus
DMA	Dynamic mechanical analysis
DSC	Differential scanning calorimetry
ECDC	European center of disease Prevention and Control
EOET	Ethylene oxide–ethylene terephthalate
FDA	Food and Drugs Administration
FDM	Fused deposition modelling
HDPE	High density polyethylene
HSCT	Higher solution critical temperature
LDPE	Low density polyethylene
LOM	Laminated object manufacturing
LSCT	Lower solution critical temperature
LUT	LAPPEENRANTA-LAHTI UNIVERSITY OF TECHNOLOGY
MERS	Middle east respiratory disease
MFI	Melt flow index
M <sub>n</sub>	Number average molecular weight
MW/M <sub>w</sub>	Molecular weight
N	Number of cycles
NaCl	Sodium chloride
N95, N99, N100	Non-oil 95%, 99%, 100%
NIOSH	National Institute for Occupational Safety and Health
NPF	Nominal Protection Factor
OSHA	Occupational Safety and Health Administration
PA	Polyamide
PAN	Polyacrylonitrile
PBA	Poly (1,4-butylene adipate)
PC	Polycarbonate
PCL	Polycaprolate/Polycaprolactone
PCLA	Poly (l-lactide- <i>co</i> - $\epsilon$ -caprolactone)

PCR	Polymerase chain reaction
PE	Polyethylene
PEG	Polyethylene glycol
PEG-b-PCL	Poly (ethylene glycol) methyl ether- block -poly ( $\epsilon$ -caprolactone)
PE-g-ma	Polyethylene-graft-maleic anhydride
PES	Polyester
PET	Polyethylene terephthalate
PLA	Poly(lactic acid)
PLGA	Poly (lactic- <i>co</i> -glycolic acid)
PM	Particulate matter
PMMA	Poly (methyl methacrylate)
PP	Polypropylene
PPDO	Poly(p-dioxanone)
PP-g-ma	Polypropylene-graft-maleic anhydride
PPE	Personal protective equipment
PS	Polystyrene
PUR	Polyurethane
RPM	Revolutions per minute
SARS	Severe acute respiratory syndrome
SDA	Sabouraud Dextrose agar
SEM	Scanning electron microscopy
SLM	Selective laser melting
SMASH	Shape memory assisted healing
SME	Shape memory effect
SMF	Shape memory fibre
SMP	Shape memory polymer
SMPC	Shape memory polymer composites
TPU	Thermoplastic polyurethane
TSA	Tryptic Soy Agar
US	United States
UV	Ultraviolet
WHO	World Health Organisation
wt.	Weight

## 1. INTRODUCTION

Since the outbreak of coronavirus disease in December 2019, the demand for facemask has been increasing (O'Dowd, et al., 2020; Wibisono, et al., 2020). Coronavirus is a pneumonia-based disease caused by the novel SARS-COV-2. It is believed that the disease is linked to the severe acute respiratory syndrome (SARS) and the middle east respiratory disease (MERS). The disease is alleged to have originated from a seafood market in Wuhan in China, although it has not been confirmed (O'Dowd, et al., 2020).

The mode of transmission of this disease varies but is largely by droplets and contact transmission, although airborne transmission route is evidently emerging. The contact transmission can be direct or indirect contact via the saliva or respiratory droplets and secretions of infected persons expelled when they are talking, coughing, singing, or sneezing. The direct contact occurs by transmission of the virus via physical contact between the infected person and susceptible person while the indirect contact occurs when the virus is transmitted by an intermediate object usually formite (i.e., a contaminated surface or contaminated object which has been infected with respiratory secretions or droplet). The droplet transmission occurs when droplets are produced when an infected person talks, coughs or sneezes. The droplets created can be large droplets or small (fine) droplets called aerosols. Large droplets ( $>5-10\mu\text{m}$ ) created do not suspend in air for too long and settle quickly while the aerosol droplets ( $\leq 5\mu\text{m}$ ) suspend in air for a long time and may eventually evaporate. This leaves even smaller droplets in air which are considered as airborne and can be inhaled. Several reports have shown that these droplets can go as far as 20 feet for a strong cough or sneeze while smaller droplets of  $1\mu\text{m}$  can stay longer than 12 hours in air (WHO, 2020a; O'Dowd, et al., 2020).

As the virus continued to spread easily, personal hygiene, social distancing and self-quarantine was advised and implemented to minimize the spread. The pandemic continued for months, and the lockdown and travel restrictions imposed to minimize the virus from spreading resulted in economic deceleration. Workers had to return to work to rebuild and sustain the economic condition. Hence, complete social distancing was unsustainable and the need to implement new actions to minimize the spread of the virus became necessary. In addition, some people infected with coronavirus show symptoms such as coughing, fatigue sneezing, etc. Some infected people

do not show symptoms at all and some show symptoms much later even though they are carriers. Those that do not show any symptoms are said to be asymptomatic while those that show symptoms later are pre-symptomatic (Wibisono, et al., 2020; Chua, et al., 2020). Taking all these factors into consideration, the world health organisation (WHO) together with the Centers for Disease control and Prevention (CDC) recommended the use of facemask to protect ourselves, minimize the spread of the virus and save lives (O'Dowd, et al., 2020; CDC, 2020a).

Facemasks are the most important personal protective equipment (Chua, et al., 2020). They are a type of personal protective equipment (PPE) used to prevent or minimize the spread of respiratory infections and are effective at helping prevent transmission of respiratory viruses and bacteria. The facemask is used to avoid contamination of the surrounding after a person sneezes or coughs and to also filter already contaminated air when inhaled. They play an important role to minimize the spread of the virus especially when a carrier is presymptomatic or asymptomatic as shown in Figure 1 (Chua, et al., 2020). Without these PPE, healthcare providers, essential workers, and the public in general are exposed to the risk of infection (CDC, 2020b)

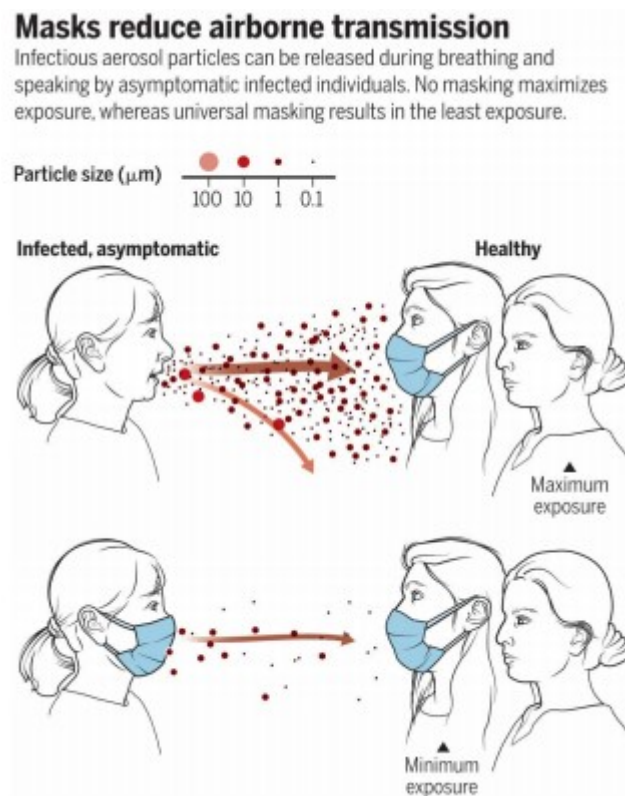


Figure 1. Schematic representation of how facemask helps reduce transmission (Chua, et al., 2020).

Different types of facemasks made from different materials and offering different levels of protection are in existence today (Chua, et al., 2020). Their effectiveness and quality depends on their filtration capacity (i.e., the ability of the mask to filter particles of specific size range) which in turn depends on the type of material used in making them (O'Dowd, et al., 2020). Air contaminants are known to vary in sizes while the size of SARS-COV-2 ranges from 60-140nm, which is less than the size range of bacteria, pollen, and dust as shown in Figure 2. Therefore, masks made with materials of large pore sizes such as cotton, synthetic fabric, etc, will offer low level of protection to its users against the virus. These types of masks will be less effective in filtering the viruses than masks made from materials with small pore sizes such as medical mask and respirators (Chua, et al., 2020).

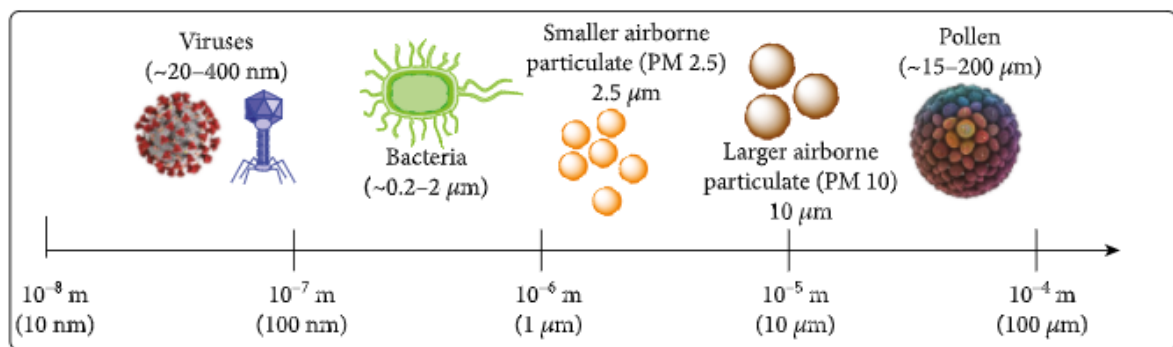


Figure 2. Sizes for pathogens and airborne pollutants (Chua, et al., 2020).

In addition to filtration capacity, the effectiveness and quality of a facemask depends on its fit (O'Dowd, et al., 2020). Most facemasks are loose and do not prevent leakage from the sides, therefore do not filter particles from air completely. In view of this, CDC has recommended that facemask should cover the mouth and nose completely, fit properly on the sides of the face and not have spaces. This requirement ensures proper fitting and insignificant leakages when worn with all air directed via the filter media.

According to CDC, the medical mask and N95 respirators are the most effective facemask for protection against covid-19 (CDC, 2020c). Medical mask are disposable and loose-fitting face-mask with fluid resistance properties. They cover the user's mouth and nose and acts as a barrier against particulates and fluid. Due to their loose-fitting, they may not offer maximum protection from inhaling airborne pathogens. Respirators in contrast to medical mask are designed to be

tight-fitting and covers the users mouth and nose as well as offer higher level of protection against pathogens (FDA, 2020). In general, face masks are recommended for diseases transmitted through droplets and respirators for respiratory aerosols and the aim is it to utilize both to prevent infections in public settings (Liu & Zhang, 2020). The N95 respirators are US standard and approved by National Institute for Occupational Safety and Health (NIOSH) under the new particulate filter tests (Özer & Haamustafaoğlu, 2020). They been recommended by CDC particularly for healthcare workers and patients of Covid-19 to prevent airborne transmission. With filter efficiency of 95%, this filter removes large, small, and very small particles below 0.3  $\mu\text{m}$ . N95 respirators lower the user's exposure to airborne particles in form of aerosols and droplets, as well as viruses and bacteria which remain in air for hours (CDC, 2020c).

In Europe, the FFP2 respirator with filtration efficiency of  $\geq 94\%$  corresponds to the N95 US standard respirators (Özer & Haamustafaoğlu, 2020). According to WHO, the medical mask and N95 respirators or FFP2 respirators or equivalent standards are the most effective facemask for protection against covid-19 when in public or health care environment or handling cargo. The N95 respirators or FFP2 respirators or equivalent are solely recommended for use by healthcare workers when performing aerosol producing procedures while the medical masks are recommended for use by healthcare workers, cleaners, caregivers, lab technicians, etc, when in contact with COVID-19 patients or patients with respiratory symptoms (WHO, 2020b).

Medical mask and respirators are typically made from polymer materials. They are usually made up of layers of the mostly used nonwoven material. The polymers are used in spun bond, melt-blown and electrospinning technology to produce the nonwoven material, and consequently used to make the mask (Henneberry, 2020a; Adanur & Ajay, 2020). Polymers such as polypropylene, polyethylene, polystyrene, polycarbonate can be used (Wibisono, et al., 2020; Özer & Haamustafaoğlu, 2020). 3D printing is another technology that has been used to make facemask especially in this COVID-19 pandemic. This technology can be used to print different designs of masks and custom-made masks based of the wearers facial dimension (Swennen, et al., 2020). 3D printing technology uses a printer and a printing material such as polymer to produce a physical object of a digital design by layer-to-layer application of a printing material. The technology has been used in printing different designs of facemasks and other PPEs such as face shields, ventilators, and goggles as well (Bharti & Shailendra, 2020).

Although respirator masks are tight-fitting and cover the users mouth and nose, the ability of a wearer to get a mask that properly fits depends on the facial dimension of the wearer. Face sizes and shapes are different, and a respirator mask of one size and shape will not fit all faces. Of course, a mask can be custom-made based on an individual's facial dimension and size, however the mask can only be utilized by the same individual and not perfectly fit another face. As various research on reducing and reusing respirator masks to reduce demand and minimize waste are still ongoing, the idea of custom-made mask becomes restricted since their shape or size cannot be changed to fit another face during reuse. Also, the possibility to use the masks for several years becomes a challenge when the owner of a customized mask leaves the job or becomes unavailable to use the mask. As such, there is a need to develop a mask that can be moulded and remoulded to fit any face. This will improve the fitting and reusability of masks as well as minimize waste accumulated from masks.

The concept of shape-memory polymers as an alternative polymer for making face masks was recommended in Bailar, et al. (2006) but an investigation of this concept has not been reported till date and to my knowledge. Shape-memory effect has been reported since 1940s in a US patent which mentioned observing shape-memory effect in a dental material produced from methacrylic acid resin. Recently, researchers have developed huge interest in SMPs because of its numerous applications and ease of production. Shape-memory polymers are smart polymers which can change from their original shape to a temporary shape and back to their original shape when exposed to stimulus such as heat, light, solvent, etc., The thermo-responsive SMPs are the most studied SMPs because their shape memory effect results from a combination of polymer morphology and thermo-mechanical programming technology. Generally, they contain two segments, the soft segment which acts as the temporary shape and is responsible for changing shape, and the hard segment which defines the permanent shape. The shape memory capability is enabled when the permanent shape is deformed and then fixed into a temporary shape by cooling the soft segment below its transition temperature. The permanent shape can be recovered by reheating the deformed polymer above the transition temperature of the soft segment resulting in the recoiling of the polymer chains from the temporary state to the original state. In addition to shape memory properties of SMPs, they also exhibit self-healing ability and can repair mechanical damages such as marks, scratches, or cracks. This property allows the materials' lifespan and performance to be extended. Their self-healing performance depends on the properties of the polymer material and consequently, on the special functional

properties of the polymer such as reversible interactions. Their self-healing ability is as a result of the shape recovery of the SMP which brings the scratched or cracked surfaces in close contact when an external stimulus such as heat is applied, thus healing the damage (Hager, et al., 2015; Bhattacharya, et al., 2020; Xie, 2011). Shape memory polymers have dual and multi-shape property which has made them potential materials in various challenging applications such as in self-coupling mobile phones, drug carriers, smart medical devices, smart fabrics, self-healing material, etc., (Marc & Andreas, 2007; Parameswaranpillai, et al., 2020; Behl & Lendlein, 2007; Jianwen & Song, 2011).

In this study, the concept of shape memory was studied. Different thermo-responsive shape memory polymer blends were prepared by polymer extrusion. The polymer blends extruded consist of two polymers, with one acting as the soft segment and the other as the hard segment. Shape memory polymer blend with compatibilizers and additives were also extruded. The compatibilizers and additive were introduced to improve compatibility, interfacial adhesion, and mechanical properties of the blends. The shape memory effect alongside the mechanical properties, melting and crystallization behaviour, morphology, and self-healing behaviour of the SMP was investigated. Subsequently, the filaments extruded were used as printing materials to 3D print facemasks that can change shape and size to fit any face when thermally actuated. Finally, the 3D printed facemasks are thermally activated and fitted to different faces. The shape memory facemask developed is for protection against Covid-19 transmission.

## **2. FACEMASK**

Facemask is a type of personal protective equipment (PPE) used to prevent or minimize the spread of respiratory infections and is effective at helping to prevent transmission of respiratory viruses and bacteria. They are used to avoid contamination of the surrounding after a person sneezes or coughs and to filter an already contaminated air when inhaled (Chua, et al., 2020). Although all respiratory protective equipment are called facemask, different types of facemasks exist for different purposes or people. Different facemask recommendations exist for healthcare professionals and for the public use. Also, different facemask recommendations exist for high-risk people and the rest of the public (Sozkes & Serda, 2020; Özer & Haamustafaoğlu, 2020).

## **2.1 Types of facemasks**

### **2.1.1 Nonmedical facemask**

Society has been involved in producing different types of improvised facemasks due to increasing demand for facemasks as well as their widespread shortage in this COVID-19 pandemic. Nonmedical facemasks are self-made, homemade, or commercially made types of facemasks, produced from cloth, or other textile or other raw materials as presented in Figure 3a. They are generally not recommended for use in hospital surroundings or for healthcare workers and have been classified as community or nonmedical masks by European center of disease Prevention and Control (ECDC) and as face coverings by Centers for Disease Control and Prevention (CDC) (Rubio-Romero, et al., 2020). These types of masks are used to prevent transmission of infection from infected people but do not provide effective protection as required for a PPE (Özer & Haamustafaoğlu, 2020).

### **2.1.2 Medical facemask**

They are also known as surgical masks and provide covering to the chin, nose, and mouth of the wearer and acts as a barrier, preventing the transmission of infections between wearers as presented in Figure 3b. These types of masks are regulated by the Europe standard according to EN 14683:2019 + AC:2019 and classified into type I, II, and II R medical masks based on breathing resistance, bacterial filtration efficiency, microbial cleaning, and splash resistance as shown in Table 1. Medical mask has been recommended for patients and healthcare workers in hospital surroundings. Type I medical mask prevents transmission of infection from infected people and are recommended for patients. Type II and II R prevent transmission of infection from infected persons to another as well as provide protection for the wearer from infected droplets. Type II and II R have been recommended for healthcare workers while Type II R is strongly recommended in operating rooms. Medical masks have also recommended for people older than 60 years, people with weakened immune system and people having more than one disease. They are also recommended in crowded environments and places where social distancing is impossible but in cases of shortages, medical masks are reserved only for healthcare workers and vulnerable people (Özer & Haamustafaoğlu, 2020; Rubio-Romero, et al., 2020).

Table 1. Requirements for medical mask defined in EN 14683:2019 + AC:2019 (Alex, 2020).

Test	Type I Medical mask	Type II Medical mask	Type II R Medical Mask
Bacterial filtration efficiency (%)	$\geq 95$	$\geq 98$	$\geq 98$
Breathing resistance (Pa/cm <sup>2</sup> )	<40	<40	<60
Splash resistance (kPa)	Not needed	Not needed	$\geq 16$
Microbial cleanliness (cfu/g)	$\leq 30$	$\leq 30$	$\leq 30$

a



b



Figure 3. (a) Nonmedical facemask (b) Medical facemask (Alex, 2020).

### 2.1.3 Respirators

They are also known as face filtering piece (FFP) and provide higher level of protection to the wearers against air borne contaminants such as aerosols, particles, and droplets. Respirators provide higher filtration efficiency and better fit and seal compared to the medical facemask. Due to its higher level of protection, they have been recommended for high-risk aerosol producing procedures such as PCR sampling for COVID-19, eye examinations, throat examinations, etc (Rubio-Romero, et al., 2020; Özer & Haamustafaoğlu, 2020). Based on their types, respirators are classified into valved and non-valved respirators as illustrated in Figure 4. The valved respirators improve breathability by reducing breathing resistance through the filters. They as well reduce the accumulation of moisture and heat inside the respirator. Therefore, exhalation is easier in valved respirators (no filtration) compared to non-valved, but their inha-

lution resistance is the same (Sozkes & Serda, 2020; Raul, et al., 2020). Respirators are regulated in Europe by the Europe standard according to EN 149:2001+A1:2009 and classified into FFP1, FFP2, and FFP3 respirators based on total inward leakage and filtration efficiency (British Standards Institution, 2009). In US, respirators are classified as N95, N99, N100 by NIOSH. The FFP2 and FFP3 are most suitable for protection against COVID-19 and correspond to N95 and N99 US masks (Özer & Haamustafaoğlu, 2020).

Table 2. Performance requirements for respirators (Lepelletier, et al., 2020).

Test	FFP1	FFP2	FFP3
Filtration efficiency (%)	$\geq 80$	$\geq 94$	$\geq 99$
Total inward leakage (%)	$< 22$	$< 28$	$< 2$

a



b



Figure 4. (a) FFP2 non-valve (b) FFP3 Valved (Rubio-Romero, et al., 2020).

## 2.2 History

In 1897, a surgeon from Poland recorded the earliest use of medical facemask. The mask produced from a one-layer gauze was used to minimize droplets spread from the wearers mouth. In 1898, the effectiveness of the mask to protect the user was observed to increase with increasing the number of layers. By 1899, another mask which had its mouth covered with strips of roller gauze was developed and further in 1905, a mouth guard was developed to control the transmission of tuberculosis which was spread from the sputum droplets. In 1930s, the quality of the mask was enhanced based on requirements by using various filter-based and paper-based

materials in between the gauze. The efficiency of the filter-based materials was found to be higher. Finally, in 1960s two types of disposable masks were developed. The first was made like a moulded shell while the later was made with propylene filters or fibre glass filters. Today, the development of facemask has been cantered on disposable mask while the gauze is no longer in vogue.

The very first respirator called “Nearly” smoke mask was invented in 1877 for use against fires. In 1980s, during the tuberculosis breakout in united states, their use in medical field became evident. In 1997, they were incorporated for use against tuberculosis into Occupational Safety and Health Administration (OSHA) guidelines while in 2002, Food and Drugs Administration (FDA) approved the N95 respirators for use in against airborne diseases (O’Dowd, et al., 2020).

### **2.3 Materials and methods for making facemask**

Due to the size of coronavirus (160-140nm), making of facemask with nonwoven materials has been deemed more suitable and effective than the woven materials (Chellamani, et al., 2013; Chua, et al., 2020). Nonwovens are the main raw material used in aerosol filtration (Krucińska, et al., 2012). Also, the medical masks and N95/FFP2 respirators which are so far the best in this pandemic are being manufactured using nonwoven materials (O’Dowd, et al., 2020; Krucińska, et al., 2012; Chua, et al., 2020). Nonwoven materials can be in form of web, batt or sheet made from synthetic and/or natural fibres or filaments bonded by chemical, mechanical, or thermal means. They can be produced in different categories such as polymer laid originating from polymer melt and solution, dry laid originating from textile industries or wet laid originating from papermaking (Dutton, 2009; Krucinaska, 2005). These nonwoven materials are preferred for facemask because they have high dust absorption capacity, low airflow resistance, high filtration efficiency, low production cost and little or no slippage than when cotton and the advanced woven materials are used (Krucińska, et al., 2012; Chellamani, et al., 2013).

Synthethic polymers are the basic raw material used in manufacture of nonwoven material (Krucińska, et al., 2012). Polymers such as Polypropylene (PP), polycarbonate (PC), polyester (PES), polyethylene (PE), polystyrene (PS), biodegradable poly lactic acid (PLA), polyurethane (PUR) and polyacrylonitrile (PAN) were listed as suitable for producing face masks (Chellamani, et al., 2013; Chua, et al., 2020; Das, et al., 2020; Fadare & Okoffo, 2020).

Polymers such as Polyethylene (PE), polyester polyethylene terephthalate (PET), Polycarbonate (PC), polyamide (PA) and its copolymers, simple and complex PUR are suitable for making textiles for respiratory protection (Krucinaska, 2005). In addition, (Patel, 2015) invented a method for making disposable facemasks which are sustainable and eco-friendly by using biodegradable polymers such as poly lactic acid (PLA), Polycaprolate (PCL), etc.

The spun bond and melt-blown technology are the two most common polymer extrusion methods for producing nonwoven material for facemasks (Henneberry, 2020a; Chua, et al., 2020). The spun bond process is a combination of filament spinning, drawing, laying down to form web, then a bonding of the filaments in web form by mechanical, chemical, or thermal means to form spun bond nonwoven material (Midha & Dakuri, 2017; Chua, et al., 2020). The process involves various integrated steps such as, the extruder, the filter, the metering pump, the spin pack (die assembly), the quenching, drawing and web formation, bonding, and winding. The melt-blown process is comparable to the spun bond process, but the pore size of the material produced is small and the microfibrils produced are much thinner. The die assembly is the major component responsible for the difference in fibre diameter. For spun bond process, the diameter of fibre is usually between 15-35  $\mu\text{m}$  while that of melt-blown is between 1-10  $\mu\text{m}$ . As a result, melt-blown is the technology used in making the core filter material in facemasks (Henneberry, 2020a; Pu, et al., 2018; Chua, et al., 2020). Electrospinning is another technology for making nonwovens for face mask from polymer solutions. The polymer solution charged through an electromagnetic field comes out as thin jet and is collected on a plate in form of nanofibrous nonwoven web. In this technology, a positive charge is directed to the nozzle of a tube containing polymer solution while a negative charge is directed to a collector. This causes the polymer jet at the nozzle to become charged and form a Taylor cone. The polymer jet at the nozzle is extruded and pulled by an applied electromagnetic force which causes it to accelerate and become thinner and consequently split the polymer jets into several filaments, producing nanofibers which are gathered at the collector (Adanur & Ajay, 2020).

Another technology that has been used to make facemask is the 3D printing. This technology uses a printer and various printing materials such as polymer, ceramic, or metal. Using 3D printing, physical objects can be produced from a digital design by layer-to-layer application of a printing material. Selective laser melting (SLM), fused deposition modeling (FDM), laminated object manufacturing (LOM), and other 3D printing methods are now available, with

FDM being utilized for extruded polymers. 3D printing has been continuously applied during this COVID-19 pandemic to fill the gap between demand and supply of PPE by printing various PPE such as surgical mask, face shields, ventilator, goggles, etc. Using this technology, different designs of facemasks have been printed using different polymers materials such as PP, PLA, acryl butadiene styrene (ABS) (Bharti & Shailendra, 2020).

Medical masks are made up of three layers of nonwoven fabric produced from suitable polymeric materials. The outer layer is composed of 15-25gsm nonwoven melt fabric produced from polypropylene using the spun bond method. This layer is usually more water repellent than the others. The middle layer is composed of 25-35gsm nonwoven fabric produced from polypropylene using the melt-blown method. This layer has better filtration capacity than the others due to its higher fibre density. The inner layer is also composed of 15-25gsm nonwoven fabric produced from polypropylene using the spun bond method. This layer is chemically untreated, anti-allergic and softer to provide comfort for the user. Besides polypropylene, other polymers such as polycarbonate, polyester, polyethylene, polystyrene, etc, can be used (Özer & Haamustafaoğlu, 2020; Chellamani, et al., 2013; Henneberry, 2020b). Face filtering respirators, like medical masks, are made up of numerous layers of nonwoven polypropylene fabric. The inner and outer layer is composed of nonwoven fabric produced from polypropylene using the spun bond method. These layers are mostly hydrophobic and act as barrier to the user's exhalation as well as the external environment. The prefiltration and filtration layers are located between the outer and inner layers. The prefiltration layer is usually a needle punched nonwoven which is denser and stiffer and provides rigidity to the respirator while the filtration layer which has higher filtration capacity, is composed of electret nonwoven fabric produced from polypropylene using the melt-blown method (Henneberry, 2020a; Wibisono, et al., 2020; O'Dowd, et al., 2020). The thickness of the filtration layer is typically 800-1200 $\mu\text{m}$  while the inner and outer layer are 100-150 $\mu\text{m}$  and 300-400 $\mu\text{m}$  respectively (Wibisono, et al., 2020).

Polymers used in facemask that have been used in spun bond process include PP, PE, PUR, PES and PA, etc. PP (isotactic) due to its low cost, lowest density, highest yields, and highest versatility has been widely used in nonwovens. PE is also a very important polymer in nonwovens with good hydrophobic and chemical resistance properties, as well as excellent electrical insulation properties. PES have superior modulus, heat stability and tensile strength than PP and widely applied as well. PA has highly energy intensive properties and is more

expensive than PP and PES, while PUR has good elastic properties. Amongst all the polymers mentioned, PUR has been found to be very expensive (Lim, 2010). Though a range of polymers can be used in spun bonding process, high molecular weight (MW) and high MW distribution polymers such as PP, PA, PES are mostly used (Midha & Dakuri, 2017). The polymers used in facemask that have been used in melt-blown process include PP, PE, PUR, PES, PA, PS, PC, PET (Dutton, 2009; Krucinaska, 2005). Though a range of polymers can be used in melt-blown process, low MW and narrow MW polymers are mostly preferred. Low MW means low melt viscosity. Low melt viscosity means high melt flow index (MFI) which results in reduced operating temperature and consequently increased throughput and reduced energy consumption (manufacturing cost) (Dutton, 2009). In general, facemasks are made of multi-layered nonwoven materials manufactured by different combinations of the technologies mentioned above (Krucińska, et al., 2012).

## **2.4 Facemask test**

Worldwide, several standards for testing the performance and safety of respiratory protective masks exist. In Europe, standards to approve the performance of respiratory protective mask has been specified by the European committee of standards and are stated in EN 149:2001+A1:2009. Different functioning components of the mask must satisfy the specified test requirement for its safety to be certified (Blad, et al., 2020). These performance tests include filtration efficiency, total inward leakage, breathing resistance, CO<sub>2</sub> build-up, clogging, flammability (Blad, et al., 2020; Krucińska, et al., 2012; Serfozo, et al., 2017). According to EN 149 standard, face masks are classified based on their filtration efficiency and total inward leakage (British Standards Institution, 2009).

### **2.4.1 Filter penetration test**

The performance of respiratory protective mask can be described in terms of their filtration efficiency. The filter penetration test measures the mask's capacity to filter tiny particles such as aerosols that may cause harm to the wearer (Blad, et al., 2020) thereby ensuring that the wearer inhales purified air. This test includes the penetration test, the exposure test, and an additional storage test in case of reusable filtering materials, all conducted in accordance with EN 13274-7 (British Standards Institution, 2009). Polydisperse sodium chloride (NaCl) and

paraffin oil are used as test aerosols to measure filter penetration. The experiment is carried out in an aerosol chamber where the test specimen (mask) is fitted in a sealed manner on an adaptor. The test aerosol is fed into the test chamber and a specified flow is passed through the test specimen while its concentration is measured before and after passing through the test specimen using a photometer. The filter material penetration test should meet the requirements in Table 3 (British Standards Institution, 2019).

For NaCl, the test aerosol is generated in an aerosol generator which atomizes an aqueous NaCl solution and evaporates the water. The generated aerosol has particle size between 0.06-0.1  $\mu\text{m}$  and aerosol concentration between 4-12  $\text{mg}/\text{m}^3$ . The concentration of the NaCl aerosol is measured before and after passing through the test specimen using a flame photometer as

$$P (\%) = \frac{C_2 - C_0}{C_1 - C_0} \times 100\% \quad (1)$$

where  $P$  is the penetration,  $C_0$  is the photometer reading for clean air, while  $C_1$  and  $C_2$  is the concentration of the NaCl aerosol before and after passing the test specimen. For paraffin oil, the test aerosol is generated in an aerosol generator which atomizes paraffin oil. The generated aerosol has particle size between 0.29-0.45  $\mu\text{m}$  and aerosol concentration between 15-25  $\text{mg}/\text{m}^3$ . The concentration of the paraffin oil aerosol is measured before and after passing through the test specimen using a light scattering aerosol photometer as

$$P (\%) = \frac{l_2 - l_0}{l_1 - l_0} \times 100\% \quad (2)$$

where  $P$  is the penetration,  $l_0$  is the photometer zero reading for clean air, while  $l_1$  and  $l_2$  is the photometer reading before and after the test specimen. During exposure test, the test specimen is exposed to a specified mass of test aerosol and penetration recorded at every five minutes interval. For the reusable filters, a storage test is conducted immediately after the exposure test. The test specimen is stored under ambient condition for  $24 \pm 1$  hour after which another penetration test is conducted (British Standards Institution, 2019).

Table 3. Requirements for filter material penetration test (British Standards Institution, 2009).

Class	Maximum allowable penetration of test aerosol	
	NaCl test (95 L/min)	Paraffin oil test (95 L/min)
FF1	20%	20%
FF2	6%	6%
FF3	1%	1%

#### 2.4.2 Total inward leakage (TIL)

Protection factor is a term used to define the performance of a respiratory protective mask and the “nominal Protection Factor” (NPF) is a standard test performed in the laboratory and describes the level of protection offered by the mask. In Europe, total inward leakage (TIL) corresponds to the NPF (Sun, et al., 2020) and is calculated as (Rengasamy, et al., 2018)

$$NPF = \frac{100}{\text{Maximum TIL (\%)}} \quad (3)$$

TIL is one of the performance requirements stated in EN 149:2001+A1:2009 for respiratory protective masks to be approved. The TIL test is performed to check and prevent leakages before using mask and measures the fitting and sealing of the mask to the wearers face by considering all sources of leakage into and from the mask due to insufficient sealing (Krucińska, et al., 2012; Blad, et al., 2020). Total inward leakage considers the filter penetration, face seal leakage and exhalation valve leakage if any. The experiment is conducted in an enclosure which has NaCl aerosol flowing through it from top to down over the test subjects head at a minimum flowrate of 0.2 m/s. The NaCl test aerosol is generated with an atomizer from 2% NaCl solution in distilled water and its concentration inside the enclosure is maintained at  $8 \pm 4 \text{ mg/m}^3$  with  $\leq 10\%$  variation all through. The generated aerosol has particle size between 0.02-2  $\mu\text{m}$  and mass mean diameter of 0.6  $\mu\text{m}$ . The test subject wearing the test specimen is placed in the enclosure and walks on a treadmill working at 6 km/h. The test subject performs five different exercises such as walking without talking or moving head, turning from side to side, moving head up and down, talking, second walking without talking or moving head, each exercise performed for 2 minutes while in the enclosure. During exercise, inhaled air inside the mask is drawn through the sample probe and the NaCl content is measured using a flame photometer that can measure

NaCl aerosol concentrations between 15 mg/m<sup>3</sup>-5 ng/m<sup>3</sup>. The total inward leakage through the mask is calculated as

$$P(\%) = \frac{C_2}{C_1} \times \left( \frac{t_{In} - t_{Ex}}{t_{In}} \right) \times 100\% \quad (4)$$

Where P is the leakage, C<sub>1</sub> is the aerosol concentration, C<sub>2</sub> is the mean of measured aerosol concentration in the test subjects breathing zone, and t<sub>In</sub> and t<sub>Ex</sub> are the total time of inhalation and exhalation. EN 149:2001+A1:2009 requires that for 10 test subjects and 5 exercises each, 46/50 individual exercise results are not greater than the maximum given in Table 4 and the arithmetic means for 8/10 individual wearer are not greater than the maximum given in Table 4 (British Standards Institution, 2009).

Table 4. Requirements TIL test (British Standards Institution, 2009).

Class	Maximum total inward leakage for NaCl aerosol	
	Individual exercise	Individual wearer
FF1	25%	22%
FF2	11%	8%
FF3	5%	2%

### 2.4.3 Breathing resistance Test

The filtering material of the mask provides additional resistance to flow of inhaled air due to its filtration properties. As a result, tests to assess breathability through the mask and comfort is usually conducted. Breathing resistance test measures both the inhalation and exhalation resistance to air flow through the mask and should meet the requirements in Table 5. During test, the pressure drop across a face mask is measured during inhalation and exhalation.

Table 5. Requirements for breathing resistance test (British Standards Institution, 2009).

Class	Maximum allowable breathing resistance		
	Inhalation resistance		Exhalation resistance
	30 L/min	95 L/min	160 L/min
FF1	0.6 mbar	2.1 mbar	3.0 mbar
FF2	0.7 mbar	2.4 mbar	3.0 mbar
FF3	1.0 mbar	3.0 mbar	3.0 mbar

The test specimen (mask) is fitted in a sealed manner on a dummy head and breathing is stimulated by pumping air through the mouth of the dummy head using an adapter and a breathing machine adjusted to a specified flow (Figure 5) (British Standards Institution, 2009). The breathing machine is usually a radial fan (Blad, et al., 2020). The inhalation and exhalation resistance are assessed by measuring the pressure difference at the inlet and outlet of mask using a pressure sensor (British Standards Institution, 2009). For inhalation resistance, the breathing machine is adjusted to 30 and 95 L/min continuous flow and the dummy head is mounted at the air inlet of the breathing machine. For exhalation resistance, the breathing machine is adjusted to 160 L/min continuous flow or 2 liters of air at 25 cycles per min and the dummy head is mounted at the air outlet of the breathing machine. During exhalation, measurements with dummy head are carried out in 5 different positions such as facing the dummy head directly ahead, facing the dummy head vertically upwards, facing the dummy head vertically downwards, lying the dummy head on the left side and lying the dummy head on the right side (British Standards Institution, 2009).

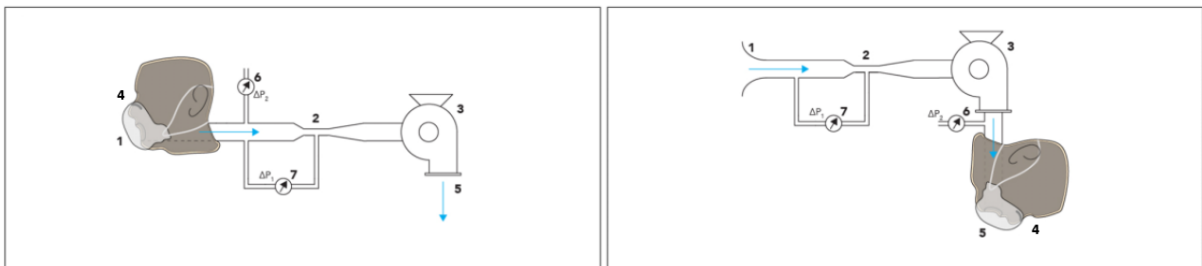


Figure 5. Breathing resistance test setup. (1) Air inlet, (2) A venturi nozzle, (3) Radial fan, (4) Dummy head with leak tight protective mask, (5) Air outlet, (6&7) Pressure sensors (Blad, et al., 2020).

#### 2.4.4 Clogging

Clogging test is an optional test but mandatory for reusable facemask. This test allows us to determine if quick clogging of filter material will occur while using mask. This test is done by measuring the filter material penetration using NaCl and paraffin aerosol, and by measuring breathing resistance displayed by mask after exposure to  $400 \text{ mg/m}^3$  aerosol for 125 minutes (Krucińska, et al., 2012). The experiment is carried out in a dust chamber filled with dolomite dust aerosol continuously flowing at  $60 \text{ m}^3/\text{h}$ . The test specimen is fitted in a sealed manner on a dummy head or sample holder and placed in the dust chamber. A humidifier and a breathing

machine modified to 15 cycles per minute and 2 liters per stroke are connected to the test specimen and operated for a precise exposure time (usually 125 minutes to 400 mg/m<sup>3</sup> of dolomite dust). The breathing machine subjects the mask surrounded by dust to sinusoidal breathing simulation while the humidifier saturates the exhaled air. After the sample exposure, the breathing resistance and filter material penetration are measured. EN 149:2001+A1:2009 requires that the breathing resistance does not exceed the specified value before the required dust load is reached. The maximum breathing resistance is given in Table 6 (British Standards Institution, 2009).

Table 6. Requirements for Clogging test (British Standards Institution, 2009).

Class	Maximum allowable breathing resistance		
	With valve		Without valve
	Inhalation resistance	Exhalation resistance	Inhalation and Exhalation resistance
	95 L/min	160 L/min	95 L/min
FF1	4 mbar	3 mbar	3 mbar
FF2	5 mbar	3 mbar	4 mbar
FF3	7 mbar	3 mbar	5 mbar

#### 2.4.5 Carbon dioxide build-up test

This test measures the CO<sub>2</sub> build up behind the face mask. According to EN 149 standard, CO<sub>2</sub> build up must not exceed 1% by volume. During the experiment, the test specimen is fitted in a sealed manner on a dummy head and breathing is stimulated by pumping air through the mouth of the dummy head using a breathing machine adjusted to 2 liters of air at 25 cycles per min. The breathing machine exhales 2 liters of air of which 5% CO<sub>2</sub> by volume is added to it through a CO<sub>2</sub> analyzer. The exhaled air passes through the facemask fitted to the dummy head to produce some trapped volume of CO<sub>2</sub>. The breathing machine inhales 2 liters of air of which its CO<sub>2</sub> content is measured as well using a CO<sub>2</sub> analyzer. The test is done until CO<sub>2</sub> content in inhaled air is constant (British Standards Institution, 2009).

#### 2.4.6 Microbial cleanliness (Bioburden)

The test is conducted as given in EN ISO 11737-1:2018 and uses an extraction method to determine the total number of microbes on face mask in fulfilment of required standard for

facemask. Aerobic microbial count and fungi enumeration are evaluated with this method. The weighed test specimen is inserted into a bottle (usually 500ml) containing 300 ml of extraction liquid. Extraction liquid is usually composed of 5 g/l NaCl, 2 g/l polysorbate20 and 1 g/l Peptone. The bottle containing specimen is placed on an orbital shaker and agitated for 5 minutes at 250 RPM. For the total viable aerobic microbial count, a 100ml of the extraction liquid is filtered from the bottle through a 0.45  $\mu\text{m}$  filter and the filter is placed on a Tryptic Soy Agar (TSA) plate and incubated for 3 days at 30°C. Similarly, for fungi enumeration, a 100ml of the extraction liquid is filtered from the bottle through a 0.45  $\mu\text{m}$  filter and the filter is placed on a Sabouraud Dextrose agar (SDA) plate with chloramphenicol and incubated for 7 days at 20-25°C. The total bioburden is calculated as the sum of TSA and SDA. Results from the test are evaluated as total bioburden per weight in grams of individual mask. According to EN ISO 11737-1:2018, the bioburden of face mask should be  $\leq 30$  CFU/g (NBN, 2019).

### **3. SHAPE-MEMORY POLYMERS**

Shape-memory polymers (SMPs) are memory retentive polymers which can change from their original shape to a temporary shape and return to their original shape when exposed to external stimulus such as temperature, light, chemical and pH (Behl & Lendlein, 2007). These polymers are responsive to stimuli, where a polymer that shows a change in structure due to change in temperature is a temperature sensitive SMP, and this structural change due to temperature change is a thermally induced shape memory effect. The thermal induced shape memory polymers are the most studied SMPs amongst all the external stimulus applied to induce shape memory effect (SME) (Xu & Jie, 2011).

A single polymer chain cannot exhibit SME because it is not an inherent property of the polymer (Hu, 2007) but is caused by a combination of polymer structure, architecture, specific processing, and programming conditions (Lendlein & Kelch, 2002). The elasticity of polymers goes from soft rubber to hard glass however, SMPs have the features of both hard and soft polymers and can reversibly change their elasticity with transition temperature ( $T_{\text{trans}}$ ). Additionally, they can change their shape when exposed to external stimulus (Hu, 2007). The permanent shape memory polymer is formed by conventional methods such as injection molding or extrusion while the temporary shape is formed afterwards when the permanent shape is deformed by a programming process (Marc & Andreas, 2007). The programming

process can be by heating, deforming, and cooling the material, or by cold drawing. Now the permanent shape is memorized while the polymer shows its temporary shape (Figure 6). The temporary SMP can also return to its permanent shape when subjected to stimulus such as heating at temperature above its transition temperature ( $T_{\text{trans}}$ ) (Lendlein & Kelch, 2002).

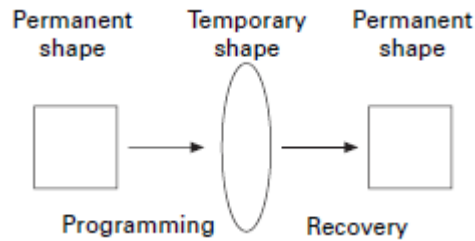


Figure 6. Schematic representation of SMP processing (Lendlein & Kelch, 2002).

In addition to shape memory properties of SMPs, they also exhibit self-healing ability and can repair mechanical damages such as marks, scratches, or cracks. This property allows the materials' lifespan and performance to be extended. Their self-healing performance depends on the properties of the polymer material and consequently, on the special functional properties of the polymer such as reversible interactions. Their self-healing ability is because of the shape recovery of the SMP which brings the scratched or cracked surfaces in close contact when an external stimulus such as heat is applied, thus healing the damage. This behavior is called shape memory assisted healing (SMASH) (Hager, et al., 2015; Bhattacharya, et al., 2020; Xie, 2011). In such systems, reducing stress, followed by heating and the consequent recovery of energy accumulated during crack opening is required to close the crack and heal the sample (Bhattacharya, et al., 2020).

### 3.1 Shape memory effect

Generally, SMPs by their molecular structure are polymer networks with molecular switches that are stimuli responsive. The polymer network contains net points (hard segment) and chain segments (soft segment). The net points are physical or chemical (covalent bond) crosslink points and define the permanent shape of polymer while the chain segment, also called the switching segment, act as the temporary shape and function as reversible molecular switches at  $T_{\text{trans}}$  (Behl & Lendlein, 2007). The switching segment can be crystalline or amorphous and their transition temperature can further be distinguished into a melting temperature ( $T_m$ ) or glass

transition ( $T_g$ ) respectively (Xu & Jie, 2011). The shape-memory effect is enabled when the permanent shape (B) is deformed and then fixed while under external stress to a temporary shape A by adding reversible net points which prevents the deformed switching segment from recoiling as shown in Figure 7. These reversible net points can be created by physical cross-linking achieved by crystallization or vitrification of  $T_{trans}$  domains. They can also be created by covalent cross-linking derived by introducing functional groups to the switching segments. When these temporary shaped (A) polymers are exposed to operating temperature above its  $T_{trans}$ , it becomes flexible and exhibit entropic elastic behavior which causes it to release of the external stress applied and recoil back to its permanent shape B (Marc & Andreas, 2007). Hence the driving force for shape recovery is the recoiling of the polymer chains from the temporary state which is strained to the permanent state which is less oriented (Xu & Jie, 2011).

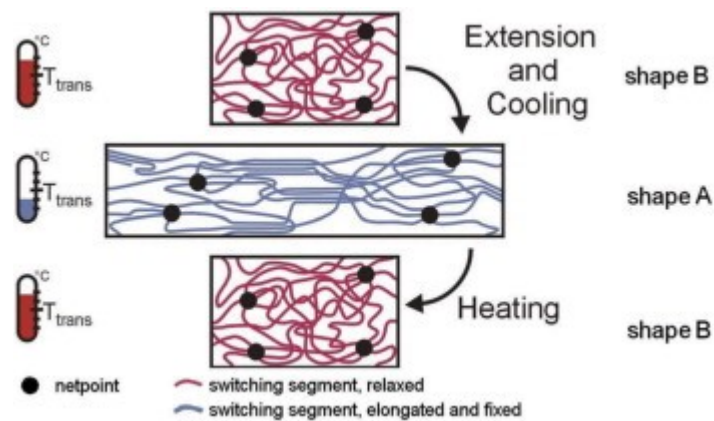


Figure 7. Schematic representation shape memory effect (Marc & Andreas, 2007).

### 3.2 History

L B Vernon first mentioned observing shape memory in a dental material produced from methacrylic ester resin in 1940s (Parameswaranpillai, et al., 2020). In 1950s, a heat shrinkable tubing which showed shape memory was developed by Paul cook using radiation-crosslinked polyethylene. In 1980s, CDF-Chimie company invented SMP poly(norborene) which was later commercialised as Norsorex by a company in Japan. Afterwards, shape memory Poly(trans-isoprene) and poly(styrene-butadiene) were invented in Japan. This series of events lead to further research on polyene based SMPs until polyurethane based SMPs with wide range of properties was discovered by Mitsubishi heavy industries in 1990s (Jianwen & Song, 2011). Till date, several articles reporting shape memory effects have been published (Parameswaranpillai, et al., 2020).

### 3.3 Classification of shape memory polymers

SMPs are basically classified based on their polymer structure and composition, external trigger stimuli and shape-memory function (Parameswaranpillai, et al., 2020).

#### 3.3.1 Classification of SMPs based on their polymer structure and composition

Classification of SMPs based on their polymer structure considering their structure, polymer materials, crosslinking types, morphology, and composition gives four different types of SMPs namely, physically crosslinked, chemically crosslinked, polymer blend and polymer composites (Parameswaranpillai, et al., 2020).

*Chemically crosslinked SMP:* Chemically crosslinked SMP is obtained by connecting polymer chains by covalent bonds and are typically thermosets. They are irreversible in nature and more stable than the physically crosslinked. The covalent bonds can be achieved via linear or branched polymers crosslinking (polymerization), and by copolymerization of a single or more monomers. SMPs such as polyacrylate, styrene copolymers, epoxides, thermosetting polyurethanes have been synthesized by polymerization methods. Chemical crosslinking can also be obtained by polyaddition and polycondensation method. A thermosetting polyurethane with SMP and hydrogel characteristics has been synthesized using this method (Parameswaranpillai, et al., 2020).

*Physically crosslinked SMP:* Physically crosslinked SMP is obtained when the morphology of the polymer contains no less than two segregated phases (Behl & Lendlein, 2007). They are referred to as thermoplastics and the presence of segregated phases in morphology of polymer is the reason for the thermally induced shape memory behavior of thermoplastics (Parameswaranpillai, et al., 2020). In this polymer network, the net point is for the phase with the highest thermal transition ( $T_{perm}$ ) and the chain segment (switching segments) is for the lower thermal transition temperature ( $T_{trans}$ ) (Behl & Lendlein, 2007). The physically crosslinked polymers can additionally be categorized into linear polymers (block and high MW), branched polymers, polymer complex and into SMPs with amorphous or crystalline switching segments (Parameswaranpillai, et al., 2020). The SMPs with amorphous switching segment have  $T_g$  as their  $T_{trans}$  and responsible for the SME. Typical example is the Segmented amorphous shape-memory polyurethanes (PUR) (Leng & Shanyi, 2010). The SMPs with

crystalline switching segment have  $T_m$  as their  $T_{trans}$  and responsible for the SME. Typical examples reported are poly (ethylene oxide-*co*-butylene terephthalate) (Luo, et al., 1997) and poly(L-lactide-*co*- $\epsilon$ -caprolactone) (Lu, et al., 2008). Unlike the chemically crosslinked SMPs, it is possible to remold the fixity phase in physically crosslinked SMPs after getting to the temperature where the physical bonds vanish (Parameswaranpillai, et al., 2020).

*Polymer blend:* SMP blends exist as either miscible or immiscible blends with both showing shape memory properties. Both miscible and immiscible SMP blends have interesting industrial applications due to their ease of blending and the opportunity to synthesize SMPs with enhanced mechanical and thermal properties. The blend is prepared by physically blending two polymers with one polymer having a higher  $T_g$  or  $T_m$  than the other. SMP blends of thermoplastics and thermoplastics with elastomers have been reported. Miscible SMP blends of poly (vinyl acetate) and PLA (Liu & Mather, 2003), poly (vinyl chloride) and thermoplastic polyurethane (TPU) (Jeong, et al., 2001), have been reported in literature. Immiscible SMP blends of PCL and poly(styrene-*b*-butadiene-*b*-styrene) (Zhang, et al., 2009), TPU and PLA (Jing, et al., 2015), PLA and PCL (Liu, et al., 2020; Navarro-Baena, et al., 2016), PLA and Polyethylene glycol (PEG) (Guo, et al., 2018) have also been reported in literature.

Shape memory has also been shown in polymer blends containing a third component such as crosslinkers, compatibilizer, etc. The compatibilizer helps to enhance the miscibility and interfacial adhesion. Introducing a compatibilizer can also improve shape memory properties while maintaining individual properties of the polymers. Zinc dimethyl acrylate was introduced as compatibilizer in polypropylene and ethylenepropylenediene rubber blends. The shape memory characteristics and interfacial adhesion both improved significantly (Parameswaranpillai, et al., 2020). Li, et al. (2009) introduced ethylene-butyl acrylate-glycidyl methacrylate terpolymer as a compatibilizer to in HDPE/PET blends and reported enhanced miscibility and interfacial adhesion as well as enhanced shape recovery. Qin, et al. (2018) introduced dicumyl peroxide as compatibilizer to PLA/PPC (polypropylene carbonate) blend and reported enhanced miscibility, mechanical properties, and shape memory properties.

*Polymer composites:* In shape memory polymer composites (SMPCs), micro-sized and nano-sized fillers are introduced to improve polymers properties such as mechanical properties and recovery stress. Due to the fillers, SMPCs possess enhanced shape memory and mechanical

properties as well as novel two-way SME, multi-SME, indirect SME, etc. Ratna & Karger-Kocsis, (2008) introduced Kevlar and glass as fillers and reported reduced recoverable strain and improved stiffness. Zhou, et al. (2007) and Meng, et al. (2009) reported improved shape memory properties of poly (D,L-lactide) using hydroxyapatite and chitosan respectively as filler.

*Segmented Block Copolymers:* SME in segmented block copolymers is between comonomers and is dependent on their  $T_{\text{trans}}$ . The comonomer with the lower  $T_m$  or  $T_g$  is the switching phase while the comonomer with higher  $T_m$  or  $T_g$  is the fixity phase. An example is poly (l-lactide-co- $\epsilon$ -caprolactone) (PCLA) with l-lactic acid comonomer as the fixity phase and  $\epsilon$ -caprolactone comonomer as the switching phase. Another example is the ethylene oxide–ethylene terephthalate segmented copolymers (EOET) with ethylene terephthalate comonomer as the fixity phase and ethylene oxide comonomer as the switching phase, also in poly (lactic-co-glycolic acid) (PLGA) and PURs (Parameswaranpillai, et al., 2020).

*Cross-Linked Homopolymers:* This class of shape memory polymers has both crystalline and amorphous phase in a single polymer. The crystalline phase is the fixity phase and responsible for giving shape to the SMP while the amorphous phase is the switching phase, and the reaction of its physical bonds is responsible for assigning temperature and reshaping. Semicrystalline PLA is an example of shape memory homopolymers although its SME is restricted to a narrow temperature range (Parameswaranpillai, et al., 2020).

*Hydrogels and Supramolecular Polymers:* Hydrogels show shape memory behaviour due to their capacity to absorb large amount of water because of their hydrophilic group content. These hydrogel SMPs can be lower solution critical temperature (LSCT) hydrogels that shrinks at temperatures above LSCT and swells at temperatures below LSCT, or higher solution critical temperature (HSCT) hydrogels that shrinks at temperatures below HSCT and swells at temperatures above HSCT. In this class of SMPs, temperature plays an important role in its SME. Polyacrylamide due to its LSCT has been applied in body temperature responsive shape memory hydrogel. Supramolecular type of SMPs are derived from non-covalent reactions such as van der Waals forces, dipole-dipole, and hydrogen bonds. These reactions improve stability of the polymer structure as well as act as the fixity phase. Supramolecular SMP's such as PEG

in PEG- $\alpha$ -CD, pyridine in PURs, PEG-PMMA-*co*-acrylic acid have been reported (Parameswaranpillai, et al., 2020).

### 3.3.2 Classification of SMPs based on external stimuli

Shape-memory polymers (SMPs) are stimuli-responsive materials and can change from their permanent shape to a temporary shape and return to their permanent shape when exposed to external stimulus (Parameswaranpillai, et al., 2020). External stimulus that are currently known include heat, light, moisture, electricity, and magnetism. SMPs that respond to heat are thermo-responsive SMPs. They are the most studied SMPs amongst all external stimuli (Xu & Jie, 2011).

When these SMPs are heated above the glass transition temperature or melting point of the hard segment, the polymer is shaped, and when cooled below the glass transition temperature or melting point of the hard segment, a permanent shape is formed and memorized. The temporary shape is formed by deforming the polymer at a temperature below the glass transition temperature or melting point of the hard segment but above the glass transition temperature or melting point of the soft segment, leading to the absorption of strain and stress by the soft segment. Then the deformed polymer is cooled below the glass transition temperature or melting point of the soft segment to fix the temporary shape. The temporary shape can return to the permanent shape by heating the SMP again below the glass transition temperature or melting point of the hard segment but above that of the soft segment (Figure 8) (Hu, 2007). Thermo-responsive SMPs have been reported in (Liu, et al., 2020; Navarro-Baena, et al., 2016; Luo, et al., 1997; Jianwen & Song, 2011).

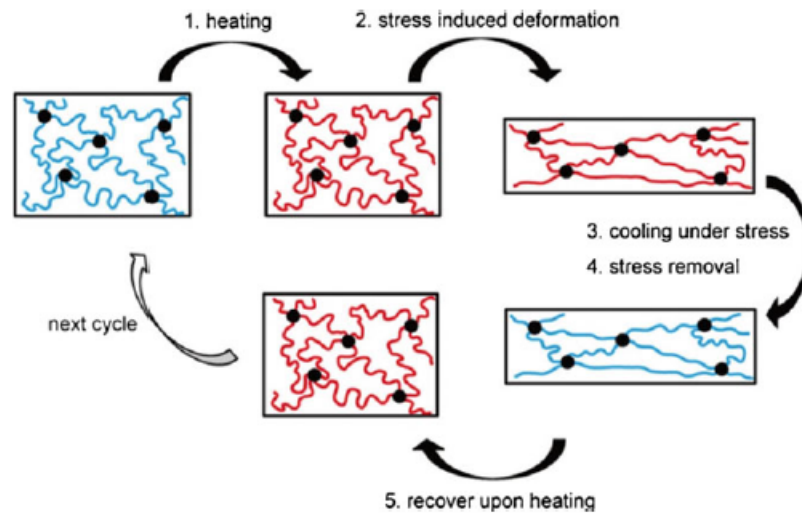


Figure 8. Schematic representation of a thermally induced shape memory effect (Parameswaranpillai, et al., 2020).

SMPs that respond to light are light stimuli SMPs and are often compared to thermo-responsive SMPs. Lu, et al. (2014) synthesized a light stimuli SMP by including carbon nanotubes (CNT) and boron nitride in epoxy based SMP. Addition of CNT and boron nitride to the SMP matrix improved its light absorption and thermal conductivity while the nitrides assisted in transferring heat to the SMP. Lendlein, et al. (2005) synthesized an UV light stimuli SMP by incorporating cinnamic groups. SMPs that respond to magnetic field are magnetic field sensitive SMPs and are synthesized by incorporating specific magnetic nanofillers into nanocomposite during preparation. The magnetic nanofillers generate heat when exposed to magnetic field and the nanocomposites recover their shape just like in thermally induced SMPs. Schmidt, (2006) incorporated magnetite nanoparticles into SMP composites of oligo( $\epsilon$ -caprolactone) dimethacrylate/butyl acrylate. The incorporated magnetite nanoparticles when exposed to external electromagnetic field transformed the energy from the field to heat.

### 3.3.3 Classification of SMPs based on shape-memory function

Shape memory polymers can show one-way, two-way, triple-way, multi-shape, and multifunctional shape memory effect. The one-way SMPs memorize only one permanent shape which is formed at a higher temperature and can deform into several temporary shapes which they have no memory of. Most thermo-responsive SMPs have one-way SME (Hu, 2007). First the permanent shape is formed and then the temporary shape is formed afterwards by a programming process such as heating, deforming, and cooling of the SMP. A shape memory effect is induced

by heating the temporary SMP above a transition temperature to obtain the permanent SMP (Marc & Andreas, 2007; Lendlein & Kelch, 2002; Parameswaranpillai, et al., 2020). One-way SMPs are not reversible and follow the direction in Figure 9. In contrast, two-way SMPs, which are also called shape changing polymers, are reversible and do not need the programming process to change to a temporary shape. Once the stimulus induced to recover the permanent shape is terminated, the temporary shape reforms. Two-way shape memory effect under constant stress has been observed in PCL where heating the PCL sample at high temperature recovers the permanent shape by contraction and cooling below the crystallization temperature reforms the PCL sample to a temporary shape by swelling. Two-way shape memory effect under constant stress has also been observed in crosslinked poly(cyclooctene) where cooling and heating of the sample corresponds to its tensile elongation and contraction (Hager, et al., 2015; Xie, 2011).

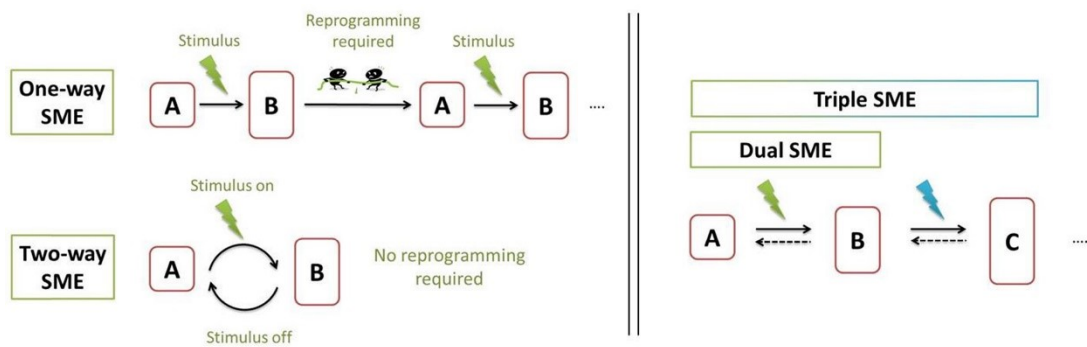


Figure 9. Schematic illustration of one-way, two-way, and triple -way shape memory effect (Hager, et al., 2015).

The triple-way SMP shows three different shapes, one permanent shape and two temporary shapes. One stimulus changes one temporary shape to the second temporary shape while a second stimulus changes the temporary shape to the permanent shape. Their design is based on wide-ranging thermal transitions and multiple phases which have different thermal transitions responsible for different shapes. Like the programming process in one-way SMP, the permanent shape SMP is heated above the thermal transition of both transitions, deformed, and finally cooled below the thermal transition of each stage while maintaining the deformation for each stage. Compared to the one-way and two-way SMPs that has one shape fixing and one shape recovery stage, the triple-way SMPs have two shape fixings and two shape recovery stages (Hager, et al., 2015; Xie, 2011; Parameswaranpillai, et al., 2020). Triple-way shape memory

has been reported in crosslinked polymer networks containing PCL and poly (cyclohexyl methacrylate) segment, and PCL and PEG segment. The triple-way SME was based on the  $T_m$  and  $T_g$  of PCL and poly (cyclohexyl methacrylate) in the first segment and the  $T_m$  of PCL and PEG in the second segment.  $T_m$  and  $T_g$  of PCL and poly (cyclohexyl methacrylate) were 50°C and 140°C respectively while the  $T_m$  of PEG ranged from 17-39°C depending on the PEG content. Multi-shape SMPs can also be synthesized just like triple shape SMPs by introducing extra different transitions. Quadruple SME has been reported in perfluorosulphonic acid ionomers based on their broad  $T_g$  (Hager, et al., 2015; Xie, 2011; Parameswaranpillai, et al., 2020; Xu & Jie, 2011). Multifunctional SMPs are designed based on unique requirements of some applications. These type of SMPs show shape memory effect and additional functionality such as biodegradability, permeability, etc, which is not related to SME. SMPs and drugs combined to produce drug delivery systems is an example of multifunctional SMP. Addition of magnetically active fillers such as iron oxide or electronically active fillers such as carbon nanotubes or carbon black to SMP network results in multifunctional SMPs that are stimulated by magnetic and electric field respectively (Parameswaranpillai, et al., 2020).

### **3.4 Techniques for preparing shape memory polymers**

#### **3.4.1 Chemical crosslinking of thermoplastics**

Chemical crosslinking of high MW thermoplastics is the best direct technique of preparing SMPs. By addition of organic peroxides and use of high radiation energy, this method introduces a network which hinders chain slippage and fixes the permanent shape. This method is suitable for both semi-crystalline and amorphous polymers using conventional processing techniques such as injection moulding, extrusion, and hot pressing however, significant changes in  $T_{trans}$  ( $T_m$  or  $T_g$ ) of the bulk polymers is expected. Heat shrinkable tubing which shows shape memory has been developed using radiation-crosslinked polyethylene (Parameswaranpillai, et al., 2020). Liu, et al. (2002) prepared a SMP by chemically crosslinking polycyclooctene (PCO) with dicumyl peroxide (DCP) using compression moulding and reported shape memory effect based on their crystallization and melting transitions.

### 3.4.2 Polymerization of monomers or prepolymers with crosslinkers

Another method to prepare SMP is to polymerize monomers or prepolymers with chemical crosslinkers in a single step. This method produces SMPs with tunable transition temperature, good shape memory properties and cycle stability. Also, the shape memory properties of the SMP can be efficiently controlled by modifying the content of the chemical crosslinker, the composition of the monomer or the MW of the prepolymer. However, limitation during processing due to high viscous nature of thermoset resins and narrow processing window due to gel time are the major drawbacks in this method. A well known example of this technique is the SMP prepared using a thermosetting epoxy resin and a chemical crosslinker. An aliphatic diamine crosslinker was introduced into the aromatic epoxide system which goes through a sol-gel transitions like other thermosets, giving a chemically crosslinked epoxy SMP (Parameswaranpillai, et al., 2020).

### 3.4.3 Synthesis of phase-segregated block copolymers

This method aims to prepare thermoplastic polymers that can be processed by conventional methods. These SMPs are usually phase-segregated block polymers consisting of two blocks that exhibit different thermal transition temperatures in which one block acts as the hard segment responsible for physical crosslinking and defines the permanent shape, and the other as the soft segment responsible for phase switching and defines the temporary shape (Parameswaranpillai, et al., 2020). Typical example is the SMP of PUR block copolymers consisting of 4,4'-Methylenebis (phenylisocyanate) with a thermal transition of 200°C and acting as the hard segment, and poly (tetramethylene glycol) with a thermal transition of 25°C acting as the soft segment (Lee, et al., 2001).

### 3.4.4 Physical blending of different polymers

This method provides an easy way to produce SMP owing to its mass production and good manufacturability. The blend is prepared by physically blending two polymers with one polymer having a higher  $T_g$  or  $T_m$  than the other. Based on the concept, the SMP blend usually contains one polymer acting as the soft segment and the other as the hard segment. These blends can be miscible or immiscible but still show shape memory. SMP polymers blends can also be

prepared by blending different polymers with a third component such as compatibilizer or a crosslinker which aims to improve shape memory properties and miscibility (Parameswaranpillai, et al., 2020). Miscible SMP blend consisting of TPU, and PVC has been reported. The PVC phase formed a miscible blend with the PCL segment in TPU acting as the switching phase while the hard segment in TPU was responsible for fixing the permanent shape. Shape memory was also reported in PUR/PCL blend where PCL was partially miscible with the PCL diol segment in PUR copolymer. Immiscible blend of poly(p-dioxanone) (PPDO)/PCL reportedly showed shape memory. The immiscibility in blend was improved when polyalkylene adipate was incorporated into the blend (Hu, 2014). See section 3.3.1 for more examples.

### **3.4.5 Composite**

SMP polymers composites are prepared with the aim to improve the mechanical properties of SMPs or introduce new functionalities to SMPs. This is prepared by blending different polymers with functional fillers. Incorporating reinforcement fillers such as carbon fibres, graphene, glass fibres, carbon nanotubes, Kevlar fibres, etc. can improve the mechanical and shape memory properties of SMPs. Incorporating functional fillers develops SMPs that can be actuated by other stimuli such as magnetic, electricity, light, etc. Conductive fillers such as carbon nanotubes and graphene generate heat when SMPC is exposed to voltage and transfers it to trigger shape memory in composite. Magnetic particles such as  $\text{Fe}_3\text{O}_4$  are incorporated in SMPs to develop magnetic-actuated SMPs. Hydrophilic cellulose nanowhisker has been incorporated in SMPs to develop solvent actuated SMPs (Parameswaranpillai, et al., 2020).

## **3.5 Characterization techniques for shape memory polymers**

### **3.5.1 Scanning electron microscopy (SEM)**

The scanning electron microscopy is a technique used to study the morphology of SMPs. It gives an image of the polymer surface which describes its surface topography by scanning a focused electron beam with diameters between 5-10nm across the polymer surface. The electron beam interacts with atoms in the polymer and are inelastically scattered, emitting electrons which produce magnified images. SEM has magnification ranging from 20-100,000 and allows 3D images to be retrieved (Hemjyoti, 2018; Hu, 2007). Liu, et al. (2020) investigated the morphology of PLA/PCL blends using a field-emission SEM and reported phase-separated

morphologies, corresponding to the results reported by Navarro-Baena, et al. (2016) and described as immiscibility in polymer blends. They also reported a relationship between shape recovery ( $R_r$ ) and PLA/PCL interfaces where  $R_r$  decreased with increasing PCL content which they attributed to the restriction to viscous flow of PCL molecular chains by physical crosslinking at the interfaces which decreased as PCL contents increased, causing the irreversible slippage of PCL molecular chains and consequently, decreasing  $R_r$  during the shape memory cycle (Liu, et al., 2020). Guo, et al. (2018) investigated the morphology of PLA/PEG blends and reported compatibility for 5-15 wt.% PEG in blends while a phase separation occurred when the PEG content was above 15 wt.%. The phase separation was attributed to the solubility limit of PEG in PLA polymer which is between 15-30 wt.% depending on its molecular weight. Similarly, Jing, et al. (2015) used SEM to study the morphology of PLA/TPU and a phase separation signifying immiscibility, was reported in all blends. The phase separation was observed to increase with increasing TPU content.

### **3.5.2 Differential scanning calorimetry (DSC)**

To develop the programming process for the temporary shape, thermal properties in shape-memory polymers need to be determined. Differential scanning calorimetry is the common thermoanalytic technique for determining the thermal properties of polymer materials. It uses the differential scanning calorimeter to monitor the thermal properties by measuring the difference in thermal properties of a sample as a function of temperature and time (Parameswaranpillai, et al., 2020). DSC detects parameters such as glass–rubber transition temperature ( $T_g$ ), melting temperature ( $T_m$ ), crystallization temperature ( $T_c$ ), melting enthalpy ( $H_m$ ), crystallization enthalpy ( $H_c$ ), etc. Usually, the sample material and an inert reference material, typically platinum or alumina, which does not go through structural modification and thermal transition, are utilised in the test. Equal temperatures are maintained in both sample and reference material afterwards the thermal transition of the sample is determined by measuring the difference in energy required to keep both materials in the same temperature (Parameswaranpillai, et al., 2020). The experiment is comprised of three cycles carried out in a standard aluminium pan. In the first cycle, the test samples are heated to high temperatures usually between 200 -250°C and maintained at that temperature for 5 minutes to erase their thermal history. Then they are cooled down to very low temperatures (-80-0°C). Finally, they are heated again to high temperatures between 200-250°C and their thermal properties explored.

These three cycles are usually carried out at heating rates typically 10-20°C/min (Guo, et al., 2018; Lai & Lan, 2013; Jing, et al., 2015).

Liu, et al. (2020) explored the crystallisation and melting behaviours of PLA/PCL blends using DSC analysis and reported the poor crystallization behaviour of PLA, in contrast to PCL. Neat PCL exhibited better crystallization than neat PLA. In the blends, PCL crystallization was inhibited when its content was low while PLA still did not show melt crystallization which was attributed to the slow rate of PLA crystallization. The blends with 30 wt.% PCL content and less enhanced PLA crystallization while those with PCL content above 30 wt.% inhibited PLA crystallization. Result from their DSC analysis also showed that PCL had lower  $T_m$  and functioned as the reversible phase (soft segment) for the temporary shape while PLA showed higher  $T_m$  and functioned as the fixed phase (hard segment) for the permanent shape. Crystallization of the reversible phase was observed to influence shape memory properties such as shape fixity ( $R_f$ ) and shape recovery ( $R_r$ ) values where the high  $R_f$  values obtained were attributed to the good crystallization capacity of PCL. Navarro-Baena, et al. (2016) also reported the poor crystallization behaviour of PLA, compared to PCL which crystallized completely. The crystallinity of PLA in the blends increased with increasing PCL content similarly as was reported by Liu, et al. (2020) but for low PCL content.

Guo, et al. (2018) studied the thermal properties of PLA/PEG blends using DSC analysis and observed poor crystallization behaviour of neat PLA with an improved crystallization behaviour when blended with 5-10 wt.% PEG. DSC curve revealed a phase separation when the PEG content was above 20 wt.% which was attributed to the solubility limit of PEG in PLA polymer. Study also showed the PEG content in blends influenced the  $T_g$  of PLA. As reported in Yu-Chen, et al. (2019), increasing the PEG content decreased the  $T_g$  value of PLA to a point and indicated less energy requirement for phase transition. This was attributed to the flexibility effect of PEG on the polymer chains as  $T_g$  values indicate flexibility of chains with lower  $T_g$  corresponding to high flexibility and vice versa. Also, the shape recovery temperature of blends was observed to be close to their  $T_g$  from DSC. Jing, et al. (2015) reported immiscibility in PLA/TPU SMP blend during thermal studies using DSC. This was observed when PLA and TPU showed different  $T_g$ . Study also showed that TPU impedes the cold crystallization of PLA since cold crystallization of PLA in blends decreased with increasing TPU content and TPU did not show cold crystallization behaviour like PLA.

### 3.5.3 Static tensile test

It is important that before changing the shape of a SMP, it has enhanced static mechanical strength. While performing static tensile tests, applied strain or stress including strain rate can be varied but temperature is fixed (Parameswaranpillai, et al., 2020). Ohki, et al. (2004) carried out this test on a SMP at constant tensile speed in a temperature-controlled chamber. The strain was then calculated as:

$$\frac{\text{elongation obtained by the crosshead displacement}}{\text{gage length}} \quad (5)$$

A stress–strain curve is usually obtained from this test which is used to assess the tensile properties of the SMP such as young’s modulus, stress at break and yield point including elongation at break (Parameswaranpillai, et al., 2020).

Guo, et al. (2018) reported modulus and elongation at break for PLA/PEG blends using the tensile tests. Result showed that neat PLA exhibits high modulus but displayed very low elongation at break which limits its application as shape memory polymer. When blended with PEG, the elongation at break improved up to 209% but the modulus reduced, showing that PEG exhibits high elongation properties suitable for SMP but with lower modulus. This tensile behaviour of PLA/PEG blends are similar to what was reported by Yu-Chen, et al. (2019).

Jing, et al. (2015) and Navarro-Baena, et al. (2016) also reported modulus, tensile strength, and elongation at break for PLA/TPU and PLA/PCL blends respectively, where neat PLA showed high modulus and tensile strength but poor elongation at break. When PLA was blended with TPU and PCL, their elongation at break increased but their modulus and tensile strength decreased due to the poor tensile strength of TPU and PCL.

### 3.5.4 Dynamic mechanical analysis (DMA)

Shape-memory polymers (SMPs) and all polymers in general show strong viscoelastic behaviour which plays an important role in their shape memory effect. Therefore, when handling SMPs, it is vital that the viscoelastic behaviour is described with suitable models based on certain parameters. Dynamic mechanical analysis is among the most important techniques used to

determine the viscoelastic mechanical behaviour of polymers (Parameswaranpillai, et al., 2020). It is the preferred technique to measure glass transition temperature and minor phase transitions in polymers (Ebnesajjad & Ebnesajjad, 2014).

During this test, sample is placed in the DMA apparatus which has a defined frequency, domain, and a temperature interval (Roudbarian, et al., 2019). A cyclically force is applied on the sample and the mechanical behaviour is obtained while observing the stress-strain relationship in a varied temperature. The storage modulus, loss modulus and  $\tan \delta$  are the measured properties with this method. The storage modulus and loss modulus describe the dynamic properties of the polymer and is defined as

$$E^* = (E'^2 + E''^2)^{\frac{1}{2}} = E' + E'' \quad (6)$$

Where  $E^*$  is the complex dynamic modulus;  $E'$  is the storage modulus which is defined as strain energy that can be stored and equates young modulus at small loadings;  $E''$  is the loss modulus related to the heat dissipation while  $\tan \delta$  is the angle for phase change and calculated as (Hu, 2007).

$$\tan \delta = \frac{E''}{E'} \quad (7)$$

Temperatures between -100 to 100°C (Hu, 2007), -20 to 90°C (Roudbarian, et al., 2019), 30 to 90°C (Parameswaranpillai, et al., 2020), frequencies between 5-20Hz (Roudbarian, et al., 2019), 0.1-180Hz (Parameswaranpillai, et al., 2020) and heating rate between 2-5°C/min have been reported in literature for different DMA apparatus and SMPs.

DMA carried out by Liu, et al. (2020) revealed the viscoelastic mechanical behaviour and  $T_g$  of PLA/PCL SMP blend. Neat PLA showed higher storage modulus than Neat PCL. Hence the blends with 10-60 wt.% PCL showed higher modulus than neat PCL due to the contribution of PLA to the storage modulus which also decreased with increasing PCL content. The  $T_g$  of PCL did not change in blends, signifying immiscibility between the two polymers. Analysis also showed that when temperature was above the  $T_g$  of PCL but below that of PLA, relaxation of PCL molecular chains occurred and the PCL phase in blends transitioned from glassy to rubbery state leading to a huge decrease in storage modulus ( $E'$ ) of PCL while PLA remained glassy.

When temperature was above the  $T_g$  of PLA, both transition of PCL phase from rubbery to viscous state due to viscous flow of PCL molecular chains and transition of the PLA phase from glassy to rubbery state resulted in a drastic decline in  $E'$  of the blend. DMA also showed decreasing  $T_g$  of PLA phase with increasing PCL content for blends of 20 wt.% and below signifying the plasticizing effect of PCL on PLA matrix for small amounts of PCL. This plasticizing effect was also reported by Navarro-Baena, et al. (2016). Value at  $\tan \delta$  peak was evaluated for different blends with reference to that of neat PLA, where values below the reference value indicated lower internal friction and stable physical crosslinking at the interfaces successfully restricting the viscous flow of PCL molecular chains. Restriction to the viscous flow of PCL molecular chains due to stable physical crosslinking at the interfaces causes the reversible slippage of PCL molecular chains and consequently, increasing  $R_r$  during the shape memory cycle (Liu, et al., 2020).

Guo, et al. (2018) reported decreasing  $T_g$  of PLA with increasing PEG content for PLA/PEG SMP blend, confirming the plasticizing effect of PEG of PLA observed by Yu-Chen, et al. (2019). This was observed from the  $\tan \delta$  curves during DMA. Storage and loss modulus in the blends decreased with increasing PEG content since PEG had a lower modulus than PLA. Lai & Lan, (2013) observed two glass transition temperatures from  $\tan \delta$  curves of PLA/TPU SMP blend, signifying their thermodynamic immiscibility. The  $T_g$  of PLA was not affected by the varying content of TPU, further confirming their immiscibility. Liu, et al. (2020) also observed a decrease in storage modulus ( $E'$ ) of PLA when the temperature reached the  $T_g$  of PLA and a decrease in storage modulus ( $E'$ ) of blends with increasing TPU content.

### 3.6 Characterization techniques for shape memory properties

Shape memory properties of SMPs are usually determined using the conventional and dynamic (cyclic) mechanical tests, respectively. A polymers shape memory property is best described by the strain recovery and strain fixity which is usually quantified by the cyclic mechanical test (Parameswaranpillai, et al., 2020). The strain fixity ( $R_f$ ) measures the ability to fix a mechanical deformation  $\varepsilon_m$  which is causing a temporary shape  $\varepsilon_u(N)$  where  $N$  is the number of cycles, and  $R_f$  is given as:

$$R_f(N) = \frac{\varepsilon_u(N)}{\varepsilon_m} \times 100\% \quad (8)$$

Strain recovery ( $R_r$ ) measures the ability of the polymer material to return to its permanent shape  $\varepsilon_p(N)$  after a mechanical deformation  $\varepsilon_m$  has been applied and is measured as the ratio between the recorded change in strain during shape-memory effect and the change in strain while programming (Marc & Andreas, 2007). This is given as:

$$R_r(N) = \frac{\varepsilon_m - \varepsilon_p(N)}{\varepsilon_m - \varepsilon_p(N-1)} \times 100\% \quad (9)$$

### 3.6.1 Thermomechanical cyclic test

The thermomechanical test methods have been established for the mostly used heat stimuli. This test is used to quantify the shape memory properties of SMPs. The test determines the switching temperature ( $T_{\text{trans}}$ ), strain recovery rate ( $R_r$ ) and strain fixity rate ( $R_f$ ) of the material (Marc & Andreas, 2007). In a typical test procedure, measurements are carried out with a tensile tester in a thermo-chamber. Several test procedures such as controlled strain or stress, cold drawing (at  $T_{\text{low}} < T_{\text{trans}}$ ) and temporary heating (at  $T_{\text{high}} > T_{\text{trans}}$ ) are demonstrated (Lendlein & Kelch, 2002). The polymer is fastened to the tensile tester in a thermo-chamber, heated to temperatures ( $T_{\text{high}}$ ) above switching temperature ( $T_{\text{trans}}$ ) but below highest transition temperature  $T_{\text{perm}}$  and stretched to a preferred strain  $\varepsilon_m$ . The strain is maintained for a while to allow the polymer chains to relax after which the stress-controlled experiment is maintained. Under constant stress  $\sigma_m$ , the test specimen is cooled to  $T_{\text{low}}$  below  $T_{\text{trans}}$ , consequently fixing the temporary shape. The strain is decreased afterwards till a stress-free condition is accomplished at 0 MPa,  $\varepsilon_u$ . The polymer is heated again to temperatures ( $T_{\text{high}}$ ) above switching temperature ( $T_{\text{trans}}$ ) as the tensile stress is held constant at 0 MPa, leading to the contraction of the specimen and recovery of its permanent shape (Figure 10) (Marc & Andreas, 2007).

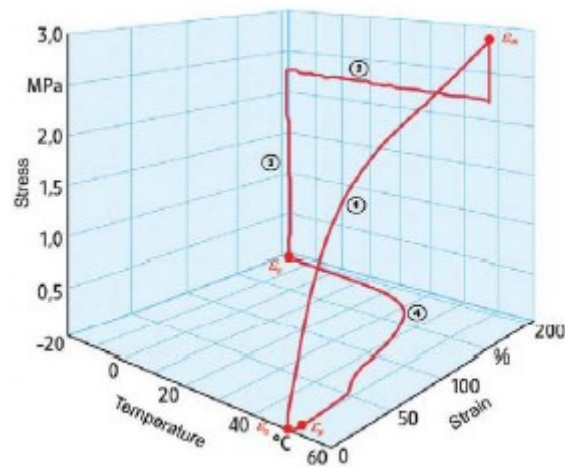


Figure 10. Diagram of a cyclic thermomechanical experiment. Step 1 is controlled by strain while steps 2 to 4 till the start of the next cycle are controlled by stress (Marc & Andreas, 2007).

Liu, et al. (2020) reported excellent shape memory properties for PLA/PCL SMP blend conducted using a stress-controlled DMA. The  $R_f$  values calculated for the blends were above 95% which increased with increasing PCL content and decreased when the PLA content was below 50 wt.%. The  $R_r$  values calculated increased followed by a decrease with the blend with 20 wt.% PCL content having the highest  $R_r$ . Also, as PCL content increased, the maximum temporary strain increased and the strain between 15-200% had little effect on the shape memory behaviour. The high  $R_f$  values obtained were attributed to the good crystallization capacity of PCL, and the crystallization increased as PCL content in the blends increased. When the reversible phase was not completely crystallized, a portion of the deformation energy produced during forced deformation was dispersed during stress relaxation. This resulted in lower  $R_f$  values in the case of 10 and 20 wt.% PCL, due to insufficient internal stress required to restore the original state of the PCL molecular chain being stored in the PCL crystals. They also found that the crystallization of the reversible phase PCL was not the key factor influencing the  $R_f$  since the  $R_f$  values decreased as crystallization of PCL increased with increasing PCL content and that the fixed phase had little or no influence on the  $R_r$  values since the PLA molecular chains are still frozen during deformation temperature. Further study confirmed that the physical crosslinking at the interfaces of the reversible and fixed phase and the  $T_g$  of the fixed phase were key factors influencing the  $R_f$  values.

Guo, et al. (2018) investigated the shape memory properties for PLA/PEG SMP blend at different strains (50-250%) and recovery temperatures, and reported tensile strain, recovery

temperature, stretch strain rate and deformation temperature as the main factors influencing the shape memory behaviours.  $R_f$  and  $R_r$  values were greater than 86% and 65% respectively for all strains.  $R_f$  and  $R_r$  values decreased with increasing PEG content, contrary to what was reported by Yu-Chen, et al. (2019) where  $R_r$  increased with increasing PEG content. A slight decrease for 5-20 wt.% blends and a sharp decrease when the PEG content was above 20 wt.% was observed, signifying a phase separation in blends. They attributed the decreasing  $R_f$  and  $R_r$  values to the increasing irreversible deformation caused by PEG, although the blends with proper PEG contents maintained relatively high values. The  $R_f$  values also increased with increasing strain for same PEG content while the  $R_r$  values decreased with increasing strain for same PEG content, stating that  $R_f$  and  $R_r$  values depend on one another with high  $R_f$  corresponding to low  $R_r$ .  $R_f$  and  $R_r$  values were higher for higher strain rate because relaxation of molecular chain occurs at low strain rate. Optimum  $R_r$  values (>80%) were achieved at 70°C for all blends, making it the maximum recovery temperature. Maximum  $R_f$  and  $R_r$  were obtained at a deformation temperature of 60°C.

Jing, et al. (2015) reported  $R_f$  and  $R_r$  values >90% for all blends of PLA/TPU, showing their excellent shape memory properties. They reported shape memory properties for three cycles of the blends except the blend with 80 wt.% PLA which broke during the third cycle due to high PLA content. The  $R_f$  and  $R_r$  values as well as the ease to deform the sample increased with increasing TPU content, which was attributed to the intrinsic flexibility of TPU. Lai & Lan, (2013) also reported high  $R_f$  and  $R_r$  values for PLA/TPU blends, signifying good shape memory behaviour.  $R_r$  increased with increasing TPU content and increasing recovery temperature while  $R_f$  decreased with increasing predeformation temperature as  $R_f$  decreased.

### 3.6.2 Bending test

Bending test is a technique used to illustrate the cycle-life of the SMP. The SMP sample is bent to a given angle  $\Theta_{max}$  and at a temperature ( $T_{high}$ ) higher than the switching temperature ( $T_{trans}$ ). The bent sample is cooled at a temperature ( $T_{low}$ ) below the switching temperature, the stress applied is released and the sample returns a bit to an angle  $\Theta_{fixed}$ . Finally, the bent sample is heated again above  $T_{trans}$  and as temperature increases, a series of angles  $\Theta_i$  (T) are recorded as the sample slowly recovers its original shape. At  $\Theta_{final}$ , the sample has fully recovered its original shape (Hu, 2007).

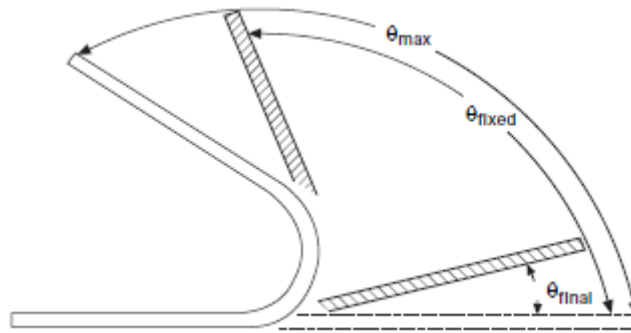


Figure 11. To illustrate the bending test ( (Hu, 2007).

The measured properties after the test are the shape fixity rate ( $R_f$ ) and shape recovery rate ( $R_r$ ) which is given as:

$$R_f = \frac{\theta_{fixed}}{\theta_{max}} \times 100\% \quad (10)$$

$$R_r = \frac{\theta_{fixed} - \theta_{final}}{\theta_{fixed}} \times 100\% \quad \text{or} \quad (11)$$

$$R_r(T) = \frac{\theta_{max} - \theta_i(T)}{\theta_{max}} \times 100\% \quad (12)$$

Where  $R_r(T)$  is the shape recovery at temperature ( $T$ ) above the switching temperature, which the sample has been heated to (Hu, 2007). Jing, et al. (2015) reported excellent shape memory properties for PLA/TPU using bending test. They obtained  $R_f$  values  $>76\%$  and  $R_r$  values  $>91\%$  for all blends for three cycles. Similarly, Shen, et al. (2012) reported excellent shape memory properties for PLA/PEG using bending test.  $R_f$  and  $R_r$  values  $>91\%$  were obtained for all blends.

### 3.6.3 Heat shrinkage measurement

The test sample is stretched at room temperature and a constant strain (0.2 MPa) is maintained after which the sample is heated above  $T_{trans}$ . The heat shrinkage is then calculated as

$$\text{Heat shrinkage (\%)} = \frac{l_{str} - l_s}{l_{str} - l_o} \times 100 = \frac{l_{str} - l_s}{l_{str}(1 - \lambda^{-1})} \times 100 \quad (13)$$

Where  $l_{str}$  and  $l_s$  is the length of the test sample after stretching and after shrinkage process respectively,  $l_o$  is the original length of test sample and  $\lambda$  is the ratio of  $l_{str}/l_o$  i.e., the draw

ratio. The heat shrinkage experiment is temperature dependent  $l_s(t)$  and is determined as a function of time for a known  $T_{high}$  (Lendlein & Kelch, 2002).

### 3.7 Characterization techniques for self-healing properties

Self-healing properties of SMPs are usually determined using their fractured or notched specimen. First the specimen is placed in a tensile testing machine and pulled along its longitudinal axis at a particular strain. The strained specimen is placed in an oven set at a  $T_m$  higher than the  $T_m$  of the soft segment but lower than that of the hard segment to recover its original shape. This first step is done twice. Then notches are placed on the specimen after which it is stretched and then heated in an oven for a period for recovery and self-healing. Finally, the healed specimen is placed in a tensile testing machine and pulled along its longitudinal axis at a particular strain again. The degree of healing is calculated using the equation below:

$$\%_{heal} = \frac{P_{healed} - P_{notched}}{P_{virgin} - P_{notched}} \times 100 \quad (14)$$

Where  $P_{healed}$ ,  $P_{notched}$  and  $P_{virgin}$  is the tensile strength of the healed, notched, and virgin SMPs respectively (Bhattacharya, et al., 2020).

Bhattacharya, et al. (2020) reported the self-healing behaviour of thermoplastic blends of TPU and PCL for 10-60 wt.% PCL content. Fractured surface of a sample of the blend was observed to come in close contact after heating at 90°C for 30 minutes. Upon heating at a temperature higher than the  $T_m$  of PCL but below that of TPU, they observed the flow and redistribution of molten PCL into the fractured surface thereby enhancing self-repair. The self-healing mechanism was attributed to the reversible plasticity SME. They also observed that blends with high PCL content did not show considerable self-healing properties and this was attributed to their poor mechanical properties at high temperatures and necking tendency during fracturing. Seal healing properties of other SMPs have also been reported in Hager, et al. (2015).

### 3.8 Applications

SMPs have several applications in biomedical structures. Sutures, prosthetics, catheters, nails, drug delivery devices, tubes, implants, orthopaedic devices, and contact lenses can be produced using SMPs (Hu, 2007; Jianwen & Song, 2011; Hager, et al., 2015). SMP was applied in designing a biodegradable self-tying suture. The suture was applied to a wound as loose knots and on stimulation at 41°C, recovered its permanent shape and tightened the knots (Hu, 2007). A photothermally activated SMP have been applied in treating stroke (blood clot). The SMP is introduced into the blood vessel via a catheter and on photothermal activation, recoils to its permanent shape resulting to a mechanical removal of blood cloth and consequently, relieve of deficient blood supply. SMPs have been applied in biodegradable intragastric implants used in treating obese patients. These implants inflate after a programmed time and give the patient a satiety feeling after consuming a little quantity of food. Similar to the working principle above, biodegradable SMPs have been applied in designing vascular stents which show easier drug elution and improved healing properties (Marc & Andreas, 2007; Jianwen & Song, 2011; Hager, et al., 2015).

SMPs have been applied in designing self-healing devices used to repair mechanical damage. These self-healing devices are designed by inserting a healing agent (such as a capsule) in the polymer or by employing the special functional properties of the polymer such as reversible interactions. When applied to cracked surfaces, the self-healing device due to their shape memory property pull the cracked surfaces together thereby enhancing the healing process (Hager, et al., 2015; Parameswaranpillai, et al., 2020).

Potential application of SMPs in solar rails and arrays, radar antennas or sunshields in aerospace industry is of great interest (Hager, et al., 2015). SMPs have various applications in the textile and clothing industries for products such as shoes, breathable fabrics, and wrinkle and shrink-resistant finishes for clothing. SMP-based clothing recovers their permanent shape (wrinkle-free) after they are wrinkled during wear by subjecting them to higher temperature during washing. Also, shape memory fibres (SMF) made from SMPs by various spinning methods have found several applications in the textile industries (Parameswaranpillai, et al., 2020).

### 3.9 Polymer selection

Choosing polymers for designing SMP is based on the desired  $T_g$  for polymer network containing no less than one amorphous segment, or  $T_m$  for polymer network containing no less than one crystalline segment. This in turn depends on the desired application and environment where they will be utilised. Thermoplastic and thermoset polymers can be used although thermoplastics are usually preferred because of their easier moulding. Thermoset polymers become hard when heat and pressure is applied due to formation of stable three-dimensional network, and therefore cannot be reprocessed. The thermoplastics unlike the thermosets can be reprocessed. They melt when heated and solidify when cooled, hence can be repetitively remelted (Langer, et al., 2000; Vlachopoulos & Strutt, 2003).

## 4. MATERIAL AND METHODS

### 4.1 Materials

Material purchased for experiment, their properties and functions are listed on Table 7, and a flowchart detailing the experimental steps and methods is given in Figure 12.

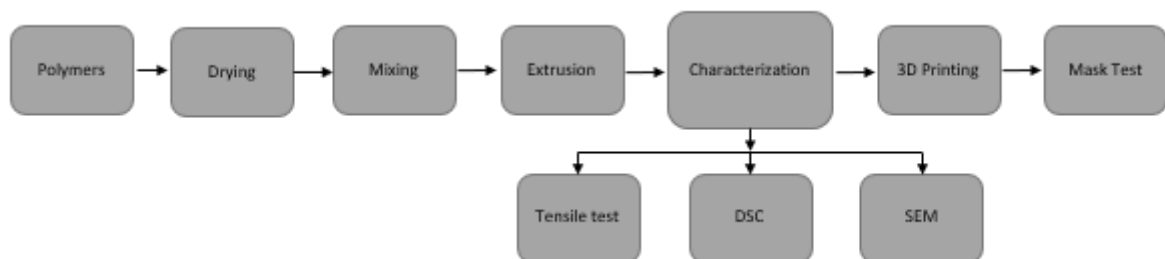


Figure 12. Flowchart of experimental methods (Source: Author).

Table 7. Materials for experiment.

Material	$M_w/M_n$	Density (g/cm <sup>3</sup> )	MFI (g/10min)	$T_m$ (°C)	Form	Function in blend	Purchased
Poly(lactic acid) (PLA)		1.24	6	175	Filament	Polymer	3D-CAD solutions Tampere Finland
Polycaprolactone (PCL)	$M_n \sim 80000$	1.145	2.01-4.03 (160°C/5kg)	60	Pellets (~3 mm)	polymer	Sigma-Aldrich Finland
Polypropylene (PP)	$M_w \sim 340000$ $M_n \sim 97000$	0.9	4 (230°C/2.16kg)	160-165	Pellets	Polymer	Sigma-Aldrich Finland
Low density polyethylene (LDPE)		0.918	1 (190°C/2.16kg)	100-125	Pellets	Polymer	Sigma-Aldrich Finland
Poly (1,4-butylene adipate) (PBA)	$M_w \sim 12000$	1.019		56-60	Chips	Polymer	Sigma-Aldrich Finland
Poly (ethylene glycol) (PEG)	$M_n \sim 4000$			58-61	Pellets	Polymer	Sigma-Aldrich Finland
Polyethylene-graft-maleic anhydride (PE-g-ma) ~0.5 wt.% maleic anhydride		0.92		107	Pellets	Compatibilizer	Sigma-Aldrich Finland
Polypropylene-graft-maleic anhydride (PP-g-ma) ~8-10 wt.% maleic anhydride	$M_w \sim 9100$ $M_n \sim 3900$	0.934		156	Pellets	Compatibilizer	Sigma-Aldrich Finland
Poly (ethylene glycol) methyl ether- block -poly ( $\epsilon$ -caprolactone) (PEG-b-PCL)	PEG Av. $M_n$ 5,000, PCL Av. $M_n$ 25,000			63-68	Chunks	Compatibilizer	Sigma-Aldrich Finland
Poly (ethylene glycol)-Poly (propylene glycol)-Poly (ethylene glycol) block copolymer (PEG-PPG-PEG)	$M_n \sim 5800$			39	Semi- solid	Additive	Sigma-Aldrich Finland

## 4.2 Extrusion of polymer blend

Polymer pellets were dried at 40°C in an oven for 12h and mechanically premixed in a zipped bag to obtain homogenous mixture before melt blending. The weight ratios of the premixed blends are given in Tables 8-10. 3D filaments of the polymer blends were prepared using an extruder (Filabot EX2 extruder, FB00720, USA) at temperatures 20-30°C higher than their given melting temperatures. Figure 13 shows the Filabot EX2 extruder set up used for polymer extrusion. The setup consists of the extruder, the airpath and the spooler. The extruder device has a speed and temperature control screen, a hopper, a three-stage screw for mixing and interchangeable nozzles. The melt-blended polymer mixture exits the extruder nozzle, passes through the Filabot Airpath where they are cooled and finally gathered with the Filabot spooler.

Table 8. Weight ratios of the premixed PP blends

Sample	Base Polymers		Compatibilizer
	PP (wt.%)	PCL (wt.%)	PP-g-ma (phr)
PP100	100	-	-
PP 90PCL10	90	10	-
PP80PCL20	80	20	-
PP70PCL30	70	30	-
PP90PCL10C1.25	90	10	1.25
PP80PCL20C1.25	80	20	1.25
PP70PCL30C1.25	70	30	1.25
PP90PCL10C5	90	10	5
PP80PCL20C5	80	20	5
PP70PCL30C5	70	30	5
PP90PCL10C10	90	10	10
PP80PCL20C10	80	20	10
PP70PCL30C10	70	30	10

Table 9. Weight ratios of the premixed PLA blends

Sample	Base Polymers		Additive
	PLA (wt.%)	PCL (wt.%)	PEG-PPG-PEG
PLA100	100	-	-
PLA90PCL10	90	10	-
PLA80PCL20	80	20	-
PLA70PCL30	70	30	-
PLA60PCL40	60	40	-
PLA50PCL50	50	50	-
PLA40PCL60	40	40	-
PLA60PCL40C5	60	40	5
PLA60PCL40C7.5	60	40	7.5
PLA60PCL40C510	60	40	10
PLA70PCL30C5	70	30	5
PLA70PCL30C7.5	70	30	7.5
PLA70PCL30C10	70	30	10
PLA80PCL20C2.5	80	20	2.5
PLA80PCL20C5	80	20	5
PLA80PCL20C7.5	80	20	7.5
PLA80PCL20C10	80	20	10

Table 10. Weight ratios of the premixed LDPE blends

Sample	Base Polymers		Compatibilizer
	LDPE (wt.%)	PCL (wt.%)	PE-g-ma (phr)
LDPE100	100	-	-
PCL	100		
LDPE90PCL10	90	10	-
LDPE80PCL20	80	20	-
LDPE70PCL30	70	30	-
LDPE90PCL10C	90	10	10
LDPE80PCL20C	80	20	10
LDPE70PCL30C	70	30	10



Figure 13. Filabot EX2 extruder set up used for extrusion.

### 4.3 3D printing

#### 4.3.1 Filament testing

The suitability of the prepared filament (polymer blends) for 3D printing was investigated conducting 3D printing trials on a simple rectangular model. An FDM printer (Prenta Duo, Prenta Oy, Finland) was used to produce the model. First a rectangular 3D model was designed and loaded into a slicing software (Slic3r). The model was dimensioned as 25 mm (length)  $\times$  6 mm (width)  $\times$  3 mm (thickness). The printing parameters on the slicing software such as printing speed, bed temperature, nozzle temperature, layer thickness, raster angle and infill density were adjusted to create the G-code of the rectangular model. Then the extruded filaments of 1.75mm (diameter) were fed into the FDM printer where the heated nozzle of the printer scanned around the printing bed matching the coordinate location identified by the G-code to produce the rectangular model.

#### 4.3.2 Mask 3D printing

A FDM printer (Prenta Duo, Prenta Oy, Finland) was used to produce the mask. First a 3D model was designed and loaded into a slicing software (Slic3r). The printing parameters on the slicing software such as printing speed, bed temperature, nozzle temperature, layer thickness, raster angle and infill density were adjusted to create the G-code of the mask 3D model. Then the prepared filaments from extrusion were fed into the FDM printer where the heated nozzle of the printer scanned around the printing bed matching the coordinate location identified by the G-code to produce the 3D model. The mask to be printed contained 4 parts; the mask body,

filter connector, filter holder and the cap. The filter connector, holder and cap were printed with pure filament while the mask body responsible for mask fit were printed using the prepared and selected shape memory filaments.

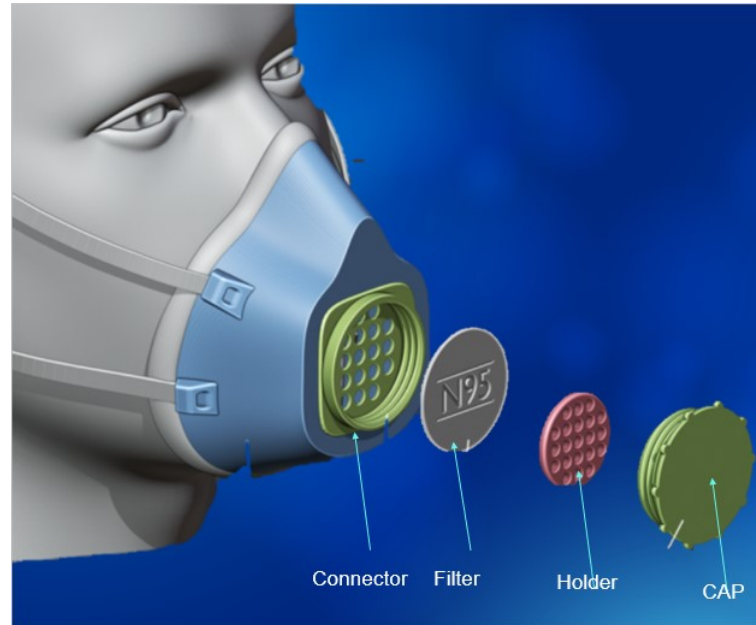


Figure 14. The mask designed to be printed.

#### 4.4 Characterization

Only successfully extruded materials were characterized. Characterized blends were PLA/PCL blends, PP/PCL blend, LDPE/PCL blends and their compatibilized blends.

##### 4.4.1 Tensile test

The mechanical properties of the filaments were tested using the universal testing machine (Zwick Roell Z020) at a selected cross head speed of 30mm/min and load of 20kN. These mechanical properties describe how much load and force the polymer sample can withstand before failure. A minimum of five samples each were cut from the filaments into 165mm length. The cut samples were conditioned for 72 hours in a conditioning chamber set to 65% relative humidity and temperature of 23°C. The tests were carried out at room temperature and samples were placed between pneumatic grips of the testing machine, leaving 22mm distance between clamps. The test sample was pulled along its longitudinal axis till it broke or reached the specified limit. The strain, stress, and young modulus (E) were obtained from this experiment

using the TestXpert II software, and the tensile strength, young modulus, and elongation at break of the filaments were obtained from the average of 5-6 tested samples.

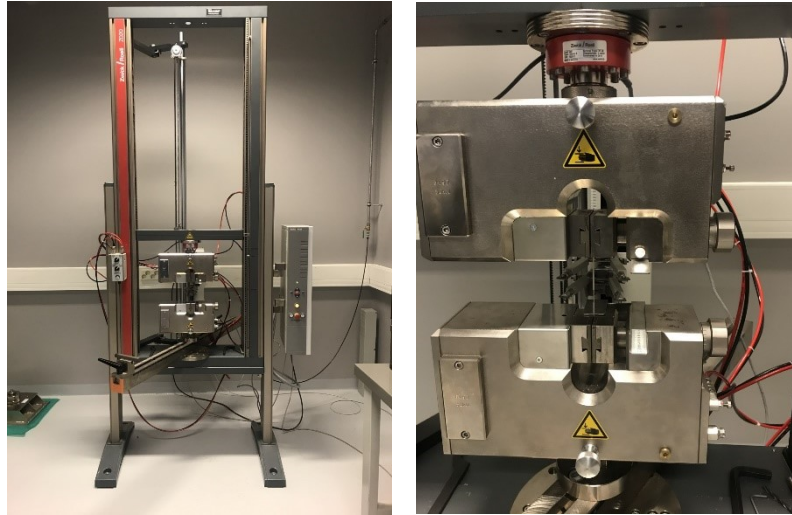


Figure 15. Zwick universal tensile tester setup used for tensile testing.

#### 4.4.2 Differential Scanning Calorimetry (DSC)

The melting and crystallization behaviours of the extruded filaments were investigated using differential scanning calorimeter (DSC 204FI, NETZSCH). The melting temperature, glass transition, crystallization temperature, melting enthalpy and crystallization enthalpy of the extruded filaments were studied with respect to heat flow rate. During the test,  $3 \text{ mg} \pm 0.7$  of each filament was weighed, sealed in an aluminium pan with pierced lid and placed in the DSC instrument operating under nitrogen atmosphere flowing at  $20 \text{ mL/min}$ . The sample in DSC was first heated from  $20^\circ\text{C}$  to  $200^\circ\text{C}$  at a heating rate of  $10 \text{ K/min}$  to erase their thermal record. While maintaining same heating rate, the sample was cooled from  $20^\circ\text{C}$  to  $-50^\circ\text{C}$  and finally heated again from  $-50^\circ\text{C}$  to  $200^\circ\text{C}$ . Three curves, first heating scan, second heating scan and cooling scan were obtained from this experiment. The degree of crystallization of PLA ( $X_{c, \text{PLA}}$ ) in blends was calculated from equation 15 assuming a melting enthalpy of  $93.6 \text{ J/g}$  at 100% crystallization of PLA (Liu, et al., 2020). The degree of crystallization of PCL ( $X_{c, \text{PCL}}$ ), LDPE ( $X_{c, \text{LDPE}}$ ) and PP ( $X_{c, \text{PP}}$ ) in blends were calculated from equation (16) assuming a melting enthalpy of  $136 \text{ J/g}$ ,  $293 \text{ J/g}$ , and  $205 \text{ J/g}$  at 100% crystallization respectively (Liu, et al., 2020; Aumnate, et al., 2019).

$$X_c(\%) = \left[ \frac{\Delta H_m - \Delta H_{cc}}{\Delta H_m^0 \times W} \right] \times 100 \quad (15)$$

$$X_c(\%) = \left[ \frac{\Delta H_m}{\Delta H_m^0 \times W} \right] \times 100 \quad (16)$$

Where W is the weight fraction of PLA, LDPE, PP and PCL in the blends,  $\Delta H_m$  and  $\Delta H_m^0$  are the melting enthalpy and 100% crystalline melting enthalpy of PLA, LDPE, PP and PCL in the blends and  $\Delta H_{cc}$  is the cold crystallization enthalpy. LDPE, PP and PCL did not show cold crystallization peak, hence equation (16).

#### 4.4.3 Scanning Electron Microscopy (SEM)

The morphologies of the extruded filaments were investigated using a scanning electron microscope (Hitachi SU3500) with an accelerating voltage of 5kV. The test samples of extruded filaments were prepared by immersing filaments in liquid nitrogen for 3-5min and afterward the samples were fractured (cryogenic fracture). The fractured filaments were placed on the specimen stub and subsequently, coated by gold/palladium spraying. The specimen stub containing samples was placed in the specimen chamber and subjected to SEM imaging to characterize its morphology. Different magnifications of images of 1.5K were obtained from the experiment.

#### 4.4.4 Shape Memory test

To investigate the shape memory behaviour of the blends, thermomechanical tests were conducted manually. Extruded filaments of selected polymer blends were cut into equal length of 18cm and used as test samples. First, the samples were heated in an oven to a deformation temperature of 65°C and held for 10 mins. The initial strain,  $\varepsilon_p(N - 1)$  of the samples was recorded. Then the samples were stretched to a temporary strain,  $\varepsilon_m$  of 15%, 25% and 50% and held for about 3 mins. The samples were cooled to room temperature to fix the temporary shape and the programming strain applied was removed. The sample was kept for 5 mins and the new strain,  $\varepsilon_u$  was recorded. To recover the permanent shape, the sample was placed again in the oven set at the deformation temperature and held for 10-20 min. The original shape of the sample was recovered, and the final strain,  $\varepsilon_p(N - 1)$  was recorded. Finally, the shape fixity ( $R_f$ ) and the shape recovery ( $R_r$ ) were calculated using equations 8 and 9, respectively.

## 5. RESULTS AND DISCUSSION

### 5.1 Extrusion

Polymer blends of PLA/PCL/PEG-b-PCL, PLA/PEG, LDPE/PEG, PP/PEG, PLA/PBA were unsuccessful during extrusion and further processing was terminated. At higher temperatures, PEG or PBA present in blends exits the extruder nozzle as liquid, separating from the bulk polymer and producing heterogeneous filaments. PLA/PCL blended with PEG-b-PCL become slippery at high temperature making it difficult for the screw to exert a shear force between the polymer and the barrel wall in the extruder. Polymer blends of PP/PCL, PP/PCL/PP-g-ma, PLA/PCL, LDPE/PCL, LDPE/PCL/PE-g-ma produced homogeneous filaments during extrusion and were further processed. Polymer blends of PLA/PCL with PEG-PPG-PEG additive produced homogeneous filaments for 2.5-5 phr additive content and the homogeneity of the filaments began to decrease with increasing additive content.

### 5.2 Mechanical properties

The mechanical properties of PP/PCL, PP/PCL/PP-g-ma, PLA/PCL, PLA/PCL/PEG-PPG-PEG LDPE/PCL, LDPE/PCL/PE-g-ma were investigated by tensile tests and the results are reported as stress-strain curves in Figures 16-25 while Tables 11-15 show a summary of the mechanical properties of the polymer blends obtained from the stress-strain curves of each polymer blend and given as elastic modulus, tensile strength, and elongation at break. Due to variations, the plots are presented in two views (one zoomed view) to easily visualize the behaviour of the polymer samples at lower strains.

The stress-strain curve of PP100 presented in Fig. 16 and the result summary given in Table 11 shows its good elastic modulus, tensile strength, and elongation above 926% while PCL100 showed poor elastic modulus and tensile strength but good elongation above 926%. The tensile strength at break of PP100 and PCL100 were 38.3 MPa and 19.3 MPa, respectively. The addition of PCL changed the tensile behaviour of PP. While the elastic modulus and tensile strength decreased on addition of PCL, the elongation was maintained with 10 wt.% and 20 wt.% PCL but decreased to 549% with 30 wt.% PCL. The tensile strength and elastic modulus decreased with addition of PCL due to the lower tensile strength and elastic modulus of PCL as

compared to that of PP. A compatibilizer PP-g-ma varied between 1.25-10 phr was added to the PP/PCL blends to improve the miscibility and properties of the blend. PP-g-ma has been reported as a successful compatibilizer in polyolefin blends (Kahar, et al., 2012). Figures 17-19 and Table 12 shows the compatibilizer improved the elastic modulus and tensile strength of the PP/PCL blends when compared to the blends without compatibilizer, but clearly decreased their elongation properties. The blends with 1.25phr of PP-g-ma showed better tensile strength and elongation properties compared to blends with 5 and 10phr.

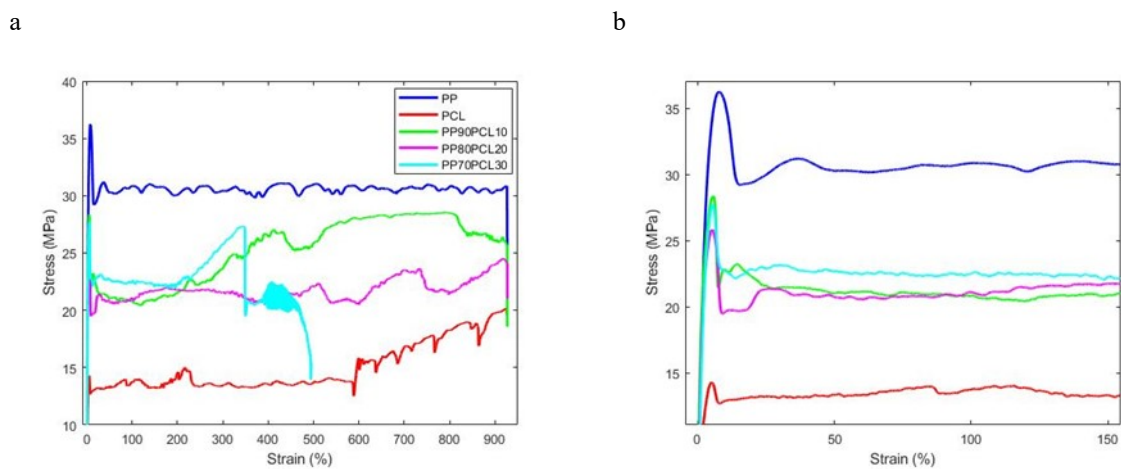


Figure 16. Stress strain curves of PP, PCL, and PP/PCL blends a) Full view b) Zoomed view.

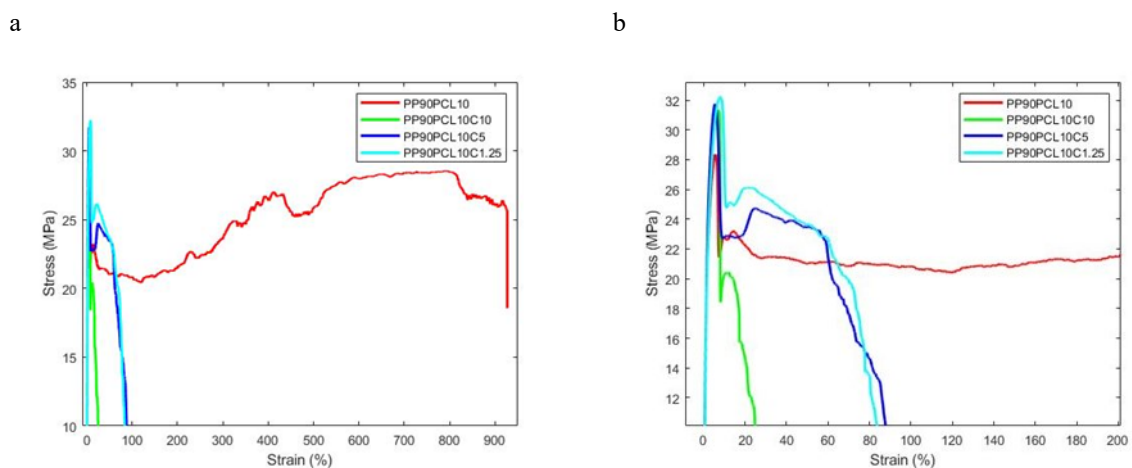


Figure 17. Stress strain curves of PP90/PCL10 and its compatibilized blends a) Full view b) Zoomed view.

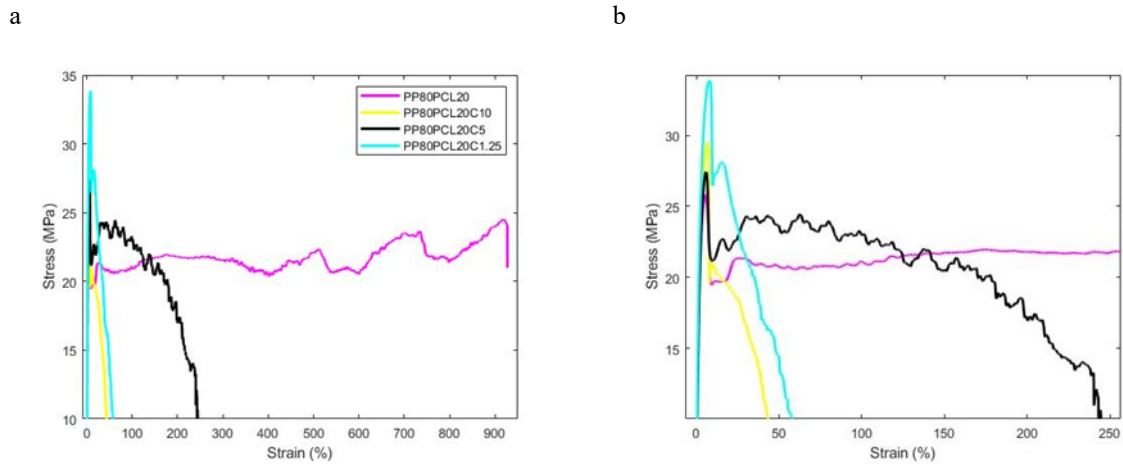


Figure 18. Stress strain curves of PP80/PCL20 and its compatibilized blends a) Full view b) Zoomed view.

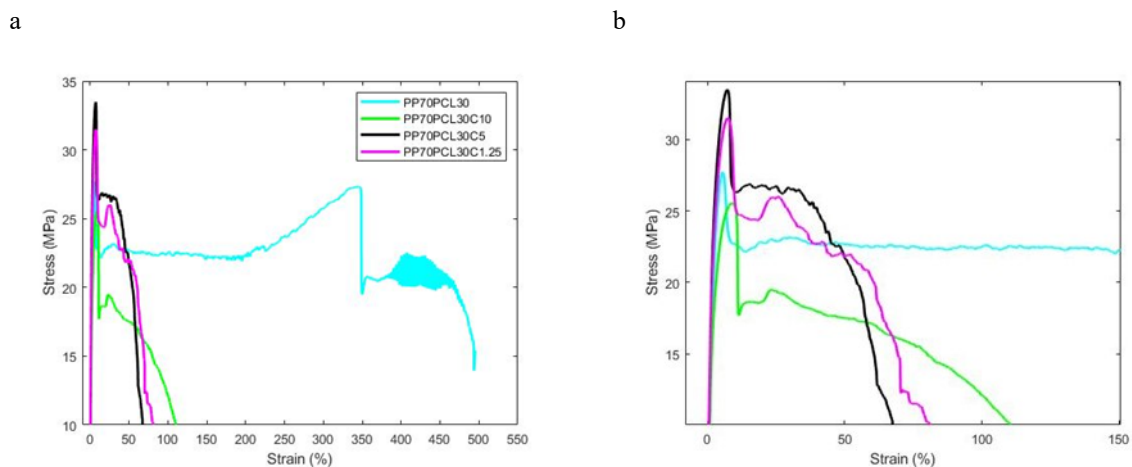


Figure 19. Stress strain curves of PP70/PCL30 and its compatibilized blends a) Full view b) Zoomed view.

Table 11. Mechanical properties of PCL, PP, and PP/PCL blends tested under room temperature.

Sample	Elastic Modulus MPa	Tensile Strength MPa	Elongation at break %
PP100	1866±350	38.3±2.31	926±1
PP90PCL10	1234±70	28.5±4.18	926±1
PP80PCL20	1117±80	25.4±1.30	926±1
PP70PCL30	890±80	27.6±6	549±247
PCL100	327.4±10	19.3±1.47	926±1

Table 12. Mechanical properties of compatibilized PP/PCL blends tested under room temperature.

Sample	Elastic Modulus MPa	Tensile Strength MPa	Elongation at break %
PP90PCL10C10	1233±90	30.2±1.50	32.7±26.3
PP90PCL10C5	1540±268	30.7±5.38	98.9±51.7
PP90PCL10C1.25	1356±77	32.2±1.1	104.3±32.4
PP80PCL20C10	1160±140	30.1±0.64	65.8±9.7
PP80PCL20C5	1457±106	30.7±5.66	178.8±158
PP80PCL20C1.25	1402±46	33.5±0.8	80.3±12.5
PP70PCL30C10	1152±140	27.7±3.76	134±46.4
PP70PCL30C5	1424±173	31.4±3.58	69.3±15.7
PP70PCL30C1.25	1307±52	32.0±1.38	116.8±36.3

The stress-strain curves of PLA100 illustrated in Figure 20 and the result summary given in Table 13 shows its good elastic modulus and tensile strength but very poor elongation property (8.62%) while that of PCL100 shows poor elastic modulus and tensile strength but good elongation above 926%. The tensile strength at break of PLA100 and PCL100 were 58.4 MPa and 19.3 MPa, respectively. PLA is very strong but brittle and its low elongation property is one of the main drawbacks in its applications. The addition of 10-60 wt.% PCL changed the tensile behaviour of PLA. The elastic modulus and tensile strength decreased with increasing PCL content showing the plasticizing effect of PCL on PLA as also reported in Navarro-Baena, et al. (2016). The tensile strength and elastic modulus decreased with increasing PCL content due to the lower tensile strength and elastic modulus of PCL as compared to that of PLA. The elongation property of the blend increased with increasing PCL content indicating the contribution of PCL in decreasing the brittle behaviour of PLA. This was similarly reported in Ferri, et al. (2016) and attributed to the plasticization effect of PCL on PLA/PCL matrix.

An additive PEG-PPG-PEG varied between 2.5-10phr was added to 80PLA/20PCL, 70PLA/30PCL and 60PLA/40PCL blends to further improve their elongation property. The plasticisation effect of PEG-PPG-PEG on PLA/PCL blends was reported in Wachirahuttapong, et al. (2016). Figures 21-23 and Table 14 shows the additive improved the elongation properties of the blend but decreased their elastic modulus and tensile strength. This was not the case for

80PLA/20PCL5 which showed a slight increase in modulus and tensile strength when compared with 80PLA/20PCL. Percentage increase of 102.1% and 321.7% was observed for 70PLA/30PCL and 60PLA/40PCL with 5phr of PEG-PPG-PEG and was lower with higher additive content. 80PLA/20PCL blend with 2.5-10 wt.% PEG-PPG-PEG showed irregularity in elongation at break but a percentage increase of 205.6 % was observed for 80PLA/20PCL with 2.5phr of PEG-PPG-PEG. The blends with lower additive content ( $\leq 5$ ) showed better elongation properties than blends with higher content, contrary to what was reported in Wachirahuttapong, et al. (2016) in which the elongation property of PLA/PCL blends increased with increasing PEG-PPG-PEG content. This could be due to improper mixing of the polymer blends and additive in the extruder due to size and temperature differences, resulting in the excess PEG-PPG-PEG settling and extruding as liquid, separately from the bulk polymer blend.

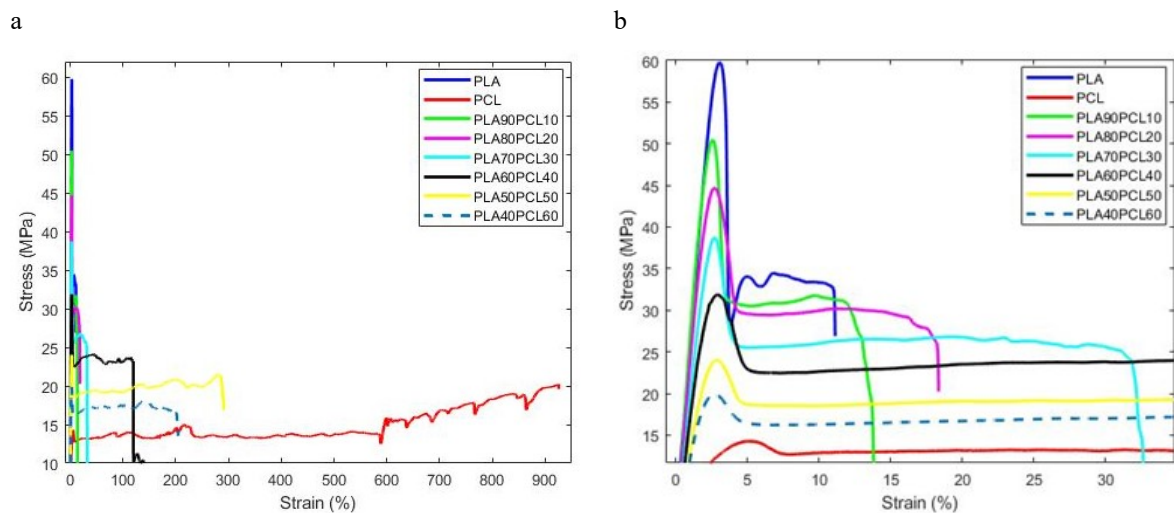


Figure 20. Stress strain curves of PLA, PCL, and PLA/PCL blends a) Full view b) Zoomed view.

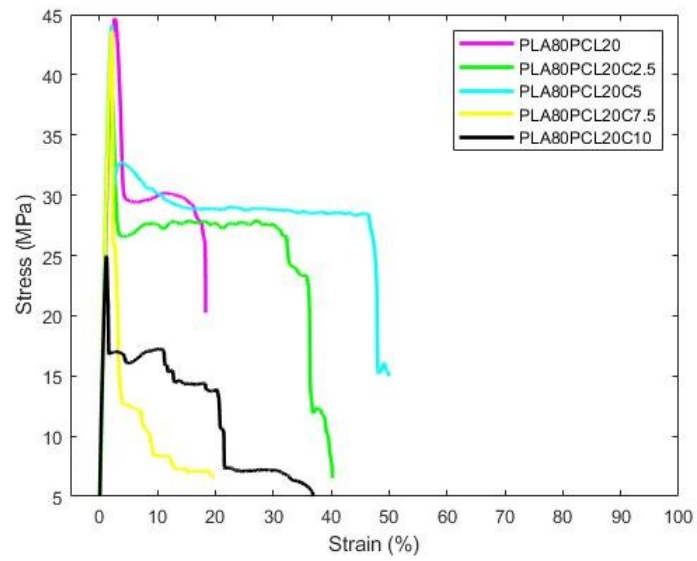


Figure 21. Stress strain curves of PLA80/PC20L and its compatibilized blends.

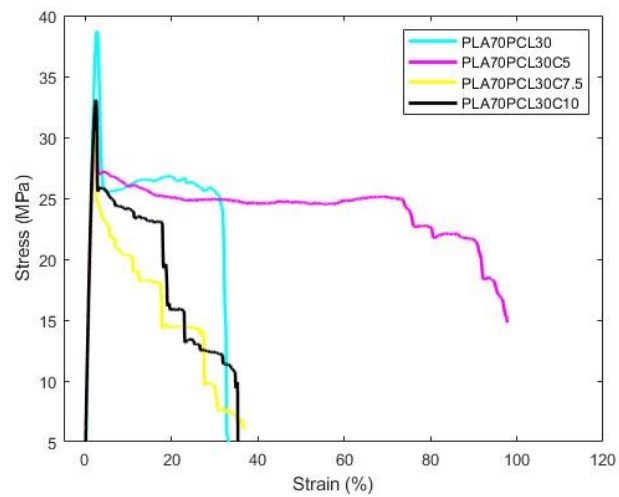


Figure 22. Stress strain curves of PLA70/30PCL and its compatibilized blends.

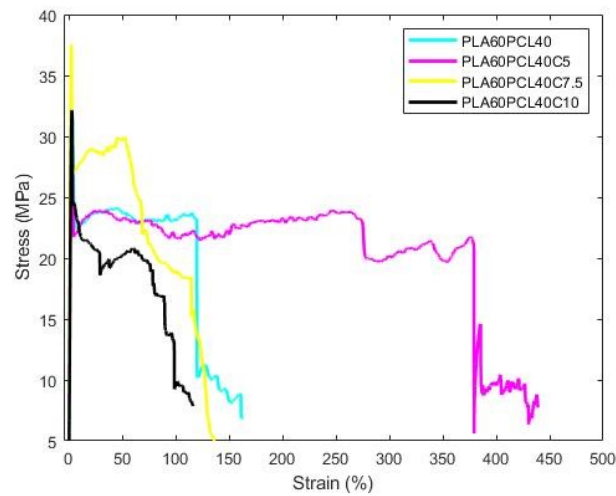


Figure 23. Stress strain curves of PLA60/40PCL and its compatibilized blends.

Table 13. Mechanical properties of PCL, PLA, and PLA/PCL blends tested under room temperature.

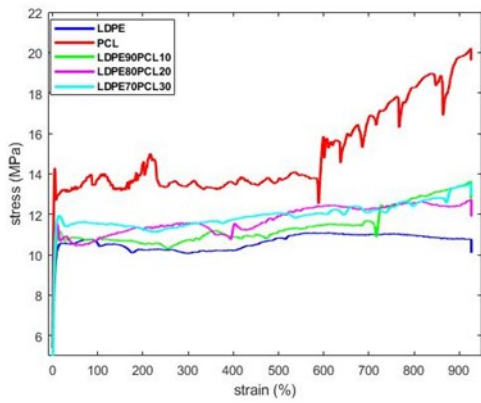
Sample	Elastic Modulus MPa	Tensile Strength MPa	Elongation at break %
PLA100	2883±220	58.4±4.25	8.62±3.88
PLA90PCL10	3087±440	52.8±9.30	13.2±2.01
PLA80PCL20	2628±76	44.5±0.97	17.9±7.5
PLA70PCL30	2252±73	37.8±4.68	53.5±0.28
PLA60PCL40	1989±510	32.8±5.70	127±99.20
PLA50PCL50	1604±276	25.2±3.49	225.2±78.70
PLA40PCL60	1254±184	20.1±1.16	260.8±103.67
PCL100	327.4±10	19.3±1.47	926±1

Table 14. Mechanical properties compatibilized PLA/PCL blends tested under room temperature.

Sample	Elastic Modulus MPa	Tensile Strength MPa	Elongation at break %
PLA80PCL20C2.5	2555±216	39.3±20.26	54.7±38.91
PLA80PCL20C5	2710±170	45.3±2.61	41.0±34.40
PLA80PCL20C7.5	2609±285	41.7±1.88	25.6±9.14
PLA80PCL20C10	2172±464	33.5±9.44	45.9±65.35
PLA70PCL30C5	1814±184	33.96±2.30	108.1±38.0
PLA70PCL30C7.5	2001±136	32.2±3.28	43.9±35.4
PLA70PCL30C10	2110±270	31.3±5.94	50.6±35.9
PLA60PCL40C5	1691±276	31.3±3.87	535.6±355.1
PLA60PCL40C7.5	1958±229	37.6±2.74	137.2±67.1
PLA60PCL40C10	1769±113	34.8±5.59	119.9±56.4

The stress-strain curves of LDPE100 presented in Fig. 24 and the result summary given in Table 15 shows its poor elastic modulus and tensile strength but good elongation property above 926%. The tensile strength at break of LDPE100 and PCL100 were 12.9 MPa and 19.3 MPa, respectively. The addition of PCL changed the tensile behaviour of LDPE. While the elastic modulus and tensile strength increased as the PCL content in blends increased, the elongation was maintained. When compared to LDPE100, LDPE90/PCL10 and LDPE80/PCL20 showed lower tensile strength and elastic modulus while LDPE70/PCL30 showed higher tensile strength and elastic modulus. The higher tensile strength and elastic modulus was due to more PCL content and higher tensile strength and elastic modulus of PCL compared to those of LDPE. A compatibilizer PE-g-ma (10 phr) was added to the LDPE/PCL blends to improve the miscibility and properties of the blend. PE-g-ma has been reported as a successful compatibilizer in polyolefin blends (Kahar, et al., 2012). Figure 25 and Table 15 shows that the compatibilizer slightly improved the elastic modulus and slightly decreased the tensile strength of the LDPE/PCL compatibilized blends when compared to the blends without compatibilizer. LDPE90/PCL10C and LDPE80/PCL20C showed good elongation property above 926% while the elongation of LDPE70/PCL30C significantly decreased to 488%. This could be due to compatibilization limitation.

a



b

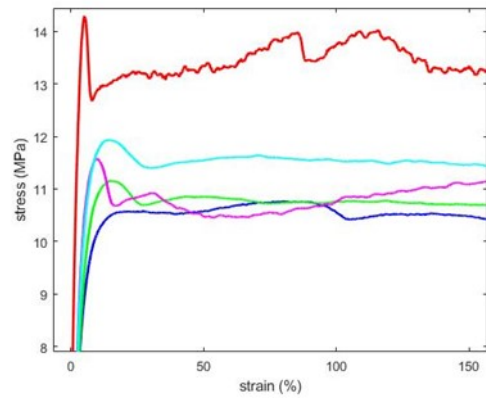
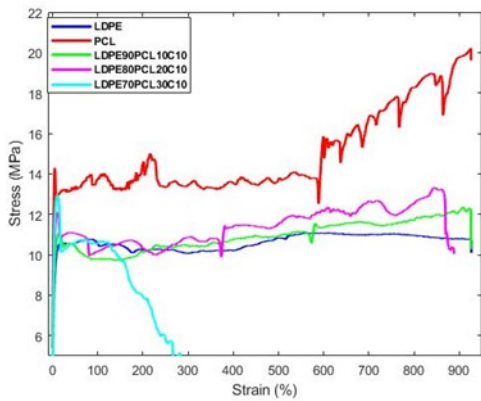


Figure 24. Stress strain curves of LDPE, PCL, and LDPE/PCL blends a) Full view b) Zoomed view.

a



b

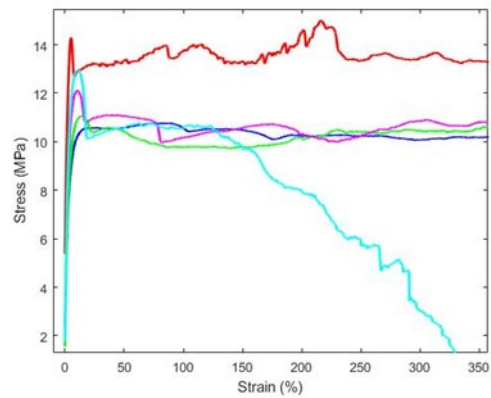


Figure 25. Stress strain curves of LDPE, PCL, and LDPE/PCL compatibilized blends a) Full view b) Zoomed view.

Table 15. Mechanical properties of PCL, LDPE, LDPE/PCL, and LDPE/PCL compatibilized blends tested under room temperature.

Sample	Elastic Modulus MPa	Tensile Strength MPa	Elongation at break %
LDPE100	289.5±50	12.9±1.69	926±1
LDPE90PCL10	250.1±20	11.6±2.07	926±1
LDPE80PCL20	284.3±40	12.7±1.06	926±1
LDPE70PCL30	340.6±70	12.8±1.35	926±1
LDPE90PCL10C	274.9±30	11.2±1.50	926±1
LDPE80PCL20C	295.7±20	12.1±1.08	926±1
LDPE70PCL30C	353.7±50	12.4±1.14	488±302
PCL100	327.4±10	19.3±1.47	926±1

Samples in most of the blends showed huge variations in their elongation properties (i.e., elongation property of each test sample), this could be due to improper mixing of the polymer pellets in the extruder screw due to their size differences.

### 5.3 Crystallization and melting behaviour

To study the crystallization and melting behaviour, blends with suitable mechanical properties were selected for further tests. The blends selected are given in Tables 16-18. The second heating scans and cooling scans of the selected blends are shown in Figures 26-30. The corresponding data obtained from DSC during investigation are summarized in Tables 16 -18.

Figure 26 and 27 shows comparative plots of DSC curves of PP/PCL and PP/PCL/PP-g-ma with varying PCL content while Table 16 summarizes the thermal parameters obtained from their DSC curves. For the blends without additive as shown in Figure 26 and Table 16, PP100 and PCL100 showed melting crystallization ( $T_{mc}$ ) peaks at 115.2°C and 32.3°C respectively and showed melting temperatures ( $T_m$ ) at 163.8°C and 58.6°C, respectively. Figure 26b shows that  $T_{m, PCL}$  did not clearly change with varying content of PCL and the value remained around 59°C while  $T_{mc, PCL}$  in Figure 26a slightly changed with varying PCL content, gradually decreasing from 35.4-34.3°C for 10-30 wt.% PCL content. When compared to the  $T_{mc, PCL}$  of PCL100, the values evidently changed. Figure 26b also shows that  $T_{m, PP}$  did not change with varying content of PCL and the values remained around 163.8°C while  $T_{mc, PP}$  slightly changed

for PP80PCL20. The non or very little changes in thermal transitions of PP and PCL in PP/PCL blends is an indication of weak interaction between both polymers.

As reported in Table 16, PP100 and PCL100 showed melt crystallization enthalpy ( $H_{mc}$ ) at  $82.6 \text{ Jg}^{-1}$  and  $57.3 \text{ Jg}^{-1}$  respectively and showed melting enthalpy ( $H_m$ ) at  $78.3 \text{ Jg}^{-1}$  and  $65.8 \text{ Jg}^{-1}$  respectively.  $H_{mc, PCL}$  and  $H_{m, PCL}$  of PP/PCL blends increased with increasing PCL content while  $H_{mc, PP}$  and  $H_{m, PP}$  decreased with increasing PCL content. The degree of crystallization ( $X_c$ ) of the PP and PCL and those in blends were calculated using equation 16.  $X_{c, PP}$  and  $X_{c, PCL}$  were calculated as 38.21% and 48.38% for PP100 and PCL100, respectively indicating that PP and PCL shows good crystallisation behaviour.  $X_{c, PCL}$  of blends when compared to that of PCL100 obviously reduced.  $X_{c, PCL}$  of PP90PCL10 was 15.4% and 27.6% for PP70PCL30, indicating that the crystallization of PCL in blends was inhibited at low PCL contents.  $X_{c, PP}$  of blends when compared to that of PP100 apparently increased indicating that PCL further improved the crystallization behaviour of PP.  $X_{c, PP}$  was highest for PP80PCL20 and slightly lower for PP90PCL10 and PP70PCL30, indicating that the crystallization of PP is slightly improved by adding 20 wt.% PCL.

For the blends with compatibilizer as shown in Figure 27 and Table 16,  $T_{mc, PCL}$  (Figure 27a) and  $T_m, PCL$  (Figure 27b) did not significantly change with varying content of PCL and their values remained around  $32^\circ\text{C}$  and  $59^\circ\text{C}$  respectively. Figure 27b also shows that  $T_m, PP$  clearly changed for PP80PCL20C1.25 and PP70PCL30C1.25 from  $163.8^\circ\text{C}$  of PLA100 to around  $166^\circ\text{C}$  for both blends.  $T_{mc, PP}$  slightly changed for PP80PCL20C1.25 and PP70PCL30C1.25. The little changes in thermal transitions of PP and PCL in PP/PCL/PP-g-ma blends is an indication of more interfacial interaction between both polymers and possibly improved miscibility.

As reported in Table 16,  $H_{mc, PCL}$  and  $H_{m, PCL}$  of PP/PCL/PP-g-ma blends increased with increasing PCL content while  $H_{mc, PP}$  and  $H_{m, PP}$  decreased with increasing PCL content. Addition the compatibilizer obviously enhanced the crystallisation behaviour of PCL in the blends when compared to that of blends without compatibilizer.  $X_{c, PP}$  of blends with compatibilizer when compared to that of blends without compatibilizer decreased. Like the non-compatibilized PP/PCL blends,  $X_{c, PP}$  was highest for PP80PCL20C1.25 and slightly lower for PP90PCL10 and PP70PCL30, indicating that the crystallization of PP is slightly improved by adding 20 wt.% PCL.

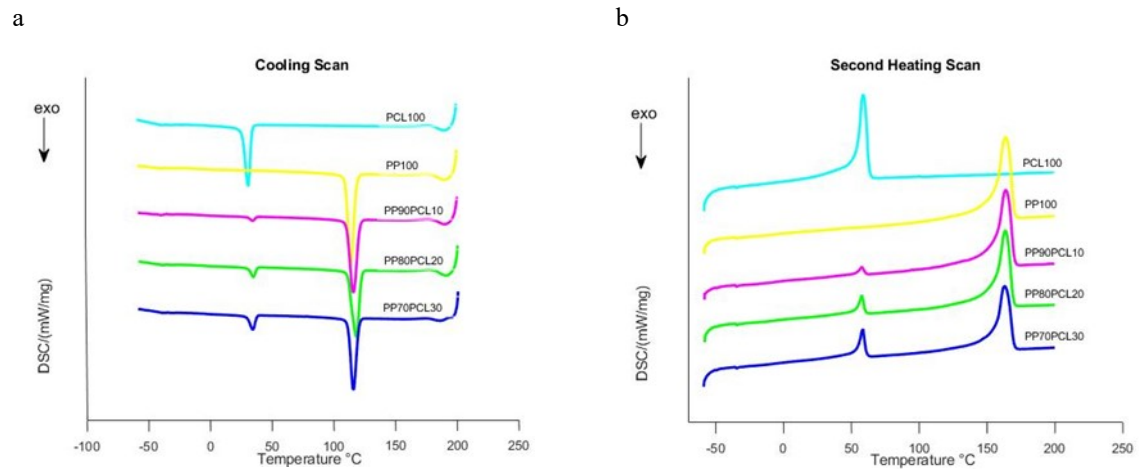


Figure 26. DSC analysis of PP, PCL, and PP/PCL blends: a) Cooling scans and b) Second heating scans.

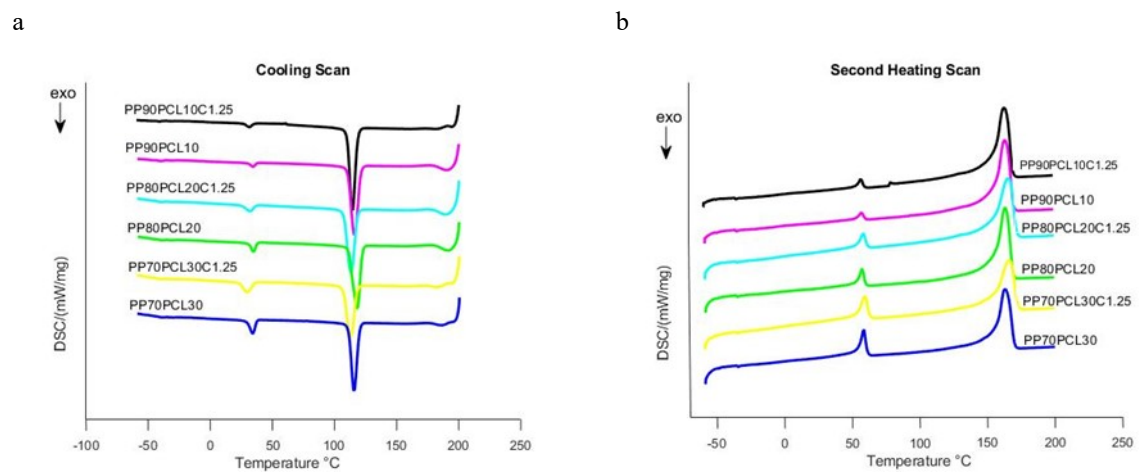


Figure 27. DSC analysis of PP/PCL blends and compatibilized PP/PCL blends: a) Cooling scans and b) Second heating scans.

Table 16. Thermal parameters of PCL, PP, PP/PCL blends and compatibilized PP/PCL blends obtained from the DSC scans.

Sample	PCL					PP				
	T <sub>m</sub> (°C)	T <sub>mc</sub> (°C)	H <sub>m</sub> (Jg <sup>-1</sup> )	H <sub>mc</sub> (Jg <sup>-1</sup> )	X <sub>c</sub> (%)	T <sub>m</sub> (°C)	T <sub>mc</sub> (°C)	H <sub>m</sub> (Jg <sup>-1</sup> )	H <sub>mc</sub> (Jg <sup>-1</sup> )	X <sub>c</sub> (%)
PP100	-	-	-	-	-	163.80	115.20	78.33	82.59	38.21
PP90PCL10	57.57	35.35	2.09	2.93	15.35	163.70	116.30	72.02	76.53	39.04
PP80PCL20	57.67	35.31	6.40	7.11	23.51	163.80	118.20	68.69	71.93	41.88
PP70PCL30	58.59	34.34	11.27	11.42	27.62	162.70	115.30	57.37	61.88	39.98
PP90PCL10C1.25	57.51	31.45	2.79	3.18	20.50	163.60	115.40	70.95	75.29	38.46
PP80PCL20C1.25	58.67	32.31	5.74	6.37	21.11	165.80	114.20	66.08	71.65	40.29
PP70PCL30C1.25	59.63	30.34	11.39	12.65	27.92	165.70	113.30	55.52	59.95	38.69
PCL100	58.64	32.33	65.80	57.31	48.38	-	-	-	-	-

Figure 28 and 29 shows comparative plots of DSC curves of PLA/PCL and PLA/PCL/ PEG-PPG-PEG respectively with varying PCL content while Table 17 summarizes the thermal parameters obtained from their DSC curves. For the blends without additive as shown in Figure 28 and Table 17, PLA100 and PCL100 showed melting temperatures (T<sub>m</sub>) at 153.6°C and 58.6°C respectively. PLA100 showed cold crystallization (T<sub>cc</sub>) peaks at 111.5°C while PCL100 showed melt crystallisation (T<sub>mc</sub>) peak at 32.3°C. Figure 28a shows that T<sub>mc, PCL</sub> did not obviously change with varying content of PCL and the value remained around 33°C. Both PLA100 and PLA in blends did not show melt crystallisation peaks and this was attributed to the slow crystallisation rate of PLA (Liu, et al., 2020). T<sub>m, PLA</sub> (Figure 28b) did not show apparent changes with addition of PCL and the temperature values were maintained around 154°C while T<sub>m, PCL</sub> also did not significantly change with varying content of PCL and the value remained around 59°C. It also shows that T<sub>cc, PLA</sub> slightly changed and increased with increasing PCL content, from 111.5°C for PLA100 to a range of 115.7-118.6°C for 10-30 wt.% PCL. These non or very little changes in thermal transitions of PLA and PCL in their blends is an indication of weak or lack of interaction between both polymers signifying poor miscibility. The T<sub>g</sub> value of PLA could be observed in Figure 28b from PLA100 and PLA90PCL10 DSC curves but could not be observed for other blends with higher PCL content due to overlap with T<sub>m</sub> of PCL.

As reported in Table 17, PLA100 showed cold crystallization ( $H_{mc}$ ) enthalpy at  $26.55 \text{ Jg}^{-1}$  and PCL100 showed melt crystallization enthalpy ( $H_{mc}$ ) at  $57.3 \text{ Jg}^{-1}$ . PLA00 and PCL100 showed melting enthalpy ( $H_m$ ) at  $25.91 \text{ Jg}^{-1}$  and  $65.8 \text{ Jg}^{-1}$  respectively.  $H_{mc, PCL}$  and  $H_{m, PCL}$  of PLA/PCL blends increased with increasing PCL content (20-40 wt.%) while  $H_{cc, PLA}$  and  $H_{m, PLA}$  decreased with increasing PCL content. The degree of crystallization ( $X_c$ ) of the PLA and PCL and those in blends were calculated using equations 15 and 16.  $X_{c, PLA}$  and  $X_{c, PCL}$  were calculated as 0% and 48.38% for PP100 and PCL100, respectively indicating that PCL shows good crystallisation behaviour while PLA does not crystallise.  $X_{c, PLA}$  gradually but not so evidently, increased with increasing PCL content indicating that the crystallisation of PLA is enhanced by PCL content.  $X_{c, PCL}$  of PLA80PCL20 was calculated as 15% and that of PLA60PCL40 was calculated as 33.2% which is almost close to that of PCL100. These values of  $X_{c, PCL}$  suggest that PCL has good crystallisation ability which can be hindered at low PCL contents.

For the blends with additive (PEG-PPG-PEG) as shown in Figure 29 and Table 17,  $T_{mc, PCL}$  (Figure 29a) did not significantly change with varying content of PCL and addition of PEG-PPG-PEG and the value remained around  $33^\circ\text{C}$  while  $T_{cc, PLA}$  clearly changed.  $T_{m, PCL}$  (Figure 29b) also did not show apparent changes with varying content of PCL and added PEG-PPG-PEG and the value remained at around  $59^\circ\text{C}$ . However,  $T_{m, PLA}$  evidently changed with addition of PEG-PPG-PEG to the PLA/PCL blend and showed two melting behaviours. The change in  $T_m$  could be due to good interaction between both polymers while the double melting behaviour could be due to different crystal structures formed in which the lower melting temperature corresponds to the  $\beta$ -crystals and the higher melting temperature corresponding to the  $\alpha$ -crystals (Chavalitpanya & Phattanarudee, 2013).

As reported in Table 17,  $H_{mc, PCL}$  and  $H_{m, PCL}$  of PLA/PCL/PEG-PPG-PEG blends increased with increasing PCL content (20-40 wt.%) and as well increased when compared to blends without additive.  $H_{cc, PLA}$  and  $H_{m, PLA}$  decreased with increasing PCL content. Addition of PEG-PPG-PEG clearly enhanced the crystallisation behaviour of PLA and PCL in the blends.  $X_{c, PLA}$  increased with increasing PCL content indicating that the crystallisation of PLA is enhanced by PCL content.  $X_{c, PCL}$  of PLA80PCL20C2.5 was calculated as 27.9% and that of PLA60PCL40C5 was calculated as 45.7% which is almost close to that of PCL100. These values of  $X_{c, PCL}$  also suggest that PCL has good crystallisation ability which can be hindered at low PCL contents.

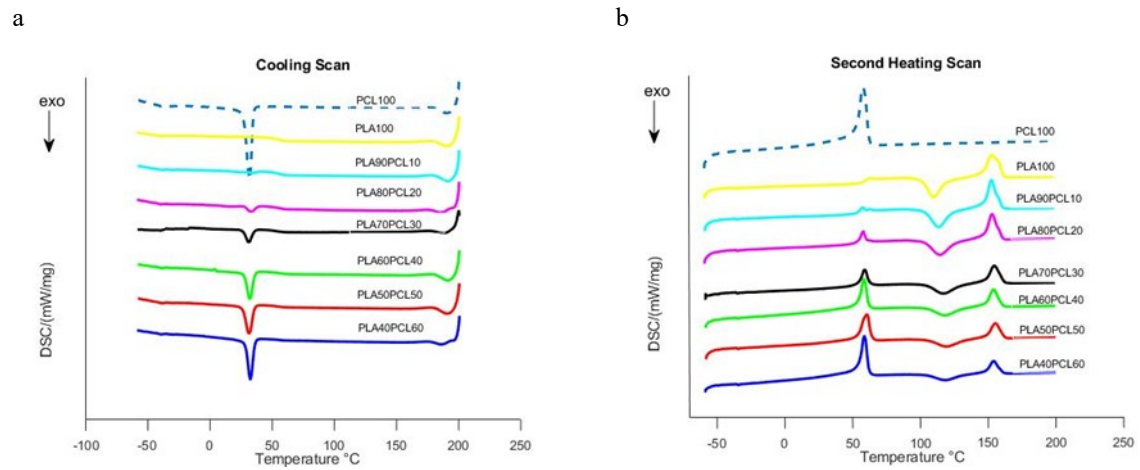


Figure 28. DSC analysis of PLA, PCL, and PLA/PCL blends: a) Cooling scans and b) Second heating scans.

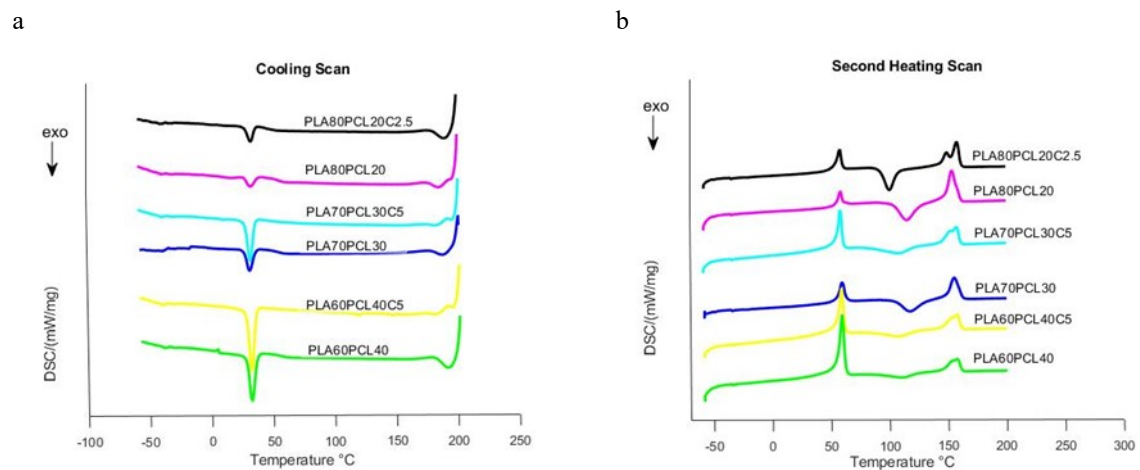


Figure 29. DSC analysis of PLA/PCL blends and compatibilized PLA/PCL blends: a) Cooling scans and b) Second heating scans.

Table 17 Thermal parameters of PCL, PLA, PLA/PCL blends and compatibilized PLA/PCL blends obtained from the DSC scans.

Sample	PCL					PLA					
	T <sub>m</sub> (°C)	T <sub>mc</sub> (°C)	H <sub>m</sub> (Jg <sup>-1</sup> )	H <sub>mc</sub> (Jg <sup>-1</sup> )	X <sub>c</sub> (%)	T <sub>g</sub> (°C)	T <sub>m</sub> (°C)	T <sub>cc</sub> (°C)	H <sub>m</sub> (Jg <sup>-1</sup> )	H <sub>cc</sub> (Jg <sup>-1</sup> )	X <sub>c</sub> (%)
PLA100	-	-	-	-	-	60	153.60	111.5	25.91	26.55	-0.68
PLA80PCL20	58.68	33.32	4.10	4.69	15.07	-	153.80	115.7	22.85	23.22	-0.49
PLA70PCL30	59.63	31.34	8.67	9.65	21.26	-	154.70	117.7	16.64	16.89	-0.38
PLA60PCL40	58.58	32.33	18.06	20.65	33.20	-	154.70	118.6	14.28	13.85	0.77
PLA80PCL20C2.5	58.64	34.31	7.60	6.02	27.93	-	149.70/157.70	100.6	21.85	20.04	2.42
PLA70PCL30C5	57.59	32.35	16.03	16.37	39.29	-	151.70/156.70	107.6	15.82	10.15	8.65
PLA60PCL40C5	58.65	32.35	24.84	24.69	45.66	-	150.70/156.70	102.7	11.46	4.34	12.68
PCL100	58.64	32.33	65.80	57.31	48.38	-	-	-	-	-	-

Figure 30 shows comparative plots of DSC curves of LDPE/PCL and LDPE/PCL/PE-g-ma with varying PCL content while Table 18 summarizes the thermal parameters obtained from their DSC curves. For the blends without additive as shown in Figure 30 and Table 18, LDPE100 and PCL100 showed T<sub>mc</sub> peaks at 107.2°C and 32.3°C respectively and showed T<sub>m</sub> at 125.7°C and 58.6°C, respectively. Figure 30 a and b shows that T<sub>mc, PCL</sub> and T<sub>m, PCL</sub> did not show obvious changes with varying PCL content and the values remained at around 33 and 59°C respectively. It also shows that T<sub>mc, LDPE</sub> and T<sub>m, LDPE</sub> did not evidently change with varying PCL content and the values remained at around 107 and 125°C respectively. These similar temperatures in thermal transitions of LDPE and PCL in LDPE/PCL blends indicate weak interaction between both polymers.

As reported in Table 18, LDPE100 and PCL100 showed H<sub>mc</sub> at 103.7 Jg<sup>-1</sup> and 57.3 Jg<sup>-1</sup> respectively and showed H<sub>m</sub> at 99.9 Jg<sup>-1</sup> and 65.8 Jg<sup>-1</sup> respectively. H<sub>mc, PCL</sub> and H<sub>m, PCL</sub> of LDPE/PCL blends increased with increasing PCL content while H<sub>mc, LDPE</sub> and H<sub>m, LDPE</sub> decreased with increasing PCL content. The degree of crystallization (X<sub>c</sub>) of the LDPE and PCL and those in blends were calculated using equation 16. X<sub>c, LDPE</sub> and X<sub>c, PCL</sub> were calculated as 34.1% and 48.38% for LDPE100 and PCL100, respectively indicating that PP and PCL shows good crystallisation behaviour. X<sub>c, PCL</sub> of blends when compared to that of PCL100 reduced. X<sub>c, LDPE</sub> increased for only LDPE90PCL10 and LDPE70PCL30 blends.

For the blends with PE-g-ma compatibilizer as shown in Figure 30 and Table 18,  $T_{m, PCL}$  (Figure 30b) did not show significant changes with varying content of PCL and addition of compatibilizer, and the value remained around  $59^{\circ}\text{C}$  while  $T_{mc, PCL}$  (Figure 30a) slightly changed with varying PCL content and addition of compatibilizer.  $T_{mc, PCL}$  slightly decreased from  $30.5$  to  $26.33^{\circ}\text{C}$  with increasing PCL content (10-30 wt.%) which could mean more interaction between both polymers and possible improved miscibility. Figure 30a and b also shows that  $T_{mc, LDPE}$  and  $T_{m, LDPE}$  did not change with varying PCL content and addition of compatibilizer.

As reported in Table 18,  $H_{mc, PCL}$  and  $H_m, PCL$  of LDPE/PCL/PE-g-ma blends increased with increasing PCL content while  $H_{mc, PP}$  and  $H_m, PP$  decreased with increasing PCL content. Addition of the compatibilizer apparently enhanced the crystallisation behaviour of LDPE90PCL10C blend when compared to that of blends without compatibilizer while crystallisation behaviour of other blends reduced.  $X_{c, LDPE}$  of blends with compatibilizer when compared to that of blends without compatibilizer decreased.

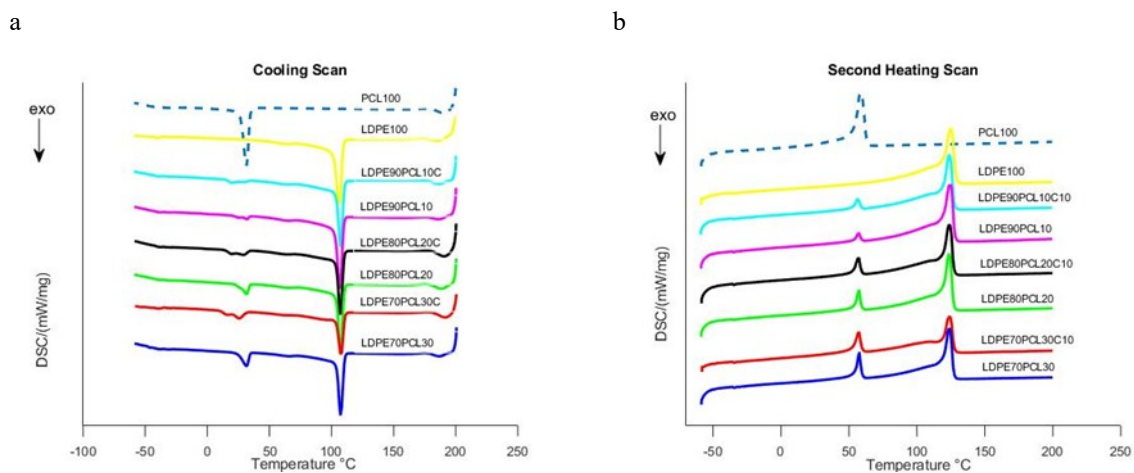


Figure 30. DSC analysis of LDPE, PCL, LDPE/PCL blends and compatibilized LDPE/PCL blends: a) Cooling scans and b) Second heating scans.

Table 18. Thermal parameters of PCL and LDPE in blends obtained from the DSC scans.

Sample	T <sub>m</sub> (°C)	T <sub>mc</sub> (°C)	H <sub>m</sub> (Jg <sup>-1</sup> )	H <sub>mc</sub> (Jg <sup>-1</sup> )	X <sub>c</sub> (%)	T <sub>m</sub> (°C)	T <sub>mc</sub> (°C)	H <sub>m</sub> (Jg <sup>-1</sup> )	H <sub>mc</sub> (Jg <sup>-1</sup> )	X <sub>c</sub> (%)
LDPE100	-	-	-	-	-	125.70	107.20	99.85	103.70	34.08
LDPE90PCL10	57.55	32.38	3.04	2.86	22.37	124.60	107.30	93.41	95.23	35.42
LDPE80PCL20	57.40	31.31	8.56	9.73	31.47	123.80	107.40	78.43	85.59	33.46
LDPE70PCL30	57.67	31.32	11.06	13.08	27.11	123.70	107.20	71.18	77.21	34.71
LDPE90PCL10C	56.56	30.50	4.44	3.51	32.66	124.30	107.30	83.80	92.06	31.78
LDPE80PCL20C	57.59	29.32	8.01	8.35	29.46	124.20	107.30	75.62	87.13	32.26
LDPE70PCL30C	57.63	26.33	10.98	10.45	26.91	124.70	107.30	58.47	69.04	28.51
PCL100	58.64	32.33	65.80	57.31	48.38	-	-	-	-	-

#### 5.4 Morphology of the blends

The morphologies of PP/PCL with 10-30 wt.% PCL, PLA/PCL with 20-40 wt.% PCL, LDPE/PCL with 10-30 wt.% PCL and their corresponding blends with additive or compatibilized were investigated using SEM. Micrographs of PP/PCL blends with 10-30 wt.% PCL and their corresponding compatibilized blends are shown in Figures 31-33.

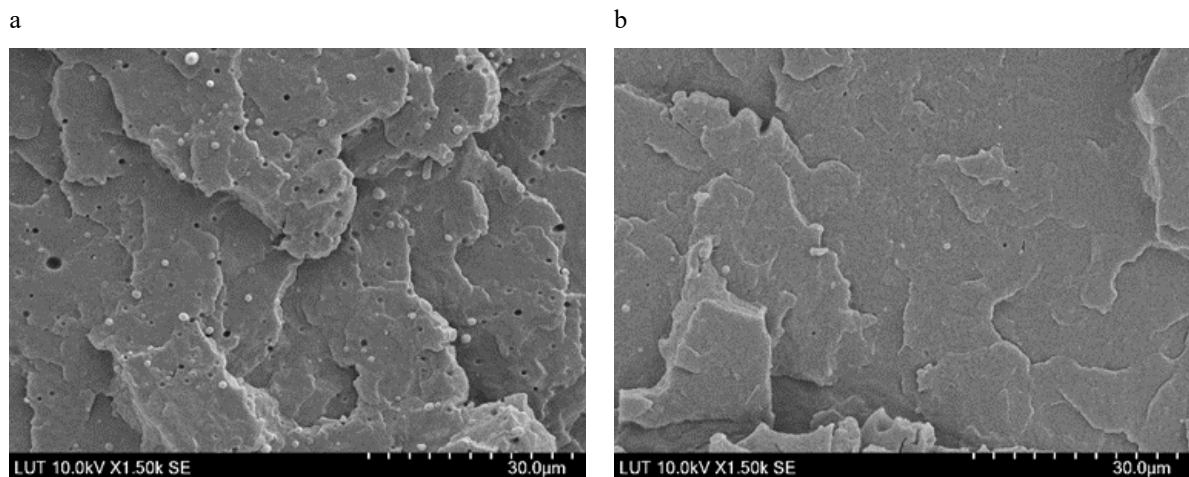


Figure 31. SEM images of a) PP90/PCL10, b) PP90/PCL10C1.25.

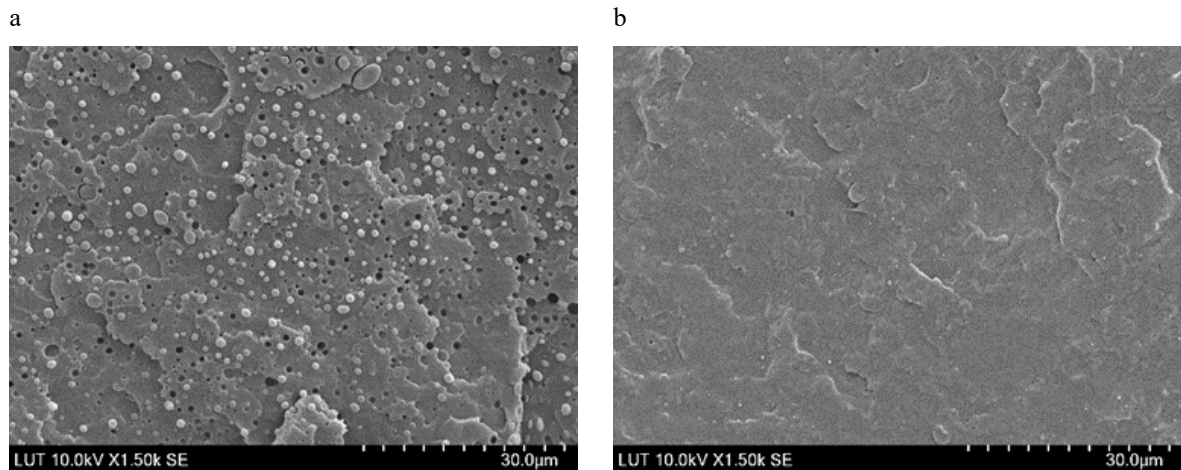


Figure 32. SEM images of a) PP80/PCL20, b) PP80/PCL20C1.25.

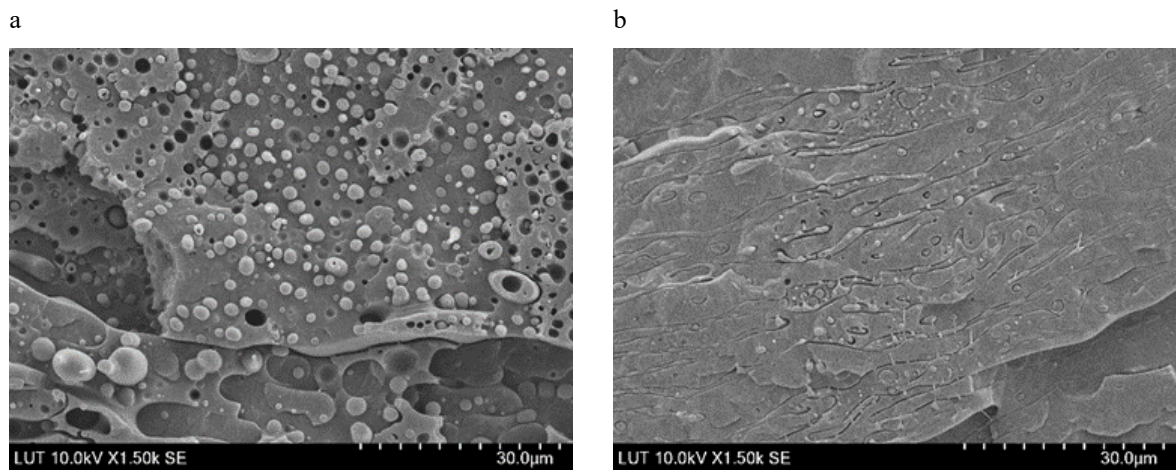


Figure 33. SEM images of a) PP70/PCL30, d) PP70/PCL30C1.25.

Figure 31a, 32a and 33a shows that PP/PCL blends exhibited a phase-separated morphology and are immiscible. The image showed spherical droplet of PCL and holes distributed in the PP matrix. The small spherical droplets and holes increased in size as PCL content in the blends increased. When PP-g-ma was added, at 1.25phr, into the PP/PCL blends, a nearly smooth structure with few tiny holes and spherical droplets of PCL were observed. Figure 31b and 32b shows the nearly smooth structure of compatibilized PP90/PCL10 and PP80/PCL20 blends. The number of holes and spherical droplets of PCL in PP80/PCL20C1.25 blend was a bit more compared to PP90/PCL10C1.25 blend due to higher PCL content. Figure 33b showed larger droplets and even fibrous forms of PCL also as a result on higher PCL content. This result suggests that the compatibilizer improved the interfacial adhesion and miscibility of both phases. Increasing the compatibilizer content will further increase the miscibility and adhesion in blends but investigations showed that the elongation properties will be highly reduced.

Micrographs of PLA/PCL blends with 20-40 wt.% PCL and their corresponding blends with additive are shown in Figures 34-36.

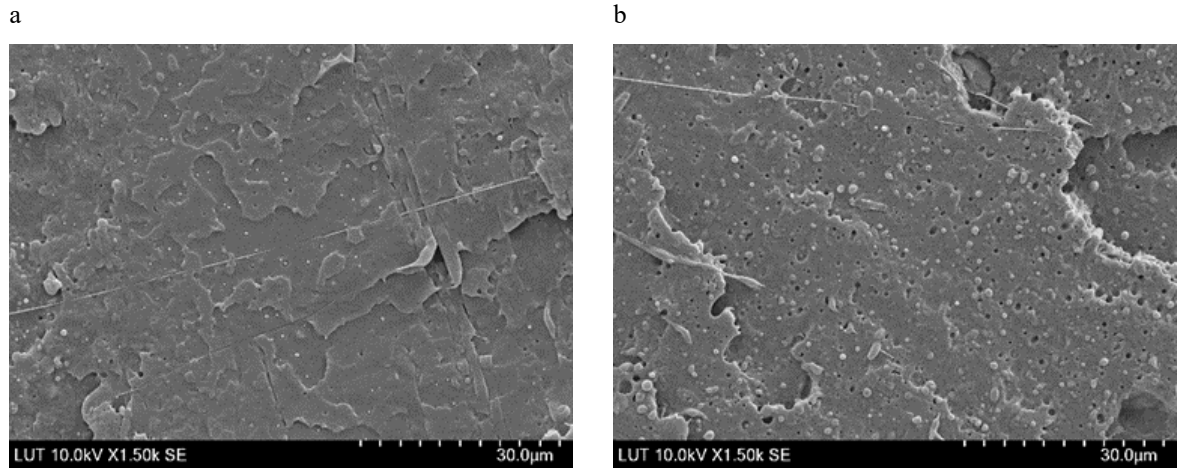


Figure 34. SEM images of a) PLA80/PCL20 b) PLA80/PCL20C2.5.

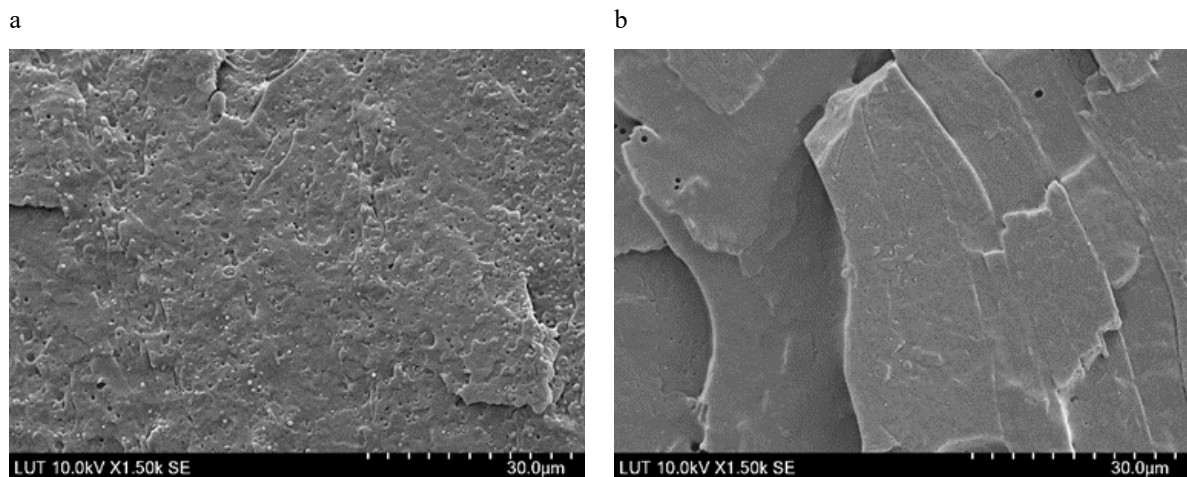


Figure 35. SEM images of a) PLA70/PCL30 b) PLA70/PCL30C5.

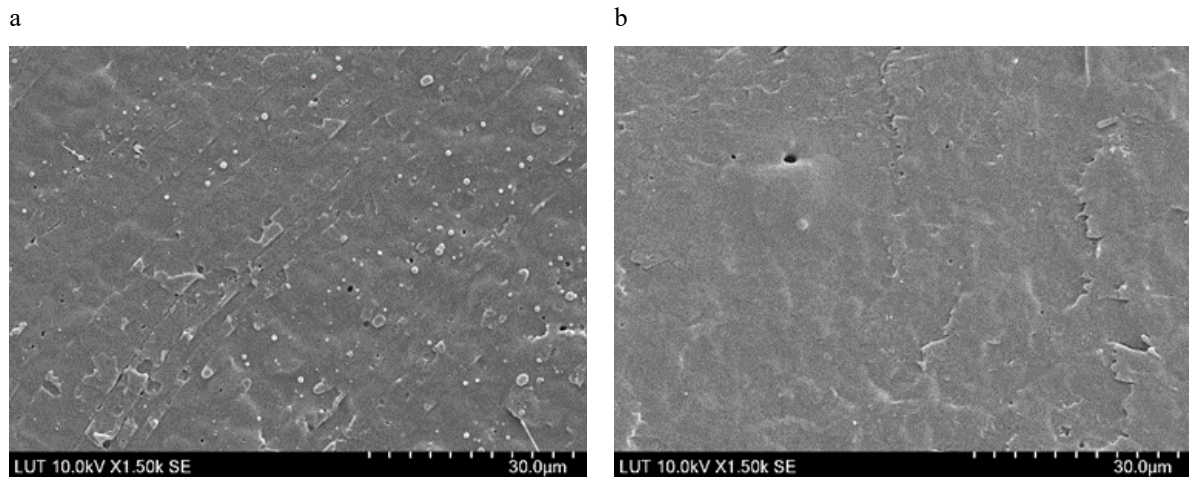


Figure 36. SEM images of a) PLA60/PCL40 b) PLA60/PCL40C5.

Figure 34a, 35a and 36a shows that PLA/PCL blends exhibited a phase-separated morphology which shows immiscibility in polymer blend. The images show spherical droplets of PCL and holes distributed in the sea-island structure of PLA matrix. The number of spherical droplets increased as PCL content increased from 20 wt.% to 30 wt.%. For the PLA60/PCL40 blend, PCL droplets changed to elongated form. The blend showed semi-continuous phase for each homopolymer with small number of spheres.

When PEG-PPG-PEG was added at 5phr into PLA70/PCL30 (Figure 35b) and PLA60/PCL40 blends (Figure 36b), a nearly smooth structure with few tiny holes and spherical droplets of PCL was observed indicating that the additive improved the surface adhesion and miscibility in these blends. This is however contrary to what was reported in Wachirahuttapong et al where the additive acted only as a plasticizer but did not improve miscibility (Wachirahuttapong, et al., 2016). The result was different when PEG-PPG-PEG was added at 2.5phr into PLA80/PCL20C blend. The micrograph (Figure 34b) showed more spherical droplets and larger droplets of PCL which could be due to the small concentration of the additive. To confirm this, PEG-PPG-PEG was added at 5phr into PLA80/PCL20 blend which showed less spherical droplets.

Micrographs of LDPE/PCL blends with 10-30 wt.% PCL and their corresponding compatibilized blends are shown in Figures 38-40.

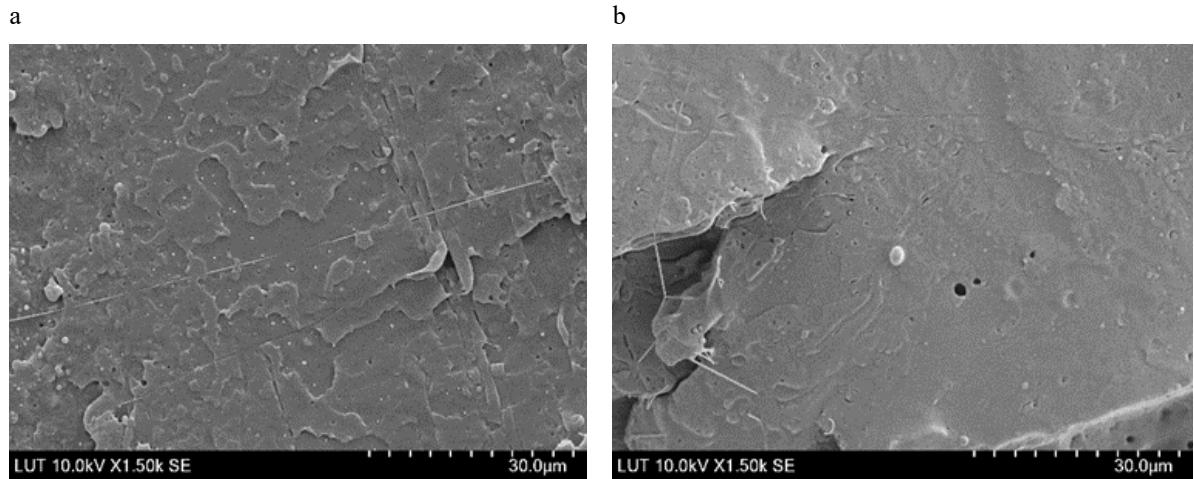


Figure 37. SEM images of a) PLA80/PCL20 b) PLA80/PCL20C5.

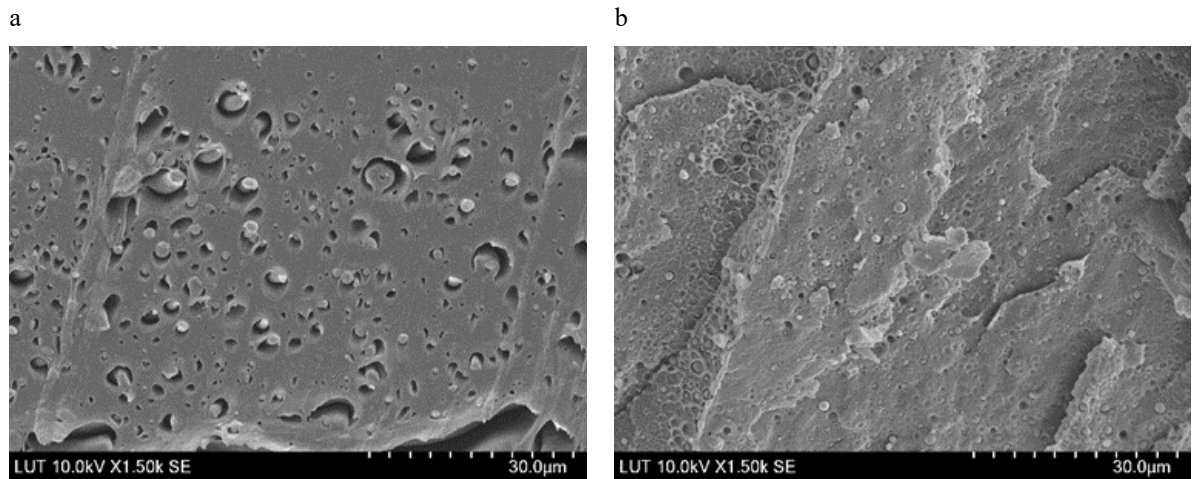


Figure 38. SEM images of a) LDPE90/PCL10, b) LDPE90/PCL10C

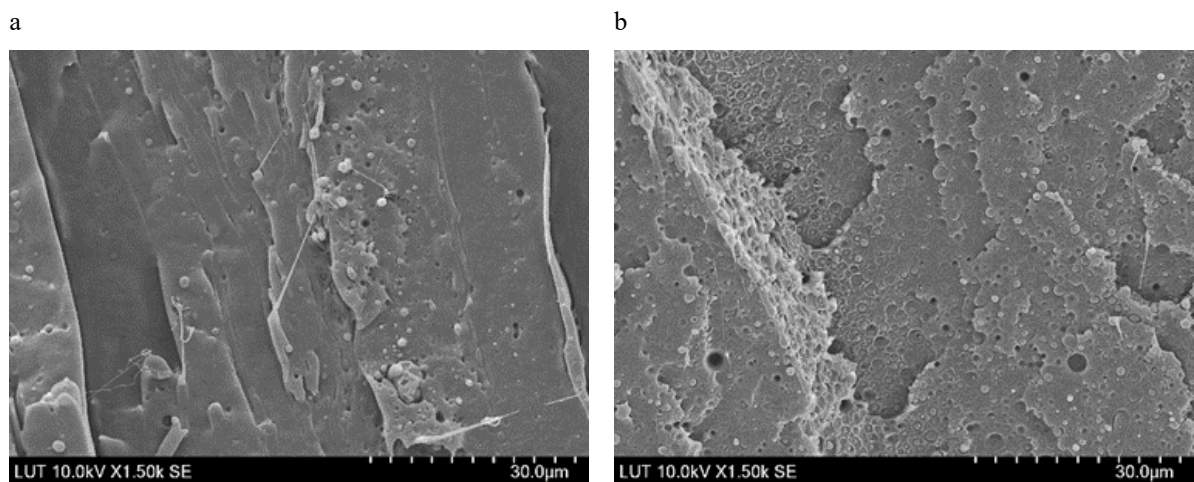


Figure 39. SEM images of a) LDPE80/PCL20, b) LDPE80/PCL20C.

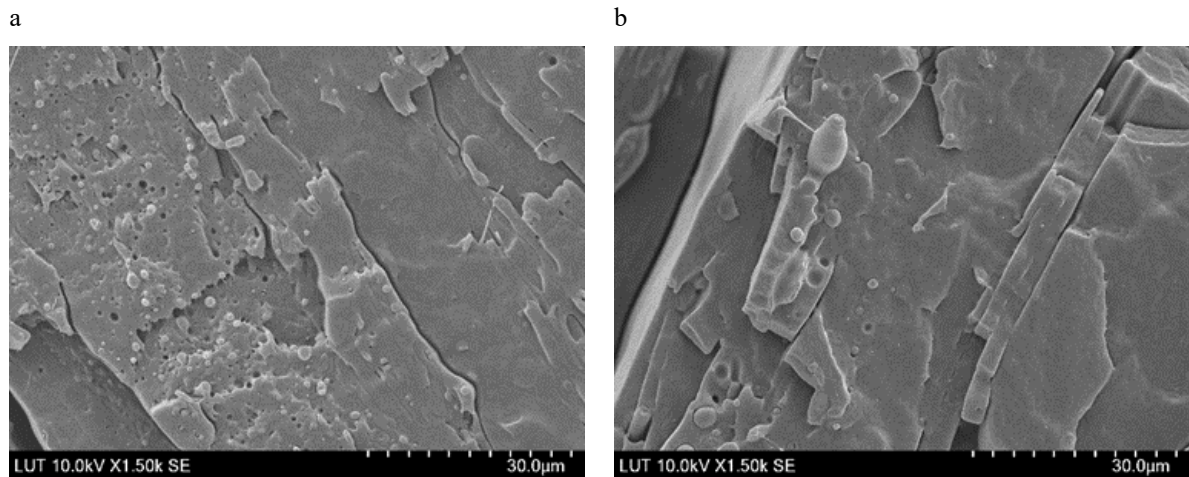


Figure 40. SEM images of a) LDPE70/PCL30, b) LDPE70/PCL30C.

Figure 38a shows fibrous forms of PCL and holes distributed in the LDPE matrix, Figure 39a fibrous forms and strings of PCL and holes distributed in the LDPE matrix and Figure 40a large droplets of PCL and holes distributed in the LDPE matrix. The PCL was not uniformly distributed in the LDPE matrix. This could be due to improper mixing of pellets in the extruder. These results confirm that LDPE/PCL blends exhibited a phase-separated morphology and are immiscible. When PE-g-ma was added, at 10phr, into the LDPE/PCL blends, micrographs in Figures 38b-40b show that fibrous PCL forms were reduced to spherical droplets and droplets to nearly smooth structures. LDPE90/PCL10C10 and LDPE80/PCL20C10 blends (Figure 38b and 39b) showed the fibrous PCL forms were reduced to spherical droplets while LDPE70/PCL30C10 (Figure 40b) showed a nearly smooth structure with traces of PCL spheres. This result suggests that the compatibilizer improved the interfacial adhesion and miscibility of both phases.

### 5.5 Filament testing

The LDPE/PCL blend was screened out in this process due to its poor tensile strength resulting in filament bending below the supplying roller even at very low printing speeds, causing difficulty in printing. PP/PCL could not stick well to the printing bed resulting in warping during printing. Successful printing was achieved using additional adhesion such as a double-sided polypropylene tape. 3D printing of PLA/PCL blends was successful without challenges.

Table 19. Printing parameters for filament testing.

Samples	Nozzle temperature (°C)	Bed temperature (°C)	Raster angle (°)	Infill density (%)	Printing speed (mm/min)
PLA/PCL	205	50	45	40	6000
PP/PCL	185	30	45	40	6000

### 5.6 Thermo-responsive shape memory behaviour and mechanism

Thermo-responsive shape memory behaviour was investigated on PP/PCL and PLA/PCL blends at different strains. Samples of PP/PCL and PLA/PCL blends were selected for shape memory test based on the results from tensile test, DSC, morphology, and 3D printing.  $R_f$  and  $R_r$  values calculated for PLA/PCL blends are given in Table 20. Several photographs were taken to provide a visual demonstration of the shape memory process and shown in Figures 41-45.

Table 20. Shape fixity and shape recovery values of investigated PLA/PCL blends.

Sample	Strain at 15%		Strain at 25%		Strain at 50%	
	$R_f$ (%)	$R_r$ (%)	$R_f$ (%)	$R_r$ (%)	$R_f$ (%)	$R_r$ (%)
PLA70PCL30	-	-	100	99.99	100	99.45
PLA60PCL40	-	-	99.56	99.99	100	98.88
PLA80PCL20C1.25	100	96.4	100	89.12	-	-
PLA70PCL30C1.25	-	-	100	80	100	72.22
PLA60PCL40C1.25	-	-	100	73.76	99.63	61.74

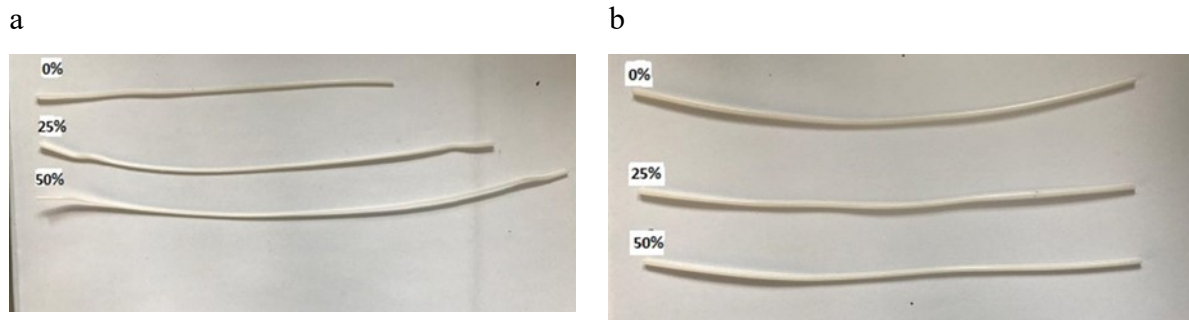


Figure 41. Thermomechanical cycle of PLA70PCL30 blend a) Fixing of temporary shape b) Recovery of permanent shape.

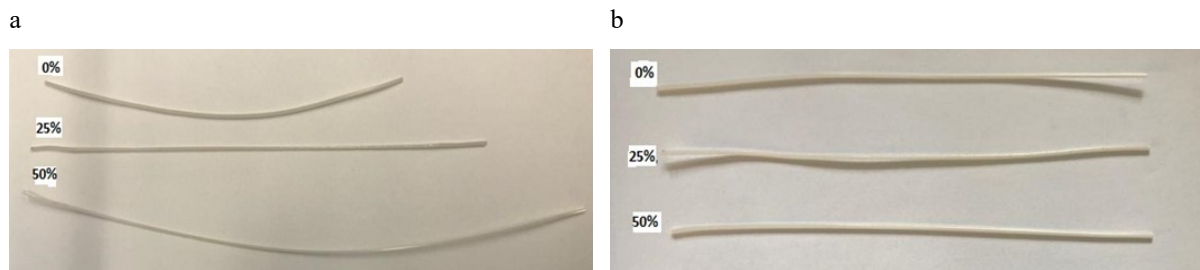


Figure 42. Thermomechanical cycle of PLA60PCL40 blend a) Fixing of temporary shape b) Recovery of permanent shape.

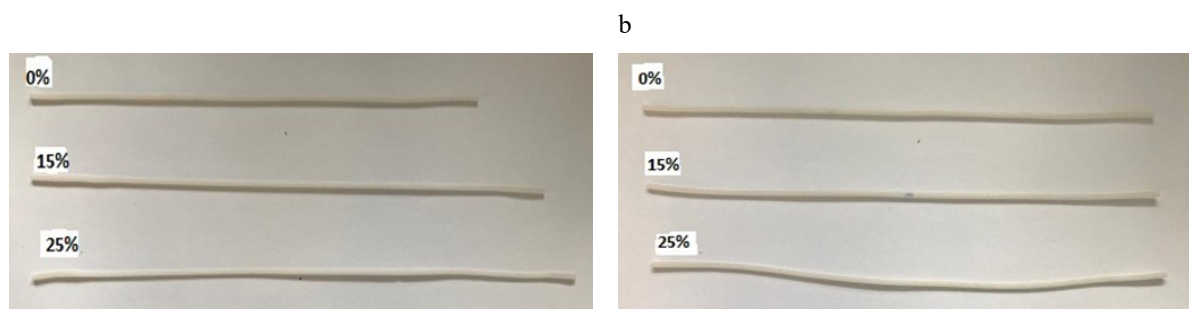


Figure 43. Thermomechanical cycle of PLA80PCL20C2.5 blend a) Fixing of temporary shape b) Recovery of permanent shape.

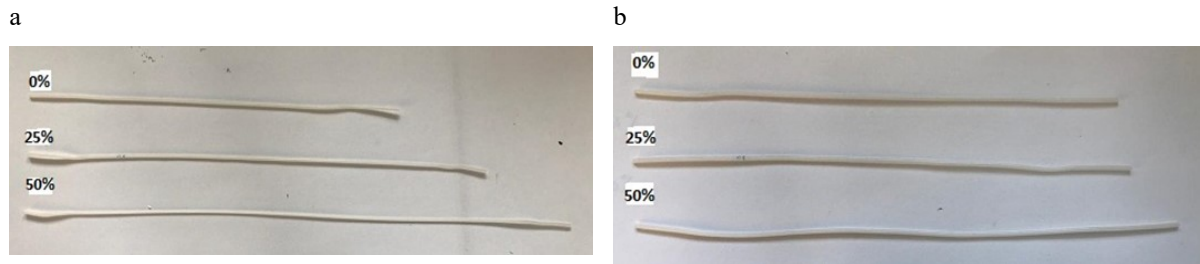


Figure 44. Thermomechanical cycle of PLA70PCL30C5 blend a) Fixing of temporary shape b) Recovery of permanent shape.

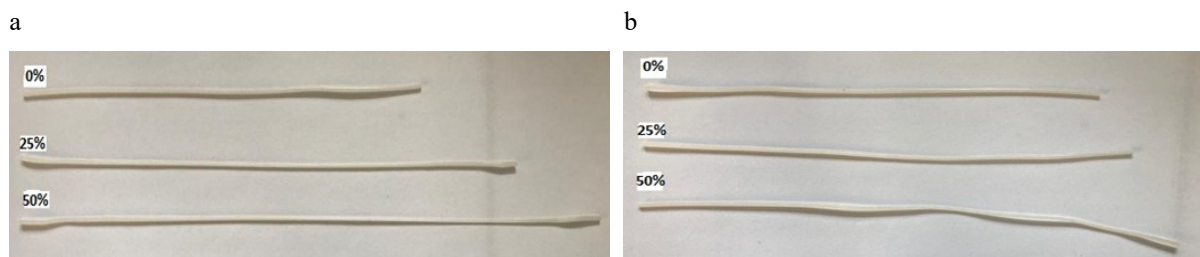


Figure 45. Thermomechanical cycle of PLA60PCL40C5 blend a) Fixing of temporary shape b) Recovery of permanent shape.

All the samples were heated, deformed, and cooled to a temporary shape. When the deformed samples were heated again, they recovered their permanent shape. Results presented in Table 20 and Figure 41-45 show that all the tested PLA/PCL blends and blends with additive demonstrated significant shape memory behaviour during the cycle. All the blends showed high  $R_f$  values (>98%). The blends without additive showed high  $R_r$  values (>97%) while the blends with additive showed lower  $R_r$  values between 61-96%. The  $R_r$  values decreased as the PCL content in blends increased from 30 to 40 wt.%. PLA70/PCL30 blend had the highest  $R_r$  values of about 99%. All samples were tested for 3 cycles and no significant change was observed. The effect of the temporary strain on  $R_f$  and  $R_r$  values were investigated. The blends were stretched at different strains considering their elongation properties. The results in Table 20 show that temporary strain had no significant effect on the  $R_f$  and  $R_r$  values of PLA/PCL without additive while  $R_f$  values for blends with additive reduced. Shape recovery speed was between 10-15 mins for the PLA/PCL without additive and 10-20mins for PLA/PCL blends with additive.

The melting behaviour, crystallisation behaviours and morphology of the blends were further studied to understand the shape memory mechanism. DSC results confirm that PCL phase which has a lower  $T_m$ , acted as the switching segment (soft segment) during shape memory cycle while the PLA phase acted as the net points (hard segment). When the samples were heated at a temperature lower than the  $T_m$  of PLA but a bit higher than that of PCL ( $T_d$ ), the PCL crystals in blends melted and their molecular chains switched to a temporary shape under applied strain. At this temperature, the molecular chain PLA which had a higher  $T_m$  were still frozen and acted as a fixed phase responsible for retaining the permanent shape. High  $R_f$  values of the blends can be attributed to the good crystallisation behaviour of PCL. During cooling, the molecular chains of PCL phase froze via rapid crystallization, requiring no external force to fix the temporary shape. As the PCL content in blends were increasing, DSC results showed that  $X_{c, PCL}$  was increasing as well, indicating that more PCL crystals partook in fixing the temporary shape.

Table 20 shows that  $R_f$  values decreased with increasing PCL content. This can be attributed to physical crosslinking at the interfaces which plays an important part in shape recovery. Same conclusion was reported by Liu, et al. (2020) for PLA/PCL blends. As the PCL content in blends increases, physical crosslinking at the interfaces responsible for limiting the viscous flow of PCL molecular chains decreases, resulting in irreversible molecular chain slippage and consequently a decrease in PCL's entropy elasticity recovery. SEM results showed that for PLA70/PCL30 blend, the uniformly distributed PCL phase was fully surrounded by PLA phase causing the molecular chains to flow in a restricted area, unlike PLA60/PCL40 blend where the interfaces between the semi-continuous PLA/PCL phase were unstable. For the former, the physical crosslinking at the interfaces could limit the viscous flow of PCL molecular chains, resulting in a little irreversible molecular chain slippage while the case was higher for the later. Investigated PP/PCL blends, i.e. PP90PCL10, PP90PCL10C1.25, PP80PCL20, PP80PCL20C1.25, PP70PCL30 and PP70PCL30C1.25 did not show thermo-responsive shape memory behaviour. When the samples were heated at a temperature lower than the  $T_m$  of PP but a bit higher than that of PCL ( $T_d$ ), the PCL crystals in blends did not melt and their molecular chains did not switch to a temporary shape under applied strain.

### 5.7 3D printed mask

The mask printed contains 4 parts; the mask body, filter connector, filter holder and the cap. The filter connector, holder and cap was printed with PLA100 filament while the mask body responsible for mask fit was printed using shape memory filaments of PLA70PCL30 blends. PLA70PCL30 was selected due to its high  $R_f$  and  $R_c$  values in addition to its mechanical properties.



Figure 46. Printed mask showing the permanent shape (before fitting).

Table 21. Printing parameters for printing mask.

Samples	Nozzle temperature (°C)	Bed temperature (°C)	Raster angle (°)	Infill density (%)	Printing speed (mm/min)
Mask body	205	50	45	15	6000
Other parts	210	50	45	15	6000

### 5.8 Mask fitting

The ability of the 3D printed respirator mask to change shape and be moulded and remoulded to fit different face sizes and shape was investigated. The mask was thermally activated by heating at 65° in an oven for 10 mins. Then it was removed and quickly placed on the face of

the fitter to take the shape. The mask was kept on the fitters face for 3-5mins to fix the shape and after removed. Same mask was thermally activated again and moulded to different fitters. Photographs of the mask before fitting and after fitting on different individuals were taken and shown in Figures 47 while Table 22 shows the dimensions of the mask before and after moulding to different fitters.

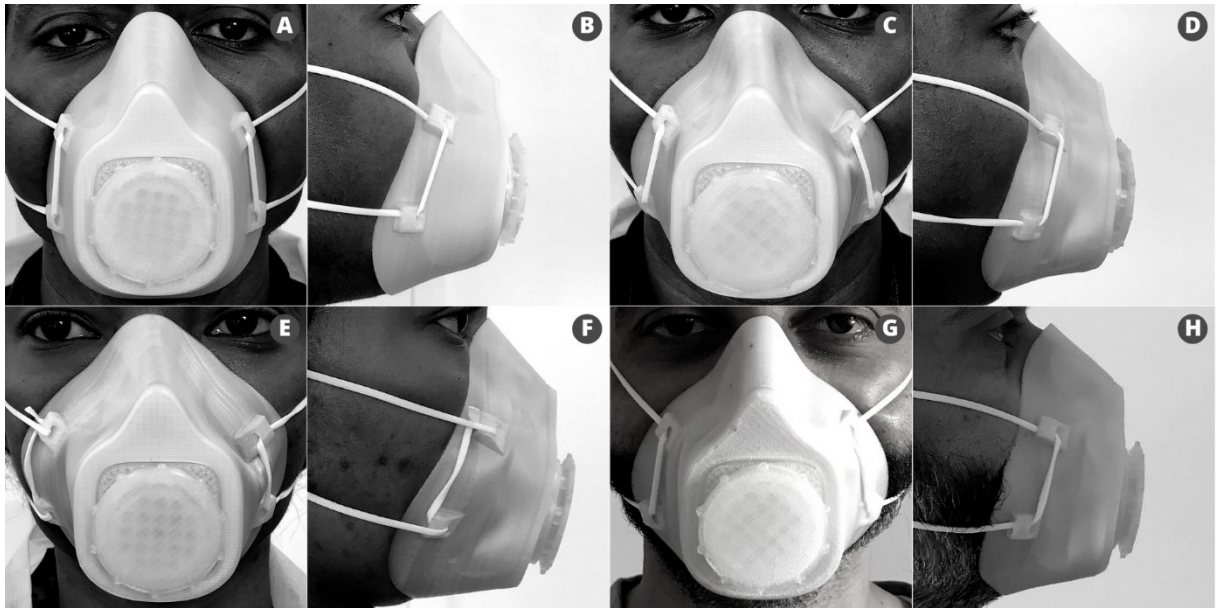


Figure 47. Mask fitting (a) Fitter 1 with original mask - Front view (b) Fitter 1 with original mask - Side view (c) Fitter 1 with moulded mask - Front view (d) Fitter 1 with moulded mask – Side view (e) Fitter 2 with moulded mask - Front view (f) Fitter 2 with moulded mask – Side view (g) Fitter 3 with moulded mask - Front view (h) Fitter 3 with moulded mask – Side view

Table 22. Mask dimension after fitting

Dimensions	3D printed mask	Fitter 1	Fitter 2	Fitter 3
Length (mm)	89.8	80.6	81.2	82.9
Width (mm)	70.7	76.1	76.1	79.6
Depth (mm)	58.5	50.4	53.1	54.2

### 5.9 Self-healing behaviour

The self-healing behaviour of the 3D printed mask was also investigated. The mask was scratched and cut using a blade and placed in an oven set at 65°C for 30 mins. Then the mask

was cooled to room temperature and photographs shown in Figure 48 were taken to provide a visual demonstration of the self-healing process. The scratches on mask completely healed but the cuts did not come in close contact with each other and did not heal. The healing was due to the flow and redistribution of molten PCL into the scratched surface thereby enhancing self-repair.

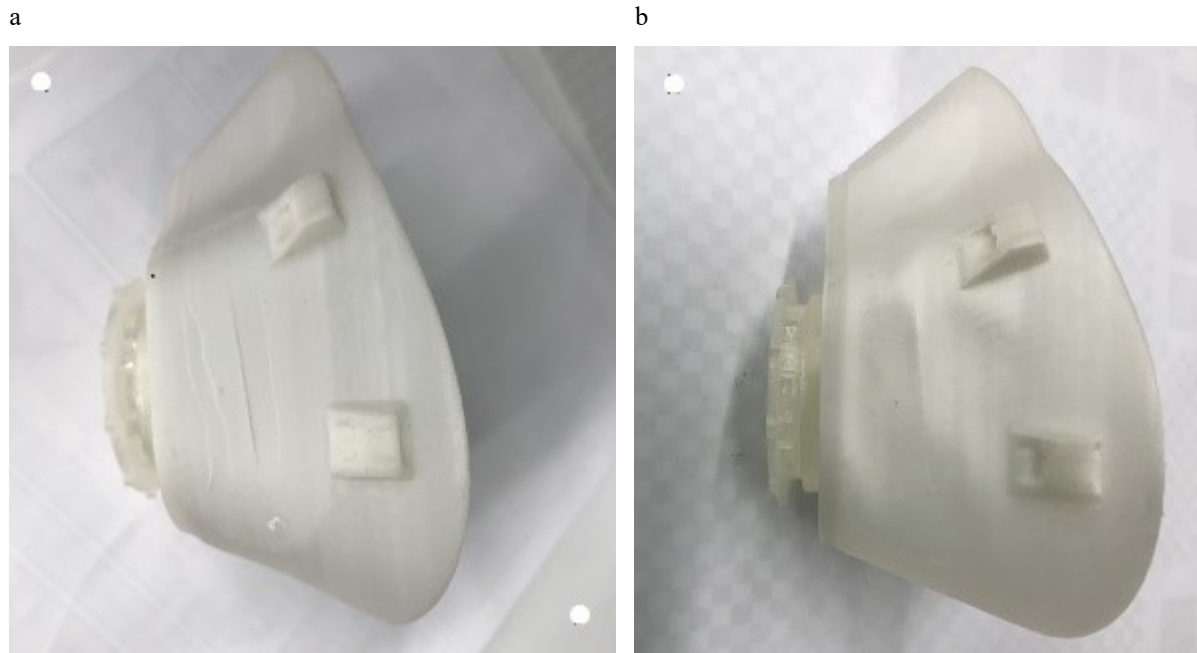


Figure 48. 3D printed mask before and after self-healing process (a) Mask showing Scratch and cut (b) Mask showing healed scratch.

## 6. CONCLUSION

Covid outbreak has increased the demand for facemask and hence the research to produce mask that offer maximum protection. Medical masks are loose fitting and may not offer maximum protection while respirator masks are tight fitting and may offer maximum protection. However, the ability of the wearer to get a proper fit depends on their facial shape and size, hence there is a need to develop respirator masks that can fit any face. It is possible to have a custom-made mask based on an individual's facial shape and size but the possibility for another wearer to use this same mask size and obtain proper fit is limited. As various research on reducing and reusing existing masks to lower the demand for masks and minimize wastes are still ongoing, the idea

of custom-made mask becomes restricted since their shape or size cannot be changed to fit another face during reuse.

In this research, the concept of shape-memory polymers as an alternative polymer for making respirator masks that can change shape and size and can be moulded or remoulded to fit any face was studied. The shape memory polymer in this study was prepared based on polymer blends. Different polymer blends with and without compatibilizers or additives were pre-processed and prepared into filaments by polymer extrusion. The blends successful during polymer extrusion i.e., PLA/PCL, PP/PCL, and LDPE/PCL, were characterised. The blends were characterized based on their new mechanical properties, melting and crystallization behaviour, morphology, and shape memory behaviour.

The mechanical behaviour showed the likelihood to create blends with a wide variety of mechanical properties which solely depends on the blend composition. PLA/PCL blends showed the highest tensile strength and elastic modulus but lowest elongation property while LDPE showed the lowest tensile strength and elastic modulus but good elongation property. PLA is a strong polymer but brittle, hence the high tensile strength but poor elongation property. The compatibilizer improved tensile strength and elastic modulus of LDPE and PP blends but notably decreased the elongation of PP blend. Additive added to PLA/PCL blends had little effect on tensile strength and elastic modulus but significantly increased elongation property.

DSC confirmed the thermal transitions and crystallization behaviour of the blends. All the polymer blends exhibited separated transitions which corresponded to the  $T_m$  of PCL and PP, PLA or LDPE. PCL showed good crystallisation behaviour and enhanced crystallization behaviour in PP and PLA blends. DSC also suggested poor miscibility in polymer blends which enhanced on addition of compatibilizer and additive. Morphology of all the polymer blends exhibited phase separation confirming the immiscibility suggested in DSC. On addition of compatibilizer and additive, improved miscibility was observed confirming the effectiveness of the compatibilizer and additive in improving the interaction between polymer interfaces.

3D printing trials were performed using the filaments of polymer blend extruded. LDPE/PCL blends due to their poor tensile strength resulted in filament bending below the supplying roller of the 3D printer even at very low printing speeds, causing difficulty in printing. PLA/PCL and

PP/PCL blends were successful during this trial. Shape memory tests were conducted for PLA/PCL and PP/PCL blends at different strains. The deformation temperature was set slightly above the temperature of PCL. Investigations on PLA/PCL blend showed that PCL acted as the soft segment and reversible phase while PLA acted as the hard segment and fixity phase. All the PLA/PCL blends investigated showed high  $R_f$  values ( $>98\%$ ) due to the good crystallization ability of PCL phase. Blends without additive showed high  $R_r$  values ( $>97\%$ ) while the blends with additive showed lower  $R_r$  values between 61-96% suggesting the additive reduced the shape recovery of the polymer. PLA70/PCL30 blend had the highest  $R_r$  values of about 99%.  $R_r$  was mostly related to the interfaces and reduced as the PCL content in blends increased from 30 to 40 wt.%. This was due to the decrease in physical crosslinking at the interfaces which causes irreversible molecular chain slippage and consequently a decrease in PCL's entropy elasticity recovery. All the PP/PCL blends did not show shape memory behaviour. The PCL crystals in blends did not melt and their molecular chains did not switch to a temporary shape under heating and applied strain.

Following the results obtained from mechanical properties, melting and crystallization behaviour, morphology, and shape memory behaviour altogether, PLA70/PCL30 blend was selected as the shape memory polymer and printing material for 3D printing the mask. Finally, the 3D printed respirator masks was thermally activated and moulded to different faces to confirm their shape fixing and recovery ability. The mask showed good shape memory behaviour after several moulding and remoulding. In addition, the self-healing behaviour of the mask was investigated. The scratches on mask completely healed but the cuts did not come in close contact with each other and did not heal.

The shape memory facemask developed in this study is for protection against Covid-19 transmission and cuts across current problems regarding facemask such as fit and maximum protection, reusability, and waste minimization.

## **7. FUTURE RESEARCH**

Since the designed mask for protection against Covid is reusable and so can be passed from one wearer to another, long-term usage might lead to contamination because germs and viruses can build and collect on the mask during exposure. It is therefore recommended that further research

on the possibility of introducing antibacterial and antiviral properties to SMP matrix or coating the mask with antibacterial or antiviral properties be carried out.

Physical interaction at the interface between two phases in blend is a major factor that affects shape recovery. Physical interaction can be improved by ensuring uniform distribution of polymers on each polymers' matrixes. Therefore, for future experimentation, research, and production of the designed respiratory mask, it is recommended that polymer materials be grinded or reduced to same size and premixed thoroughly before transferring to the hopper in extruder to achieve uniform distribution. This will solve the problem of improper mixing in extruder and as well ensure uniform distribution.

Standard tests to determine the performance and safety of respirator masks should be carried out. These performance tests should include filtration efficiency, total inward leakage, breathing resistance, CO<sub>2</sub> build-up, clogging and Microbial cleanliness.

Other polymers, most importantly, biodegradable polymers can be investigated for shape memory.

## REFERENCES

- Adanur, S. & Ajay, J., 2020. Filtration mechanisms and manufacturing methods of face masks: An overview. *Journal of Industrial Textiles*, p. 1528083720980169.
- Alex, B., 2020. Different types of face mask to use during the COVID-19 pandemic. [Online] Available at: <https://www.medicalnewstoday.com/articles/types-of-face-mask> [Accessed 29 January, 2021].
- Aumnate, C., Rudolph, N. & Sarmadi, M., 2019. Recycling of polypropylene/polyethylene blends: Effect of chain structure on the crystallization behaviors. *Polymers*, 11(9), p. 1456.
- Bailar, J. C. et al., 2006. Reusability of facemasks during an influenza pandemic. *Institute of Medicine of the National Academies*, pp. 64-65.
- Behl, M. & Lendlein, A., 2007. Actively moving polymers. *Soft Matter*, 3(1), pp. 58-67.
- Bharti, N. & Shailendra, S., 2020. COVID-19: The Use of 3D Printing to Address PPE Shortage during a Pandemic—A Safety Perspective. *ACS Chemical Health & Safety* (27)6, pp. 335-340.
- Bhattacharya, S., Hailstone, R. & Lewis, C., 2020. Thermoplastic Blend Exhibiting Shape Memory-Assisted Self-Healing Functionality. *ACS Applied Materials & Interfaces*, 12(41), pp. 46733-46742.
- Blad, T. et al., 2020. A Rapidly Deployable Test Suite for Respiratory Protective Devices in the COVID-19 Pandemic. *Applied Biosafety* 25(3), pp. 161-168.
- British Standards Institution, 2009. *Respiratory protective devices: filtering half masks to protect against particles - requirements , testing, marking*, London: Bsi Standards Limited.
- British Standards Institution, 2019. *Respiratory protective devices: methods of test Part 7, Determination of particle filter penetration*, London: Bsi Standards Limited.
- CDC, 2020a. Your Guide to Masks. [Online] Available at: <https://www.cdc.gov/coronavirus/2019-ncov/prevent-getting-sick/about-face-coverings.html> [Accessed 27 October 2020].

CDC, 2020b. Personal Protective Equipment: Questions and Answers. [Online] Available at: <https://www.cdc.gov/coronavirus/2019-ncov/hcp/respirator-use-faq.html> [Accessed 27 October 2020].

CDC, 2020c. Personal Protective Equipment: Questions and Answers. [Online] Available at: <https://www.cdc.gov/coronavirus/2019-ncov/hcp/respirator-use-faq.html> [Accessed 9 September 2020].

Chavalitpanya, K. & Phattanarudee, S., 2013. Poly (lactic acid)/polycaprolactone blends compatibilized with block copolymer. *Energy Procedia*, 34, pp. 542-548.

Chellamani, K. P., Veerasubramanian, D. & Balaji, R. V., 2013. Surgical face masks: manufacturing methods and classification. *Journal of Academia and Industrial Research*, 2(6), pp. 320-4.

Chua, M. H. et al., 2020. Face Masks in the New COVID-19 Normal: Materials, Testing, and Perspectives. *Research*, pp. 1-40.

Das, O. et al., 2020. The need for fully bio-based facemasks to counter coronavirus outbreaks: A perspective. *Science of The Total Environment*, p. 139611.

Dutton, K. C., 2009. Overview and analysis of the melt-blown process and parameters. *Journal of Textile and Apparel, Technology and Management*, 6(1).

Ebnesajjad, S. & Ebnesajjad, C., 2014. *Surface treatment of materials for adhesive bonding..* 2nd ed. Amsterdam: William Andrew.

Fadare, O. O. & Okoffo, E. D., 2020. Covid-19 face masks: a potential source of microplastic fibers in the environment. *The Science of the total environment*, 737, p. 140279.

FDA, 2020. Face Masks, Including Surgical Masks, and Respirators for COVID-19. [Online] Available at: <https://www.fda.gov/medical-devices/coronavirus-covid-19-and-medical-devices/face-masks-and-surgical-masks-covid-19-manufacturing-purchasing-importing-and-donating-masks-during> [Accessed 27 December 2020].

Ferri, J. et al., 2016. Effect of miscibility on mechanical and thermal properties of poly (lactic acid)/polycaprolactone blends. *Polymer International*, 65(4), pp. 453-463.

- Guo, Y. et al., 2018. The effect of plasticizer on the shape memory properties of poly (lactide acid)/poly (ethylene glycol) blends. *Journal of Materials Research* 33 (23), pp. 4101-4112.
- Hager, M. D., Stefan, B., Christine, W. & Ulrich, S. S., 2015. Shape memory polymers: Past, present and future developments. *Progress in Polymer Science* 49, pp. 3-33.
- Hemjyoti, K., 2018. *Shape Memory Polymers : Theory and Application*. Berlin: De Gruyter.
- Henneberry, B., 2020a. How to Make N95 Masks. [Online] Available at: <https://www.thomasnet.com/articles/plant-facility-equipment/how-to-make-n95-masks> [Accessed 15 October 2020].
- Henneberry, B., 2020b. How are Surgical Masks Made?. [Online] Available at: <https://www.thomasnet.com/articles/other/how-surgical-masks-are-made/> [Accessed 15 October 2020].
- Hu, J., 2007. *Shape memory polymers and textiles*. Elsevier, p. 62.
- Hu, J., 2014. *Shape memory polymers: Fundamentals, advances and applications*. s.l.:Smithers Rapra.
- Jeong, H. M., Ji, H. S., Sang, Y. L. & Byung, K. K., 2001. Miscibility and shape memory property of poly (vinyl chloride)/thermoplastic polyurethane blends. *Journal of materials science* 36(22), pp. 5457-5463.
- Jianwen, X. & Song, J., 2011. Thermal responsive shape memory polymers for biomedical applications. *Biomed. Eng. Front. Chall*, pp. 125-142.
- Jing, X., Hao-Yang, M., Xiang-Fang, P. & Lih-Sheng, T., 2015. The morphology, properties, and shape memory behavior of polylactic acid/thermoplastic polyurethane blends. *Polymer Engineering & Science* 55(1), pp. 70-80.
- Kahar, A., Ismail, H. & Othman, N., 2012. Effects of polyethylene-grafted maleic anhydride as a compatibilizer on the morphology and tensile properties of (thermoplastic tapioca starch)/(high-density polyethylene)/(natural rubber) blends.. *Journal of Vinyl and Additive Technology*, 18(1), pp. 65-70.
- Krucinaska, I., 2005. *Textiles for respiratory protection*. In: *Textiles for protection*. s.l.:Woodhead Publishing Limited, pp. 465-501.

- Krucínska, I. et al., 2012. Biodegradable particle filtering half masks for respiratory protection. *Fibres & Textiles in Eastern Europe*.
- Lai, S. M. & Lan, Y. C., 2013. Shape memory properties of melt-blended polylactic acid (PLA)/thermoplastic polyurethane (TPU) bio-based blends. *Journal of Polymer Research* 20.5, p. 140.
- Langer, R., Lendlein, A., Schmidt, A. & Grablowitz, H., 2000. Biodegradable shape memory polymers.. U.S., Patent No. 6,160,084.
- Lee, B. S. et al., 2001. Structure and thermomechanical properties of polyurethane block copolymers with shape memory effect. *Macromolecules*, 34(18), pp. 6431-6437.
- Lendlein, A., Hongyan, J., Oliver, J. & Robert, L., 2005. Light-induced shape-memory polymers. *Nature* 434(7035), pp. 879-882.
- Lendlein, A. & Kelch, S., 2002. Shape-memory polymers. *Angewandte Chemie International Edition* 41(12), pp. 2034-2057.
- Leng, J. & Shanyi, D., 2010. *Shape-memory polymers and multifunctional composites..* s.l.:CRC Press.
- Lepelletier, D. et al., 2020. What face mask for what use in the context of the COVID-19 pandemic? The French guidelines. *Journal of Hospital Infection*, 105(3), pp. 414-418.
- Lim, H., 2010. A review of spunbond process. *Journal of Textile and Apparel, Technology and Management*, 6(3).
- Li, S., Lu, L. & Zeng, W., 2009. Thermostimulative shape-memory effect of reactive compatibilized high-density polyethylene/poly (ethylene terephthalate) blends by an ethylene-butyl acrylate-glycidyl methacrylate terpolymer. *Journal of applied polymer science*, 112(6), pp. 3341-3346.
- Liu, C. et al., 2002. Chemically cross-linked polycyclooctene: synthesis, characterization, and shape memory behavior. *Macromolecules*, 35(27), pp. 9868-9874..
- Liu, C. & Mather, P. T., 2003. Thermomechanical characterization of blends of poly (vinyl acetate) with semicrystalline polymers for shape memory applications. *ANTEC-CONFERENCE PROCEEDINGS* (2), pp. 1962-1966.

- Liu, H., He, H. & Bai, H., 2020. Favorable Thermoresponsive Shape Memory Effects of 3D Printed Poly (Lactic Acid)/Poly ( $\epsilon$ -Caprolactone) Blends Fabricated by Fused Deposition Modeling. *Macromolecular Materials and Engineering* 305(11), p. 2000295.
- Liu, X. & Zhang, S., 2020. COVID-19: Face masks and human-to-human transmission. *Influenza and Other Respiratory Viruses*.
- Lu, H. et al., 2014. Significantly improving infrared light-induced shape recovery behavior of shape memory polymeric nanocomposite via a synergistic effect of carbon nanotube and boron nitride. *Composites Part B: Engineering* (62), pp. 256-261.
- Luo, X. et al., 1997. Thermally stimulated shape-memory behavior of ethylene oxide-ethylene terephthalate segmented copolymer. *Journal of Applied Polymer Science* 64(12), pp. 2433-2440.
- Lu, X., Sun, Z., Cai, W. & Gao, Z., 2008. Study on the shape memory effects of poly (l-lactide-co- $\epsilon$ -caprolactone) biodegradable polymers. *Journal of Materials Science: Materials in Medicine* 19(1), pp. 395-399.
- Ma, N., Lu, Y., He, J. & Dai, H., 2019. Application of shape memory materials in protective clothing: a review. *The Journal of The Textile Institute*, 110(6), pp. 950-958.
- Marc, B. & Andreas, L., 2007. Shape-memory polymers. *Materials Today* 10 (4), pp. Pages 20-28.
- Meng, Q. et al., 2009. The shape memory properties of biodegradable chitosan/poly (l-lactide) composites. *Journal of Polymers and the Environment* 17(3), p. 212.
- Midha, V. & Dakuri, A., 2017. Spun bonding technology and fabric properties: a review. *Journal of Textile Engineering & Fashion Technology* 1(4), p. 126–133.
- Navarro-Baena, I. et al., 2016. Design of biodegradable blends based on PLA and PCL: From morphological, thermal and mechanical studies to shape memory behavior. *Polymer degradation and stability* (132), pp. 97-108.
- NBN, 2019. Medical face masks - Requirements and test methods, s.l.: Belgian Standard.
- O'Dowd, K. et al., 2020. Face Masks and Respirators in the Fight Against the COVID-19 Pandemic: A Review of Current Materials, Advances and Future Perspectives. *Materials*, 13(15), p. 3363.

- Ohki, T., Ni, Q. Q., Ohsako, N. & Iwamoto, M., 2004. Mechanical and shape memory behavior of composites with shape memory polymer. *Composites Part A: applied science and manufacturing*, 35(9), pp. 1065-1073.
- Özer, A. & Haamustafaoglu, M., 2020. What Should be the Mask Types, Features and Standards Recommended for Health Institutions and for the General Population During the COVID-19 Pandemic?. *Cocuk Enfeksiyon Dergisi*, 14(3), pp. E150-E154..
- Parameswaranpillai, J., Siengchin, S., George, J. & Jose, S., 2020. *Shape Memory Polymers, Blends and Composites*. Singapore: Springer.
- Patel, S., 2015. Disposable Mask Made From Bioplastic Resins. U.S, Patent No. 14/553,479.
- Pu, Y. et al., 2018. Preparation of polypropylene micro and nanofibers by electrostatic-assisted melt blown and their application. *Polymers*, 10(9), p. 959.
- Qin, S. et al., 2018. Fully biodegradable poly (lactic acid)/poly (propylene carbonate) shape memory materials with low recovery temperature based on in situ compatibilization by dicumyl peroxide. *Chinese Journal of Polymer Science*, 36(6), pp. 783-790.
- Ratna, D. & Karger-Kocsis, J., 2008. Recent advances in shape memory polymers and composites: a review.. *Journal of Materials Science*, 43(1), pp. 254-269.
- Raul, F. et al., 2020. *Protective Masks*. s.l.:Fibrenamics.
- Rengasamy, S. et al., 2018. A comparison of total inward leakage measured using sodium chloride (NaCl) and corn oil aerosol methods for air-purifying respirators.. *Journal of occupational and environmental hygiene*, 15(8), pp. 616-627.
- Roudbarian, N., Baniasadi, M., Ansari, M. & Baghani, M., 2019. An experimental investigation on structural design of shape memory polymers. *Smart Materials and Structures*, 28(9), p. 095017.
- Rubio-Romero, J. C., del Carmen Pardo-Ferreira, M., Torrecilla-García, J. A. & Calero-Castro, S., 2020. Disposable masks: Disinfection and sterilization for reuse, and non-certified manufacturing, in the face of shortages during the COVID-19 pandemic. *Safety science* 129, p. 104830.

Schmidt, A. M., 2006. Electromagnetic activation of shape memory polymer networks containing magnetic nanoparticles. *Macromolecular Rapid Communications*, 27(14), pp. 1168-1172.

Serfozo, N. et al., 2017. Size-resolved penetration of filtering materials from CE-marked filtering facepiece respirators. *Aerosol and Air Quality Research*, 17(5), pp. 1305-1315..

Shen, T., Mangeng, L., Dewen, Z. & Liyan, L., 2012. Influence of blocked polyisocyanate on thermomechanical, shape memory and biodegradable properties of poly (lactic acid)/poly (ethylene glycol) blends. *Iranian Polymer Journal*, 21(5), pp. 317-323.

Sozkes, S. & Serda, S., 2020. COVID-19 and respiratory protection for healthcare providers. *International journal of occupational medicine and environmental health*..

Sun, C., Thelen, C., Sanz, I. S. & Wittmann, A., 2020. Evaluation of a new workplace protection factor–measuring method for filtering facepiece respirator. *Safety and health at work*, 11(1), pp. 61-70.

Swennen, G., Pottel, L. & Haers, P., 2020. Custom-made 3D-printed face masks in case of pandemic crisis situations with a lack of commercially available FFP2/3 masks. *International Journal of Oral and Maxillofacial Surgery*, 49(5), pp. 673-677.

Vlachopoulos, J. & Strutt, D., 2003. Polymer processing. *Materials Science and Technology*, 19(9), p. 1161–1169.

Wachirahuttapong, S., Thongpin, C. & Sombatsompop, N., 2016. Effect of PCL and compatibility contents on the morphology, crystallization and mechanical properties of PLA/PCL blends.. *Energy Procedia*, Volume 89, pp. 198-206.

WHO, 2020a. Transmission of SARS-CoV-2: implications for infection prevention precautions. [Online]

Available at: <https://www.who.int/news-room/commentaries/detail/transmission-of-sars-cov-2-implications-for-infection-prevention-precautions>.

[Accessed 27 December 2020].

WHO, 2020b. Rational use of personal protective equipment for coronavirus disease (COVID-19) and considerations during severe shortages. [Online]

Available at: <https://www.who.int/publications/i/item/rational-use-of-personal-protective->

[equipment-for-coronavirus-disease-\(covid-19\)-and-considerations-during-severe-shortages](#)

[Accessed 2 February 2021].

Wibisono, Y., Fadila, C. R., Saiful, S. & Bilad, M. R., 2020. Facile Approaches of Polymeric Face Masks Reuse and Reinforcements for Micro-Aerosol Droplets and Viruses Filtration: A Review. *Polymers*, 12(11), p. 2516.

Xie, T., 2011. Recent advances in polymer shape memory. *Polymer* 52 (22), pp. 4985-5000.

Xu, J. & Jie, S., 2011. Thermal responsive shape memory polymers for biomedical applications. *Biomed. Eng. Front. Chall*, pp. 125-142.

Yu-Chen, S. et al., 2019. 4D-printed hybrids with localized shape memory behaviour: Implementation in a functionally graded structure. *Scientific reports* 9(1), pp. 1-13.

Zhang, H., Haitao, W., Wei, Z. & Qiangguo, D., 2009. A novel type of shape memory polymer blend and the shape memory mechanism. *Polymer* 50(6), pp. 1596-1601.

Zhou, S. et al., 2007. Hydrogen bonding interaction of poly (D, L-lactide)/hydroxyapatite nanocomposites. *Chemistry of materials* 19(2), pp. 247-253.